Quantifying the Carbon Conversion Efficiency and Emission Indices of a Lab-Scale Steam-Assisted Flare

by

Abbas Ahsan

A thesis submitted in partial fulfillment of the requirements for the degree of

Master of Science

Department of Mechanical Engineering
University of Alberta

Abstract

A lab-scale flaring facility was established to study the carbon conversion efficiency (CCE) and emission indices (EIs) of total unburned hydrocarbons (THC), carbon dioxide (CO_2), carbon monoxide (CO), nitrogen oxides (NO_x), and black carbon (BC) for a 25.4 mm diameter steam-assisted flare. Diagnostic equipment including a photoacoustic extinctiometer, NO_x analyzer, and gas chromatograph were used to measure the concentration of the plume species generated by 20 or 40 standard liters per minute (SLPM) methane or propane flames with inner or outer coflows of steam. A carbon mass balance was applied to the flare to account for the carbon-based species produced by combustion and allow for estimates to be made of combustion efficiency and species emission rates of THC, CO_2, CO, NO_x, and BC. Seven unique experimental sets were performed in which the reference case was defined as a 20 SLPM methane jet diffusion flame with an inner coflow of steam through a 12.7 mm diameter tube. The remaining six sets branched off from the reference case with each set featuring a single experimental design difference. Each experimental set was based on a fixed fuel flow rate in which increasing amounts of assist fluid were injected into the flame until a CCE of < 10% was achieved. The steam-to-fuel gas mass flow rate ratios which provoked the onset of the collapse in CCE at 96.5% had a range of 1.0 – 4.1 for the various experimental sets. EIs for NO_x and BC were found to be at a maximum when the flame was unassisted, but decreased by approximately two orders of magnitude with increasing steam assist. EIs for CO_2 remained at a maximum value until the onset in the CCE collapse at which point they began to drop by an order of magnitude. The reverse trend occurred for THC emissions as a result of fuel stripping. During the CCE collapse phase, some of the experimental sets

generated CO emissions as a result of poor fuel-air mixing. The hydrodynamic conditions at the burner exit plane were investigated to provide insight into the discrepancy in behaviour between the different experimental sets.

Preface

The research performed for this thesis was completed in a lab-scale flare facility whose design was done as a collaborative effort with Hamza Ahsan. This includes the design and construction of the burner apparatus and procurement of diagnostic equipment. Parts of Chapter 2 of this thesis have been published in the following paper:

A. Ahsan, H. Ahsan, J.S. Olfert, L.W. Kostiuk, Quantifying the carbon conversion efficiency and emission indices of a lab-scale natural gas flare with internal coflows of air or steam, Experimental Thermal and Fluid Science. 103 (2019) 133–142. doi:10.1016/j.expthermflusci.2019.01.013.

For this paper, I shared equal responsibility with Hamza Ahsan in regards to the experimentation, data collection and processing, analysis, and writing of the manuscript. Dr. Larry Kostiuk and Dr. Jason Olfert provided manuscript edits.

Acknowledgments

The research I have accomplished and the work involved in completing this thesis has been a highly rewarding experience filled with learning and growth. I would like to express my gratitude to Dr. Larry Kostiuk who presented this research opportunity to me and whose passion for flaring inspired me to investigate the topic for myself. I deeply appreciate the countless discussions we've had where you offered mentorship, research guidance and advice, proposals that were sometimes far too difficult to implement, and a wealth of knowledge in the engineering sciences. I would also like to thank Dr. Jason Olfert who initially introduced me to the world of flaring as an undergraduate co-op student and continued to motivate me as a graduate student. Dr. Olfert's keen insight and practical know-how were indispensable in the design and performance of our experiments. The lab space and diagnostic equipment were pretty helpful too.

I would like to extend my thanks to all the members of the FlareNet research group who I have collaborated with in the course of my graduate studies. They have been a source of help and encouragement throughout my research work. I enjoyed their company and the many conversations we've had on flaring and otherwise.

I would also like to offer my sincere thanks to my family who continued to support and motivate me throughout all my studies. Their encouragement helped me dedicate myself to pursuing and completing graduate studies. Lastly, I would like to thank by brother Hamza for being by my side, literally, throughout the course of my research. I think we've had a pretty good run.

Table of Contents

1. Introduction 1

1.1 Flaring 1

1.1.1 Flaring Emissions and their Environmental Impacts 2

1.2 Assisted Flaring 5

1.3 Industry- and Government-Led Studies on Steam-Assisted Flaring 10

1.4 Objectives 23

2. Experimental Setup 25

2.1 Lab-Scale Flare Design 25

2.2 Lab-Scale Flare Test Facility 27

2.3 Methodology for Calculating Carbon Conversion Efficiency and Emission Indices 35

3. Results and Discussion 40

3.1 Experimental Test Matrix 40

3.2 Steady State Burner Temperatures and Exit Plane Conditions 41

3.3 Experimental Set 1: Reference Set with 20 SLPM CH_4 Flame and Inner Steam Coflow through 12.7 mm OD Inner Tube 47

3.4 Experimental Set 2: Doubling the Fuel Flow Rate 52

3.5 Experimental Set 3: Reducing Burner Inner Tube Diameter by Half 54

3.6 Experimental Set 4: Steam-Equivalent Gas Mixture with 58% N_2 and 42% He 56

3.7 Experimental Set 5: Steam-Equivalent Gas Mixture with 50% Steam, 29% N_2, and 21% He 58

3.8 Experimental Set 6: Burning 20 SLPM of C_3H_8 60

3.9 Experimental Set 7: 40 SLPM CH_4 Flame with Steam Outer Coflow 63

3.10 Analysis of Hydrodynamic Conditions at Burner Exit Plane 66

3.11 Comparing Experimental Results to Industry- and Government-Led Studies... 69
4. Conclusions and Recommendations for Future Work 74
4.1 Conclusions 74
4.2 Recommendations for Future Work 78
Bibliography 80
Appendix A Uncertainty Analysis Methodology 85
Appendix B Gas Mass Flow Controller Calibration 87
Appendix C Steam Production and Distribution System Calibration 89
Appendix D Gas Chromatograph Calibration Standards and Uncertainties 92
Appendix E Uncertainty Analysis for CCE and EI 94
Appendix F Adiabatic Flame Temperature 98

List of Tables

Table 1.1: Reynolds and Richardson number operating regimes for pilot-scale and commercial flare stacks based on Pohl and Soelberg [45]. 19
Table 1.2: Maximum pollutant emission indices for steam-assisted flares based on a combustion efficiency of ≥ 96.5% from studies by McDaniel [40], Pohl and Soelberg [45], and Allen and Torres [47]. 23
Table 3.1: Lab-scale steam-assisted flaring experimental test matrix. 41
Table 3.2: Range of temperature measurements taken at various *z* values in the annular and center space of the burner. 41
Table 3.3: Steam-to-fuel gas MFRs with corresponding exit velocities, momentums, and Reynolds number for fuel and steam. Calculated range in parameters for steam assist correspond to the range in the minimum to maximum steam flow rates, excluding the unassisted case. 45
Table 3.4: 100-year GWP values for various pollutant species and their respective uncertainties obtained from the IPCC [6,54]. 47
Table 3.5: Steam-fuel gas MFR at CCE of 96.5% and maximum EIs for CCE ≥ 96.5%. 69
Table D.1: GC calibration standards. 92
Table D.2: Uncertainties for gases measured by GC. 93
Table E.1: Repeatability in BC, NO_x, and CO_2 emission indices for unassisted flame tests for experimental sets 1, 4, and 5. 97

List of Figures

Figure 1.1: Average CO_2 concentrations measured at Mauna Loa Observatory, Hawaii from 1958 − 2018 [7,8]. 3
Figure 1.2: Typical design of a steam-assisted flare head with the (a) top view and (b) front view showing the configuration of lower, center, and upper steam nozzles. 7
Figure 1.3: Combustion efficiency of a steam-assisted flare burning (a) crude propylene with an LHV of 81.3 MJ/m^3 and (b) nitrogen-diluted crude propylene with an average LHV of 12.0 MJ/m^3 from a study by McDaniel [40]. 12
Figure 1.4: Emission indices of a steam-assisted flare burning flare gas with an LHV of 81.3 MJ/m^3 and 12.0 MJ/m^3 from a study by McDaniel [40]. 14
Figure 1.5: Combustion efficiency of a steam-assisted flare burning a propane and nitrogen mixture with an LHV of 49.3 MJ/m^3 from a study by Pohl *et al*. [43]. 16
Figure 1.6: Combustion efficiency of a Coanda steam-assisted flare burning a propane and nitrogen mixture with an LHV of 13.6 MJ/m^3 from a study by Pohl and Soelberg [45]. 18
Figure 1.7: Combustion efficiency of an industrial flare with center and upper steam-assist burning high and low flare gas flow rates and LHVs from a study by Allen and Torres [47]. 21
Figure 1.8: THC emission indices and corresponding combustion efficiencies for steam-assisted flare tests performed by Allen and Torres [47]. 22
Figure 1.9: NO_x emission indices and corresponding combustion efficiencies for steam-assisted flare tests performed by Allen and Torres [47]. 22
Figure 2.1: Front view of the burner along with a section view showing the inner and outer flow inlets and pathways. A close-up of the tip of the burner is presented to show the locations of the thermocouples placed inside the inner tube and in the annular space between the inner and outer tubes. A coordinate axis is shown above the tip of the burner, with *z* pointing in the upward axial direction and *r* pointing in the radial direction. 26
Figure 2.2: Flare test facility for conducting experiments with the lab-scale steam-assisted flare. 28

Figure 2.3: Establishing a closed carbon mass balance around the combustion reaction with the mole fractions of carbon-based gas species and the soot mass concentration characterized by X_k and f_m, respectively. 36
Figure 3.1: Temperature measurements of fuel and steam taken at thermocouple positions located up to 40 mm below the exit plane in the annular space and in the center of the inner tube exit plane for experimental sets (a) 1 and (b) 7. Steam saturation temperatures at local pressure are shown in red dashed lines. 43
Figure 3.2: Adiabatic flame temperatures for experimental sets 1 – 7. 46
Figure 3.3: Experimental set 1 CCE plot (bottom) and EI plot (top). 50
Figure 3.4: Near-field flow structure of inner and annular jets issuing from a nozzle with exit velocities of v_i and v_o, respectively. The heights of the inner and outer potential cores are labeled as $h_{pc,i}$ and $h_{pc,o}$, respectively. 51
Figure 3.5: Photos of experimental set 1 flame taken at increasing steam-to-fuel gas MFRs. 51
Figure 3.6: Experimental set 2 CCE plot (bottom) and EI plot (top). 53
Figure 3.7: Experimental set 3 CCE plot (bottom) and EI plot (top). 56
Figure 3.8: Experimental set 4 CCE plot (bottom) and EI plot (top). 58
Figure 3.9: Experimental set 5 CCE plot (bottom) and EI plot (top). 60
Figure 3.10: Experimental set 6 CCE plot (bottom) and EI plot (top). 62
Figure 3.11: Photos of experimental set 6 flame taken at increasing steam-to-fuel gas MFRs..... 63
Figure 3.12: Experimental set 7 CCE plot (bottom) and EI plot (top). 65
Figure 3.13: Photos of experimental set 7 flame taken at increasing steam-to-fuel gas MFRs..... 66
Figure 3.14: The response of CCE to increasing mass flow rates of assist fluid for experimental sets 1 – 7..... 66
Figure 3.15: Response of CCE to increasing steam-to-fuel gas velocity ratio for experimental sets 1 – 6..... 67
Figure 3.16: Response of CCE to increasing steam-to-fuel gas momentum ratio for experimental sets 1 – 6..... 68

Figure 3.17: Recommended steam-to-fuel gas MFR operating ranges for experimental sets 1 – 7 70
Figure B.1: Mass flow controller calibration setup. 87
Figure B.2: Calibration curve for 50 SLPM mass flow controller running methane. 88
Figure C.1: Steam production and delivery system calibration setup. 89
Figure C.2: Theoretical mass flow rate of steam. 90
Figure C.3: Experimental mass flow rate of steam. 90
Figure C.4: Steam mass flow rate calibration curve. 91
Figure D.1: Calibration curve for CH_4. 92
Figure F.1: Steady-flow combustion process for determining the adiabatic flame temperature. 98

Chapter 1

1. Introduction

1.1 Flaring

In the development of hydrocarbon resources, flaring is a common practice by which unwanted flammable gases are burned off in a controlled fashion. Flaring can occur in a wide variety of settings: from inland oil fields and refineries to offshore drilling platforms. The combustion of the flare gas can take place a few meters above the ground in the case of ground flares, or up to 150 m above the ground at the tip of an elevated vertical stack [1]. This combustion process occurs predominantly in the upstream oil and gas industry, but also downstream. Generally, flaring can be divided into three categories: production, process, and emergency flaring [2]. Production flaring is concerned with the disposal of the natural gas that is associated with the extraction of crude oil in the upstream oil and gas industry. Process and emergency flaring takes place in the downstream oil and gas industry. In oil refineries and petrochemical plants, process flares operate continuously to dispose of hydrocarbon gases that leak from relief valves. Emergency flares eliminate large volumes of gases in the event of a plant shutdown or major equipment failure. According to data released by the Global Gas Flaring Reduction (GGFR) partnership, the total volume of natural gas flared upstream in 2017 was 141 billion cubic meters [3]. A study by Elvidge *et al*. [4] revealed that upstream flaring was responsible for 90.6% of total global flaring, with the remainder taking place downstream and on industrial sites. In any case, flaring is considered the safest method of disposing of undesired

hydrocarbon gases due to the severe environmental implications of simply venting the gases into the atmosphere.

1.1.1 Flaring Emissions and their Environmental Impacts

According to the Intergovernmental Panel on Climate Change (IPCC), Earth's mean surface temperature—an average of air temperatures measured approximately 1.5 m above the land surface and ocean water temperatures measured 1 to 15 m below the ocean surface [5]—has increased since 1880 with the last few decades being the warmest since then [6]. From 1880 to 2012, Earth's land and ocean surface experienced an average combined warming of 0.85 °C with a 90% confidence interval of (0.65, 1.06) °C [6]. This persistent transition in the Earth's climate over a span of time as a result of natural factors or human activity is termed climate change. The IPCC has made near- and long-term projections of the effects of climate change which include the increased likelihood of changes to patterns in the water cycle and atmospheric circulation, higher ocean temperatures, and shrinkage of Arctic sea ice [6]. In their Fifth Assessment Report, the IPCC indicated that it is extremely likely (*i.e.*, 95 – 100% probability) that the rising global temperatures, referred to as global warming, was mostly caused by anthropogenic forcings, such as greenhouse gas emissions, since 1951 [6]. The effect by which anthropogenic agents lead to a shift in global temperatures is called radiative forcing and is defined by the IPCC as the change in the overall radiative flux towards the Earth's surface based on the energy balance between inbound solar radiation and outbound infrared radiation [6]. Radiative forcing is expressed in Watts per square meter (W/m^2) at the tropopause, which is the boundary between Earth's first and second atmospheric layers: the troposphere and stratosphere [6]. The greater the concentration of greenhouse gases in the atmosphere, which absorb Earth's outgoing infrared radiation thereby leading to higher global temperatures, the more positive the radiative forcing. Using the start of the industrial era as a baseline (*i.e.*, 1750 onwards), the increase in the atmospheric concentration of the greenhouse gas carbon dioxide (CO_2) has had the largest impact in driving radiative forcing to becoming more positive [6]. Over the past 60 years, the average CO_2 concentration in the atmosphere has increased by 30% from 315 ppm

(parts per million) to 409 ppm [7,8], as shown in Figure 1.1. As a result, the global radiative forcing for CO_2 in the industrial era has recently been estimated to be 2.01 W/m^2 [9]. The rise in the atmospheric CO_2 concentration is believed to be anthropogenic in nature and primarily caused by the combustion of fossil fuels such as coal, natural gas, and petroleum [10]. A significant contributor to increased global CO_2 emissions is flaring, which Elvidge *et al*. estimated to have been 285 347 kt in 2015 [4].

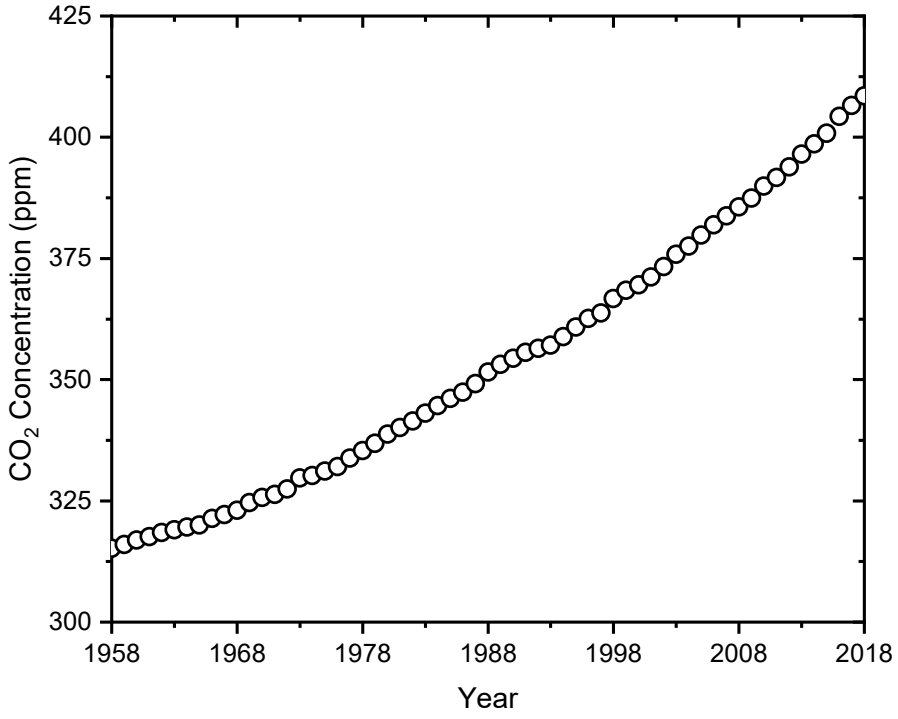

Figure 1.1: Average CO_2 concentrations measured at Mauna Loa Observatory, Hawaii from 1958 − 2018 [7,8]**.**

Despite the severity of the problem that exists with elevated CO_2 levels, flaring is still a necessary measure for preventing methane (CH_4)—a major component of natural gas—from accumulating in the atmosphere through venting. This is due to CH_4's global radiative forcing of 0.51 W/m^2 [9], which is the highest of all greenhouse gases after CO_2. On a mass basis, the IPCC confirmed that CH_4 is a much more potent greenhouse gas than CO_2, with a global warming potential (GWP) based on a 100-year time horizon of 28 [6]. This means that over this time period, one tonne of

methane traps 28 times more heat than one tonne of CO_2. Although flaring provides a chemical pathway for the oxidation of hydrocarbon gases into CO_2 and water vapour, it is not a perfectly efficient process. The performance of a flare can be assessed by its combustion efficiency (also referred to as carbon conversion efficiency), which is based on the degree to which carbon in fuel components of the flare gas is converted to CO_2. Factors such as the flare gas composition and ambient conditions can reduce the combustion efficiency, leading to the release of unburned hydrocarbon gases from the flare [11].

Another significant pollutant emitted by flaring is soot, which is categorized as particulate matter with a diameter equal to or less than 2.5 μm ($PM_{2.5}$) [12]. Among the typical products of hydrocarbon combustion, this class of particles is the most hazardous to human health due to its small size which can penetrate into the lungs and cause respiratory illnesses [13]. Soot is an aggregation of nanoscale spherules forming a fractal-like geometry, in which Black Carbon (BC) is the carbonaceous component [14]. BC has recently been implicated as having serious effects on human health and environmental welfare. In fact, BC has been specifically linked to the negative health effects associated with $PM_{2.5}$ [15,16]. In terms of climate forcing, BC is the second most potent emission after CO_2 and ahead of CH_4, with an industrial era radiative forcing value of 1.1 W/m^2 and 90% uncertainty limits of (0.17, 2.1) W/m^2 [17]. BC therefore has a climate warming effect, which is accomplished by its direct absorption of sunlight in the atmosphere and reduction of ice and snow surface albedo when deposited on those surfaces [18]. According to Stohl *et al*. [19], gas flaring is the prevailing source of BC emissions in the Arctic and is responsible for 42% of the annual mean accumulation of BC on arctic surfaces. Unlike greenhouse gases, however, BC has a shorter atmospheric lifetime measured in days and weeks [18]. Therefore, reducing BC emissions has the potential to bring rapid improvements to air quality and reduce climate forcing.

Furthermore, flaring may yield other harmful pollutants such as volatile organic compounds (VOCs), carbon monoxide (CO), sulphur dioxide (SO_2), polycyclic aromatic hydrocarbons (PAHs), and nitrogen oxides (NO_x = NO + NO_2) [20]. According to Allen [21], VOCs and NO_x emissions in the United States from

2002 to 2011 have increased by 400% and 94% respectively from the oil and gas supply chain, of which flaring is a key component. In sunlight, photochemistry involving VOCs and NO_x leads to the formation of ground-level ozone (O_3), which is a critical ingredient of smog [22]. A test performed by Torres *et al*. [23] on a full-scale industrial flare showed that incomplete combustion produced CO emissions as high as 80% of the total emissions on a carbon basis. On top of being poisonous for human health and one of the leading causes of accidental poisoning in the United States [24], carbon monoxide has an indirect climate forcing effect due to its link to methane concentrations in the atmosphere [25]. Although anthropogenic emissions of SO_2 have declined significantly over the past two decades in North America, they are still increasing or remaining constant in developing nations [26]. A major source of SO_2 emissions is sour gas well test flaring and hydrogen sulfide (H_2S) flaring in oil refineries, especially in the Middle East where measures to strip H_2S from the flare gas stream to convert to sulphur are not always present [26]. The United States Environmental Protection Agency (EPA) states that flaring H_2S can cause high concentrations of SO_2 in the ambient air and can cause respiratory illnesses to those who are exposed to it [27]. SO_2 emissions are also known to be a precursor to acid rain and fine particulate matter [28]. According to Slaski *et al*. [29], ground level concentrations of certain PAHs near sweet and sour gas flares were similar to the levels found in large industrialized cities. Although PAHs are not major contributors to O_3 depletion in the stratosphere, climate forcing, or ground-level O_3 formation, some PAHs have been classified as toxic and probably carcinogenic to humans [30].

1.2 Assisted Flaring

With the rise in popularity of flaring as a means of disposing of natural gas associated with oil extraction in the early 20th century United States, anti-smoke legislation also became prevalent due to the nuisance that smoke produced by the flare caused the local populace. Furthermore, some refineries endured damage to their flare stacks as a result of windy conditions causing the flame to bend in the direction of the wind and get drawn into the low pressure zone on the downwind side of the stack. Over time, the flare stack structure would deteriorate and fall apart due to prolonged contact with

the flame. In an attempt to resolve these issues, several petrochemical companies in the late 1940s and early 1950s in the United States introduced the concept of a smokeless flare [31–33]. This invention—later known as an assisted flare—called for the injection of an additional substance, such as air or steam, into the flare stack to improve combustion efficiency and increase the flare gas flow velocity. The practice of improving the flare performance by introducing an assist medium became an industry standard and is recommended by the American Petroleum Institute (API) for smokeless operation [34]. The most common form of assisted flaring today according to the API is steam-assisted flaring, in which steam delivered at a gauge pressure of up to 1 034 kPa is injected in a variety of ways through a series of nozzles in the flare stack. As depicted in Figure 1.2, there are generally three nozzle configurations that are employed in industry: upper, center, and lower steam. Typically, steam-assisted flares will have center steam delivered from a single nozzle located coaxially within the flare but with its tip below the flare exit plane. Steam discharged from this nozzle is expected to augment the momentum of the flare gas thereby increasing the flare gas exit velocity and improving combustion efficiency. Another common placement for steam nozzles, which deliver upper steam, is on a ring-shaped manifold around the circumference of the flare tip with the nozzles pointing towards the combustion zone to create turbulence by which more air is entrained in the combustion reaction. Flare stack manufacturers usually stipulate a minimum required steam flow rate through these two categories of nozzles. The third, less common, nozzle configuration provides the same benefit as the ring manifold nozzles and is comprised of an array of tubes interspersed within the stack structure with their tips flush with the flare stack exit plane. Although these nozzles deliver steam at the flare tip, this steam is termed lower steam. The API states that the added benefit of steam over air is that steam further promotes complete combustion through the water-gas shift reaction where the addition of water reacts with CO to form CO_2 and hydrogen (H_2).

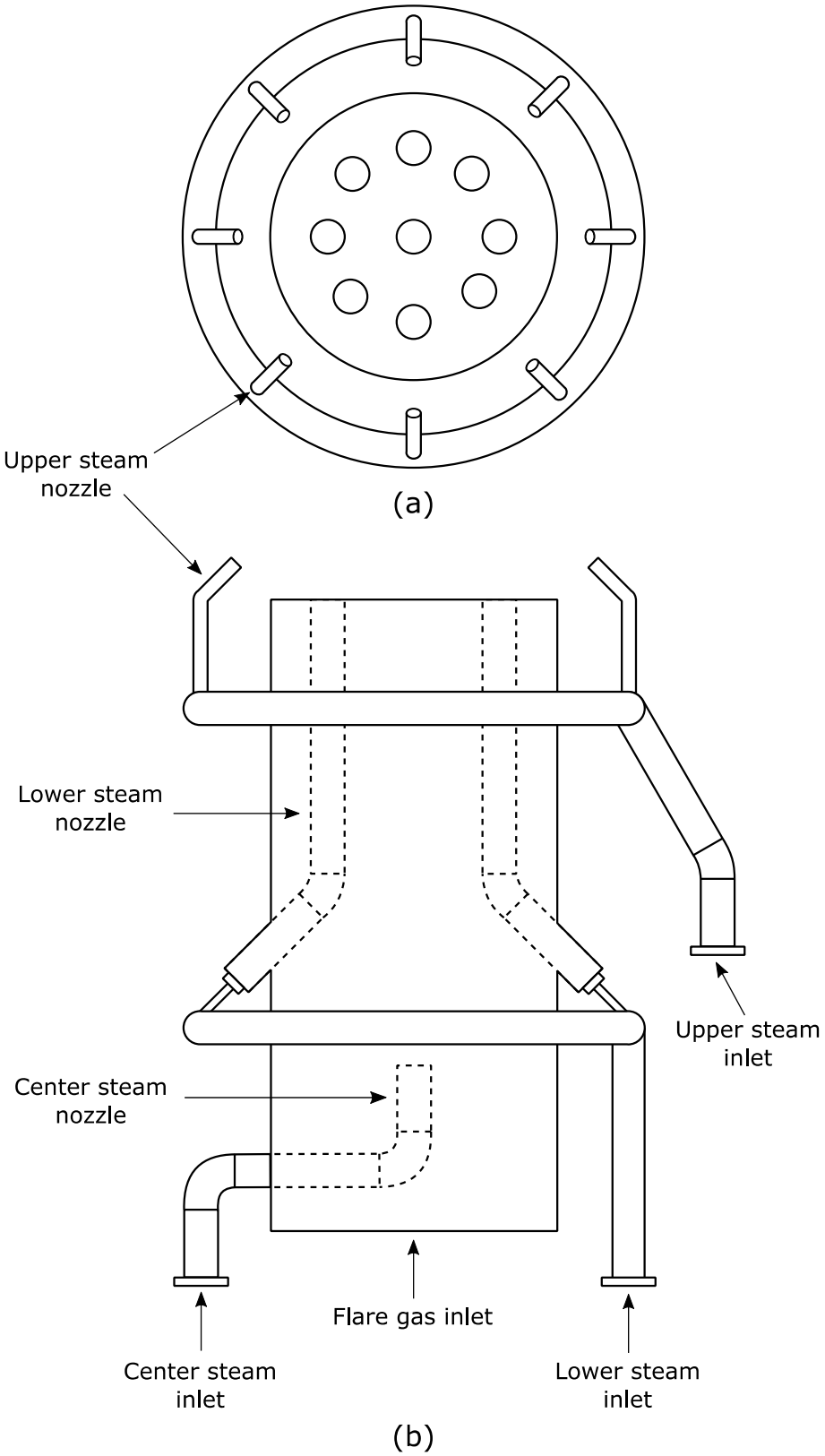

Figure 1.2: Typical design of a steam-assisted flare head with the (a) top view and (b) front view showing the configuration of lower, center, and upper steam nozzles.

Although steam-assisted flaring is the prevailing mode of smokeless flaring in the United States, it is less common in subarctic or desert climates, where there is a risk of steam lines freezing up or where access to water is limited. The next most common form of assisted flaring is air-assisted flaring using high pressure compressed air (*i.e.*, ≥ 689 kPa gauge pressure). The methods by which air is injected into the flare stack is similar to that of steam-assisted flares except that air is usually not injected below the flare tip in order to avoid premixing of the air and flare gas. This is to prevent the upstream propagation of the flame into the flare stack which has the potential to damage the stack structure. Since compressed air is considered the most expensive utility in industrial operations [35], low pressure air (*i.e.*, up to 5 kPa gauge pressure) is sometimes opted for instead. An air blower is used to generate the low pressure air for injection at the flare tip. Another type of assisted flaring is gas-assisted flaring, in which a hydrocarbon gas such as natural gas with a supply gauge pressure of up to 1 034 kPa is injected into the flare stack using similar nozzles as for steam-assisted flaring. This assist method is usually implemented for the disposal of heavier hydrocarbon flare gases, in which the injection of a secondary combustible gas is intended to improve combustion efficiency by decreasing the flare gas energy density while increasing flare gas momentum and turbulence in the combustion zone. The least common form of assisted flaring is with the use of high pressure water (*i.e.*, up to gauge pressure of 689 kPa) that is sprayed into the combustion zone of the flare. The water is sourced from wastewater or brine reserves which are by-products of the industrial processes, or seawater in the case of offshore flares.

While air-assisted flaring is prevalent in both the upstream and downstream oil and gas industry, steam-assisted flaring is only found downstream due to the requirement for a steam-generating facility. Regardless of the choice for assisted flaring, flare operators are required to meet federal and local regulations pertaining to flare emissions. A major piece of federal regulation that flare operators must adhere to in the United States is Title 40 of the Code of Federal Regulations Section 60.18 (*i.e.*, 40 CFR § 60.18) [36] on the performance of standards for stationary sources of air pollution, which stipulates a number of requirements for the operation of flares. Besides the basic requirement that flares must be operated such that a flame is always

present, the only injunction in the statute that places a restriction on flare emissions states that flares are only permitted to release visible emissions for up to 5 minutes in any 2 consecutive hours of operation. Most of the remaining statute pertaining to flaring aims at specifying the minimum required flare gas lower heating value (LHV) and the range of allowable flare gas exit velocities. For air- and steam-assisted flares, the minimum required LHV is 11.2 MJ/m^3. The maximum permitted exit velocity in meters per second for steam-assisted and unassisted flares is defined as follows:

$$V_{\max} = 10^{\frac{\mathrm{LHV_{FG}}+28.8}{31.7}} \tag{1.1}$$

where LHV_{FG} is the LHV of the flare gas in MJ/m^3. However, the above equation is only to be used for an LHV of up to 37.3 MJ/m^3 which yields a maximum exit velocity of 122 m/s. Flares with LHV's greater than 37.3 MJ/m^3 must still maintain a maximum exit velocity of 122 m/s. For air-assisted flares, the minimum required flare gas LHV is also stated as 11.2 MJ/m^3, however no upper LHV limited is provided. The maximum permitted exit velocity in meters per second is defined with the following equation (where $\mathrm{LHV_{FG}}$ has units of MJ/m^3):

$$V_{\max} = 8.706 + 0.7084 \times \mathrm{LHV_{FG}} \tag{1.2}$$

According to 40 CFR § 60.18, the compliance of flare operators to the 5 minute limitation on visible emissions is to be evaluated based on Method 22 of the United States Environmental Protection Agency (EPA) collection of test methods. Method 22 is a qualitative test procedure for the visual determination of fugitive emissions from stationary sources and smoke emissions from flares [37]. The purpose of this test method is to determine the duration of time in which visible emissions from the flare stack are present in an observation period of 2 hours. It is important to note that the severity of the flare emissions in terms of opacity levels is not recorded during this observation period. Over the past few decades, the EPA has taken a prominent role in enforcing regulatory compliance of flare operations. Through their inspection programs, such as the utilization of Method 22, the EPA have encountered

many cases of over-assisted flaring where operators have completely extinguished the flare with the excessive injection of air or steam in their attempt to eliminate visible emissions [38]. As a result of over-aeration and over-steaming of the flare, significant amounts of flare gas including hazardous VOCs have been inadvertently released into the atmosphere. The EPA has urged flare operators to abide by the flare manufacturer's guidelines on the steam to flare gas ratio, which typically ranges between 0.05 and 5 kg of steam per kg of flare gas [38]. Flare operators who are found violating federal flare requirements are liable to penalties of up to $37,500 per day for each violation [38].

Another important piece of federal regulation that concerns assisted flaring is 40 CFR § 63.670 on flare requirements in the context of refinery-based air pollution [39]. According to this statute, a flare operator must demonstrate that the flare, whether assisted or non-assisted, operates at a combustion efficiency of ≥ 96.5%. To prove compliance of this threshold, the flare operator is required to prepare and complete a site-specific flare performance evaluation test that includes taking emission samples, analyzing the samples for pollutant species, and calculating combustion efficiencies. No specific test protocol is suggested by the statute, and instead, the flare operator is to rely on their discretion. Based on the test results, flare-specific operating limits in regards to flare gas and assist flow rates are to be developed to meet the minimum allowed combustion efficiency of 96.5%.

1.3 Industry- and Government-Led Studies on Steam-Assisted Flaring

Ever since its inception in 1970, the EPA has been involved in studying the effectiveness of flaring in safely disposing of waste hydrocarbon gases. They published a number of reports addressing the reliability of assisted-flaring and its role in ensuring acceptable flare performance. A landmark study for the EPA was performed in 1983 by McDaniel [40], which looked at the effect of steam-assist on combustion efficiency and the emissions of CO_2, CO, total unburned hydrocarbons (THC), NO_x, and soot, using crude propylene as the flare gas (*i.e.*, 80% propylene and 20% propane). The study was instrumental in providing the EPA with a benchmark

for emission indices (*i.e.*, the mass of a chemical species produced per unit mass, energy, or volume of flare gas sent to the flare) of CO, THC, NO_x, and soot. Based on McDaniel's results, the EPA released its latest elevated flare emission indices for these species in its recent update of the industrial flares chapter as part of the fifth edition of its AP-42 publication on air pollutant emissions [41]. McDaniel performed the tests at the John Zink flare test facility in Tulsa, Oklahoma using an industrial flare stack with height and inner diameter (ID) of 3.75 m and 0.22 m, respectively. The exit area for the steam jet was 12.4 cm^2 while the exit area for the flare gas was 174.2 cm^2. A probe was suspended above the flare stack for taking samples of the exhaust. The aim of McDaniel's study was to establish a comprehensive set of emissions data by varying the operating conditions to better represent a realistic steam-assisted flaring scenario. Therefore, McDaniel collected samples of the exhaust while varying the LHV of the flare gas, which was done by diluting the crude propylene gas mixture with nitrogen, the flare gas flow rates, and the steam flow rates. The primary categorization of the experiments was based on the flare gas LHV: 81.3 MJ/m^3 for the experiments utilizing only crude propylene as the flare gas and an average of 12.0 MJ/m^3 for those in which crude propylene was diluted with nitrogen. For the high LHV cases, which are shown in Figure 1.3a, McDaniel [40] recommended steam-to-flare gas mass flow ratios (MFR) ranging between 0.4 and 1.5 for optimal combustion efficiencies of $\geq$ 99.8% and up to 3.6 for acceptable combustion efficiencies of $\geq$ 96.5%. For the experiments utilizing nitrogen-diluted crude propylene, as shown in Figure 1.3b, McDaniel's experiments were not conclusive in terms of what an acceptable steam-to-flare gas MFR would be. From the limited data provided, however, a steam-to-flare gas MFR of up to 0.17 appeared to provide a combustion efficiency greater than 96.5%.

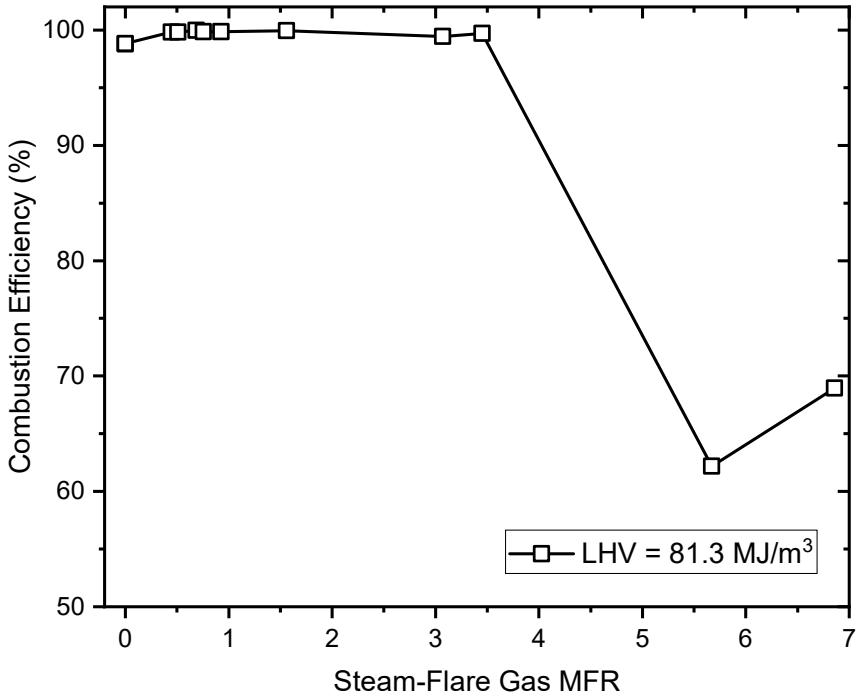

(a)

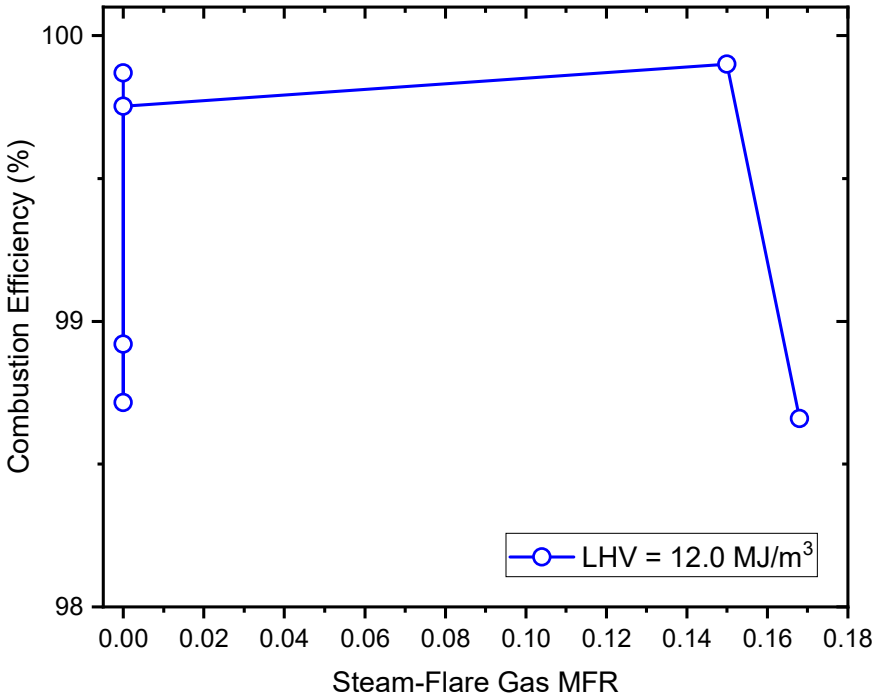

(b)

Figure 1.3: Combustion efficiency of a steam-assisted flare burning (a) crude propylene with an LHV of 81.3 MJ/m^3 and (b) nitrogen-diluted crude propylene with an average LHV of 12.0 MJ/m^3 from a study by McDaniel [40].

For each of the test points shown in Figure 1.3, McDaniel measured volume concentrations of THC, CO_2, CO, and NO_x. Emission indices for these species, denoted as EI_{THC}, EI_{CO_2}, EI_{CO}, and EI_{NO_x}, respectively, were calculated and are shown in Figure 1.4 (note the change in scale needed for the two LHV flare gases). The maximum emission indices for these species for the two LHV regimes with a combustion efficiency of $\geq 96.5\%$ were calculated and are shown in Table 1.2. McDaniel also took samples of the flare exhaust products to analyze the soot content at varying levels of smoke visibility. Due to inconsistencies in the tracer method used to determine the dilution ratio of the sampling system, McDaniel represented the soot yields in terms of mass of soot per volume of exhaust products, rather than per volume of flare gas burned. Flares producing light, average, and heavy amounts of smoke resulted in soot emission concentrations of 40, 177, and 274 μg/L, respectively. In attempting to convert these soot concentrations into emission indices, McEwen and Johnson [42] made the assumption that the soot samples were undiluted and used simple stoichiometry to generate indices of 0.9, 4.2, and 6.4 g soot/m^3 flare gas for the increasing levels of smoke, respectively.

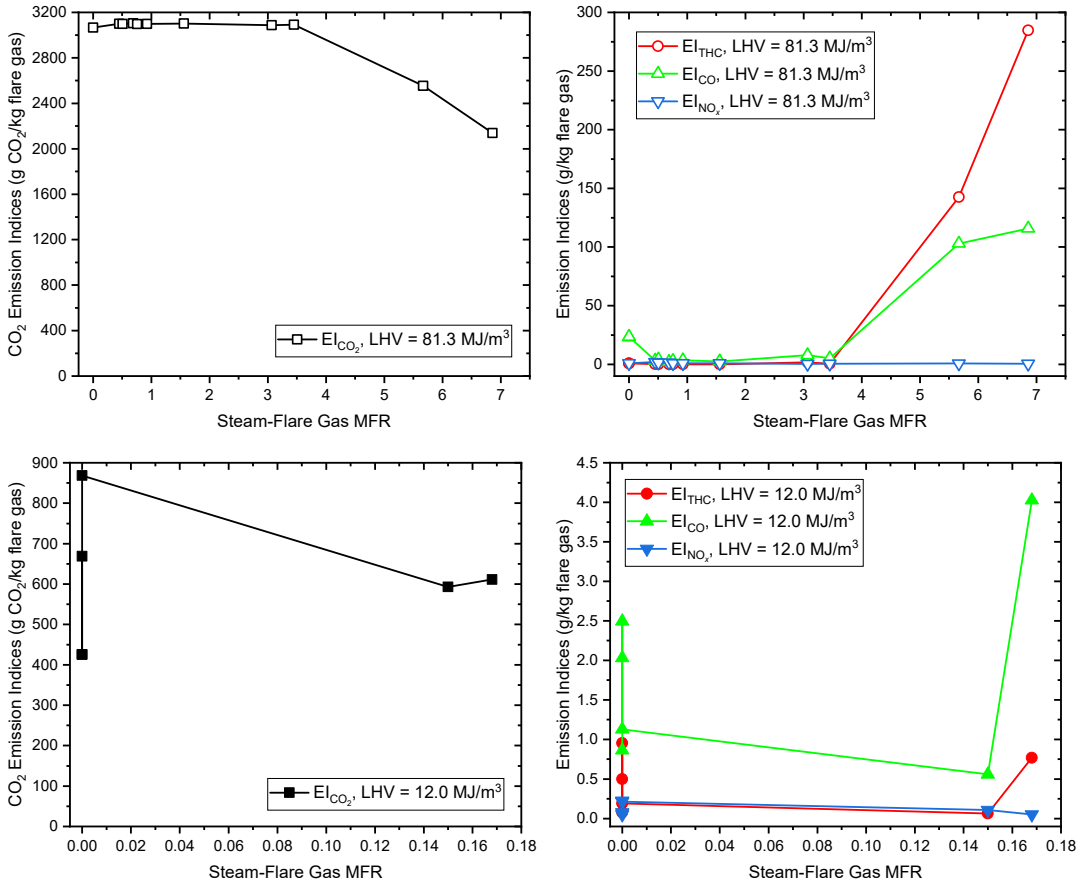

Figure 1.4: Emission indices of a steam-assisted flare burning flare gas with an LHV of 81.3 MJ/m^3 and 12.0 MJ/m^3 from a study by McDaniel [40].

As a result of the uncertainty in some of the results presented by McDaniel [40] related to the challenges McDaniel faced in closing the carbon mass balance of the flare plume with a tracer method and the scarcity in soot measurements, the EPA pursued further experimental work to better understand assisted flaring. In 1984, Pohl *et al*. [43] conducted a series of tests at the EPA's flare test facility in El Toro, California, which featured an exhaust capture hood for sampling the entire flare plume and screens to protect the flame from the effects of crosswinds. Experiments were performed on 8.9, 16.8, and 32.5 cm outer diameter (OD) pilot-scale flares using nitrogen-diluted propane as the flare gas with and without steam-assist. The flares were of basic design, consisting of a simple pipe with flare gas exit areas of 47.4, 201.3, and 766.5 cm^2, respectively. Four, eight, and sixteen steam injection nozzles were utilized with the increasing flare stack diameter, having 1.0, 1.3, and 1.6 cm

ODs, respectively. The steam nozzles were positioned outside of the pipe but with tips pointing at an angle of 60° above the exit plane of the flare and into the base of the flame. A wide range in the flow conditions were tested, including flare gas LHVs ranging from 10.1 – 87.6 MJ/m^3, flare gas exit velocities varying from 0.06 – 130.5 m/s, Reynolds numbers between 337 – 217 000, Richardson numbers between 2.9×10^{-5} – 8×10^2, and steam-to-flare gas MFRs ranging from 0 – 1. The Reynolds number is defined as the ratio of characteristic inertial to viscous forces of the flare gas at the flare exit, whereas the Richardson number is the ratio of buoyant to inertial forces. Although the flares were outfitted with steam nozzles, few tests were actually performed with steam injection. The most comprehensive steam-assist experiments were performed on the 8.9 cm OD flare burning a mixture of 56% propane and 44% nitrogen with an LHV of 49.3 MJ/m^3, in which Pohl *et al*. [43] found that for a combustion efficiency ≥ 96.5% the optimal steam-to-flare gas MFR range was 0 − 1. Pohl *et al*. [43] further stated that steam-to-flare gas MFRs greater than 0.5 constituted an over-steaming scenario, even though the maximum steam-to-flare gas MFR of 1 tested on the 8.9 cm flare yielded a combustion efficiency of 98.9%. This revealed the inconsistency between McDaniel [40] and Pohl *et al*. [43] in defining over-steaming scenarios with respect to combustion efficiency. The combustion efficiency values for the 8.9 cm OD steam-assisted flare experiments are shown in Figure 1.5.

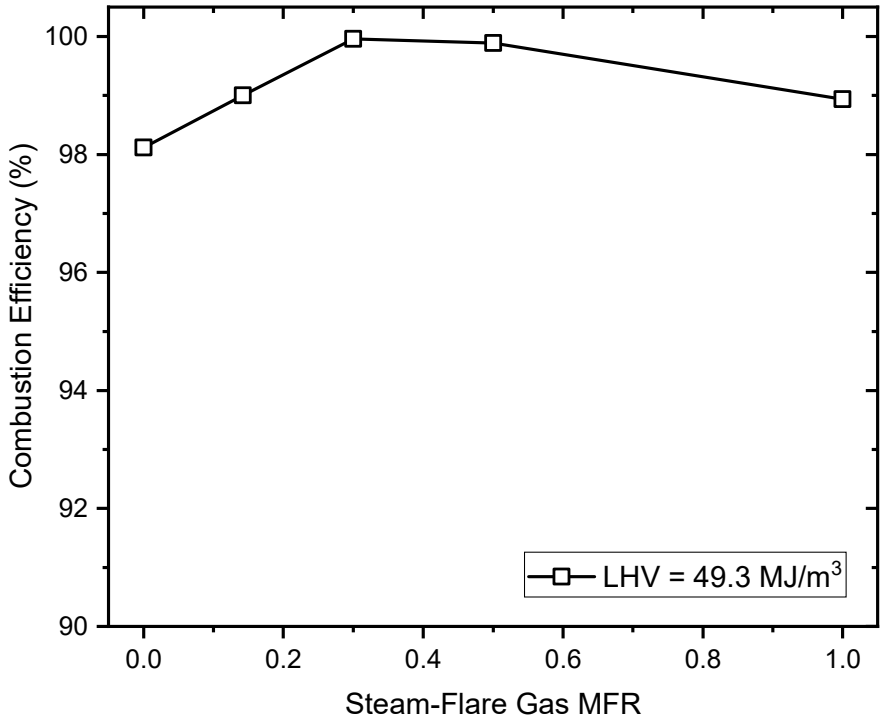

Figure 1.5: Combustion efficiency of a steam-assisted flare burning a propane and nitrogen mixture with an LHV of 49.3 MJ/m^3 from a study by Pohl *et al*. [43].

With regards to emissions, Pohl *et al*. [43] found that the injection of steam was highly effective in suppressing soot production. Unfortunately, Pohl *et al*. did not provide pollutant emission indices. Rather, the primary aim of the study was to correlate the combustion efficiency of the flame with parameters such as flame length, lift-off height, and stability in order to investigate the possibility of scaling up pilot-scale flare results to commercial flares. Overall, Pohl *et al*. [43] found that the combustion efficiency of the flare did not depend on the flare diameter and that results from the pilot-scale flares were comparable to commercial flares. An important parameter that was studied by Pohl *et al*. and is relevant to the current study is flame stability, which is defined as the ability of a flame to remain ignited over a range of fuel and oxidant flow conditions [44]. Pohl *et al*. [43] established the flame stability limits for each flare head—the point at which the flame becomes extinct—by dropping the LHV of the flare gas for a set gas exit velocity until the flame went out. This was accomplished by increasing the nitrogen-to-propane ratio of the flare gas.

Combustion efficiencies were determined near the flame stability limit and it was found that an increased proximity to this limit correlated to lower efficiencies.

Pohl and Soelberg [45] extended the work started by Pohl *et al*. [43] on a new array of pilot-scale and industrial flares. A steam-assisted industrial Coanda flare was tested, which purportedly used the Coanda effect to draw more air towards the flare gas for better combustion [46]. The Coanda flare head was tulip-shaped with an equivalent diameter of 30.5 cm, an open flare gas exit area of 729 cm^2, and had steam injection ports equipped. As with Pohl *et al*., the stability limit was determined using a propane and nitrogen flare gas mixture. Combustion efficiencies were determined at flare gas exit velocities between 0.06 − 3.02 m/s, with the nitrogen-diluted flare gas containing an average of 15.5% propane and having an average LHV of 13.6 MJ/m^3. Although the tests were performed close to the established stability limit of the flare, the range in steam-to-flare gas MFR of 0 − 3.3 did not encompass an over-steaming scenario, as is evident from Figure 1.6, where combustion efficiencies remained above 96.5%.

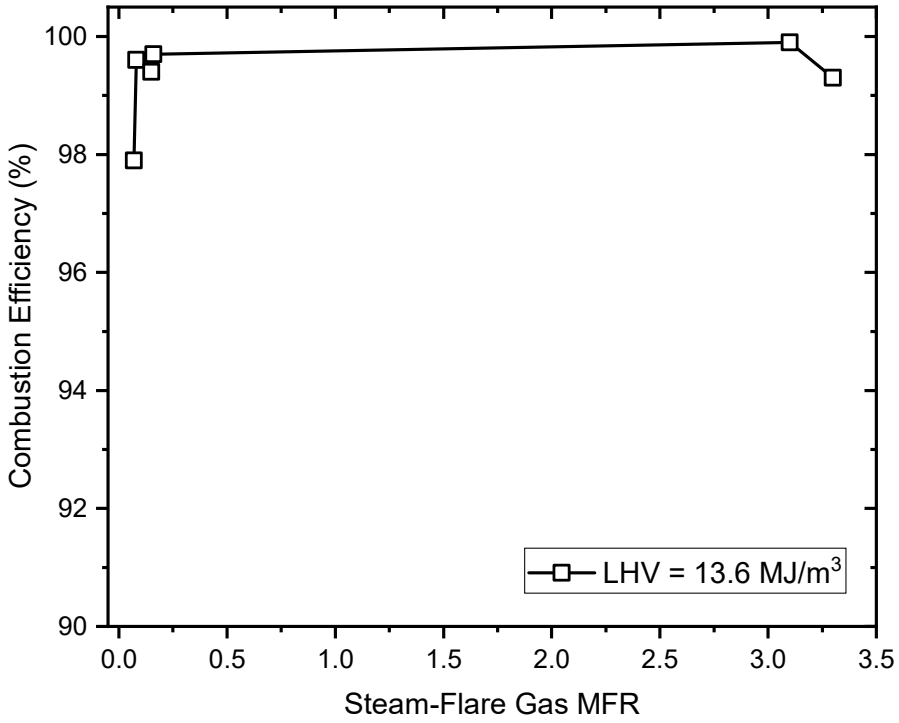

Figure 1.6: Combustion efficiency of a Coanda steam-assisted flare burning a propane and nitrogen mixture with an LHV of 13.6 MJ/m^3 from a study by Pohl and Soelberg [45].

As shown in Table 1.2, the only emissions data provided by Pohl and Soelberg [45] were for NO_x. However, this data was only provided for three test cases having an average flare gas propane content of 18%, LHV of 15.8 MJ/m^3, and combustion efficiency of 99.7%. The maximum NO_x emission index for these tests was 0.03 g NO_x/kg flare gas, which can also be represented as 0.14 g NO_x/kg C_3H_8. The main conclusions from Pohl and Soelberg [45] were in regards to the differences in the aerodynamics of pilot- and industrial-scale flares. As the diameter of the flare stack decreased, the exit Reynolds and Richardson numbers were found to decrease as well. Based on the findings of Pohl and Soelberg [45], pilot-scale flares with diameters of 2.54 cm and 3.81 cm and commercial flare stacks with diameters of 30.5 cm and 61 – 122 cm operated in a Reynolds and Richardson number regime as shown in Table 1.1.

Table 1.1: Reynolds and Richardson number operating regimes for pilot-scale and commercial flare stacks based on Pohl and Soelberg [45].

Flare stack diameter (cm)	Reynolds number regime	Richardson number regime
2.54, 3.81	$10^4 – 10^6$	$10^{-6} – 10^{-1}$
30.5	$10^3 – 10^5$	$10^{-1} – 10^3$
61 – 122	$10^3 – 10^7$	$10^{-5} – 10^4$

The most recent major study on steam-assisted industrial flares was conducted by Allen and Torres [47] in 2010 for the Texas Commission on Environmental Quality (TCEQ). Due to the concern regarding the violation of flaring regulations with over-steaming and over-aeration, the TCEQ was interested in performing field tests in conditions comparable to the offending flares. In view of this, Allen and Torres [47] completed a project at the John Zink flare test facility in Tulsa, Oklahoma with the aim of assessing the impact of steam-assist on the combustion efficiency of an industrial flare operating at low flare gas flow rates and LHVs. The full-scale tests were performed outdoors with ambient conditions being an uncontrolled variable. For the steam-assisted flare tests, a single steam flare design was selected that was representative of those found in the field. The steam-assisted flare stack had a tip diameter of 91.4 cm with a height of 4 m above the ground and with both center and upper steam nozzles equipped. The flare gas mixture was composed of a 1:4 natural gas to propylene ratio by volume, with nitrogen added as a diluent to achieve a specific LHV. To simulate a flaring scenario susceptible to over-steaming, most of the tests were performed with an LHV of 13.0 MJ/m^3, being close to the minimum value recommended by 40 CFR § 60.18 of 11.2 MJ/m^3. For comparison purposes, some tests were also performed with an LHV of 22.4 MJ/m^3. Flare gas flow rates were also kept at the low end of the flare design capacity of 425 020 kg/hr and were set to either 425 kg/hr or 1 062 kg/hr, corresponding to 0.1% and 0.25% of total capacity, respectively. These low flare gas LHV and flow rate settings posed a higher risk of over-steaming due to the flare manufacturer's minimum recommended steam assist quantity of 567 kg/hr (*i.e.*, 227 kg/hr center steam and 340 kg/hr upper steam), which corresponded to minimum steam-to-flare gas MFRs of 1.3 and 0.5 for the low and

high flare gas flow rate test cases, respectively. To comply with the 40 CFR § 60.18 restriction on visible emissions, Allen and Torres [47] bracketed the low end of the steam assist flow rate range by the incipient smoke point and the higher end by flame extinction. The incipient smoke point was defined as the operating condition at which the minimum steam flow rate yielded a flare with no visible smoke emissions at a distance of two flame lengths from the flare tip [47]. For the test cases where the flare gas composition was set to an LHV of 13.0 MJ/m^3, the recommended steam-to-flare gas MFRs for a combustion efficiency ≥ 96.5% was 0.25 and 0.32 for the low and high flare gas flow rates, respectively. These values were considerably lower than the steam-to-flare gas MFRs of 1.3 and 0.5 suggested by the flare manufacturer. The only test condition that satisfied the minimum recommended flare manufacturer steam flow rate was at the high flare gas flow rate and LHV settings of 1 083 kg/hr and 22.8 MJ/m^3, in which a combustion efficiency of ≥ 96.5% was sustained beyond an MFR of 0.5 and up to 0.84. This substantiates the concerns that the EPA [38] and Allen and Torres [47] stated regarding the potential for over-steaming in industry, particularly when the flare gas approaches the minimum allowable LHV as per 40 CFR § 60.18. The combustion efficiency trends for the low and high LHV tests are shown in Figure 1.7. In comparing the difference in effects of center and upper steam on flare performance, Allen and Torres [47] found that combustion efficiency was more sensitive to center steam as a result of it diluting the flare gas prior to combustion. Allen and Torres [47] also provided THC emission indices for five test conditions with combustion efficiencies ranging from 88% to 100% as shown in Figure 1.8. The maximum THC emissions for a combustion efficiency ≥ 96.5% was 5.29 g THC/kg flare gas as listed in Table 1.2. A separate series of tests burning a propane, natural gas, and nitrogen mixture were conducted for measuring NO_x emissions. The average flare gas LHV for these tests was 13.4 MJ/m^3 with NO_x emissions generally decreasing as the steam-to-flare gas MFR increased, as shown in Figure 1.9. The maximum NO_x emissions generated for a combustion efficiency ≥ 96.5% was 0.17 g NO_x/kg flare gas. Although Allen and Torres measured BC mass concentrations during some of the steam-assisted tests, they did not specify a BC emission index. Based on the data they collected, however, Fortner *et al*. [48]

estimated a BC emission index of 0.016 g BC/kg flare gas at a combustion efficiency of 96.5%.

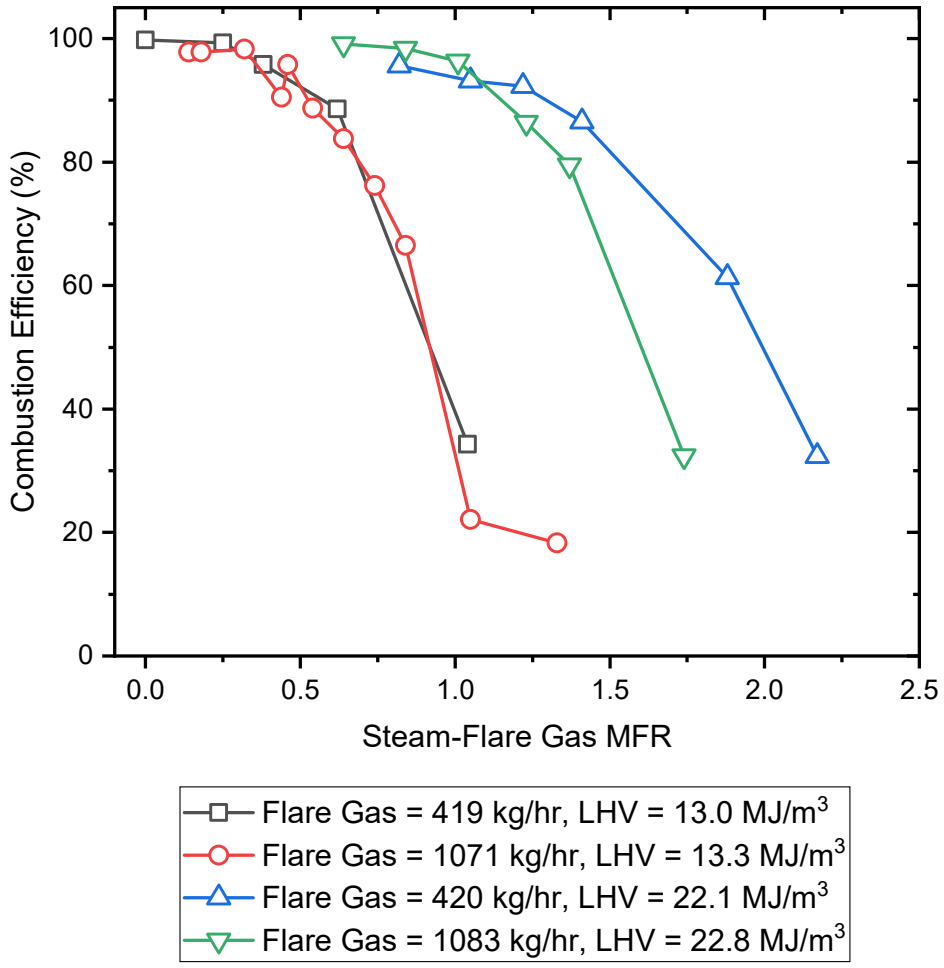

Figure 1.7: Combustion efficiency of an industrial flare with center and upper steam-assist burning high and low flare gas flow rates and LHVs from a study by Allen and Torres [47].

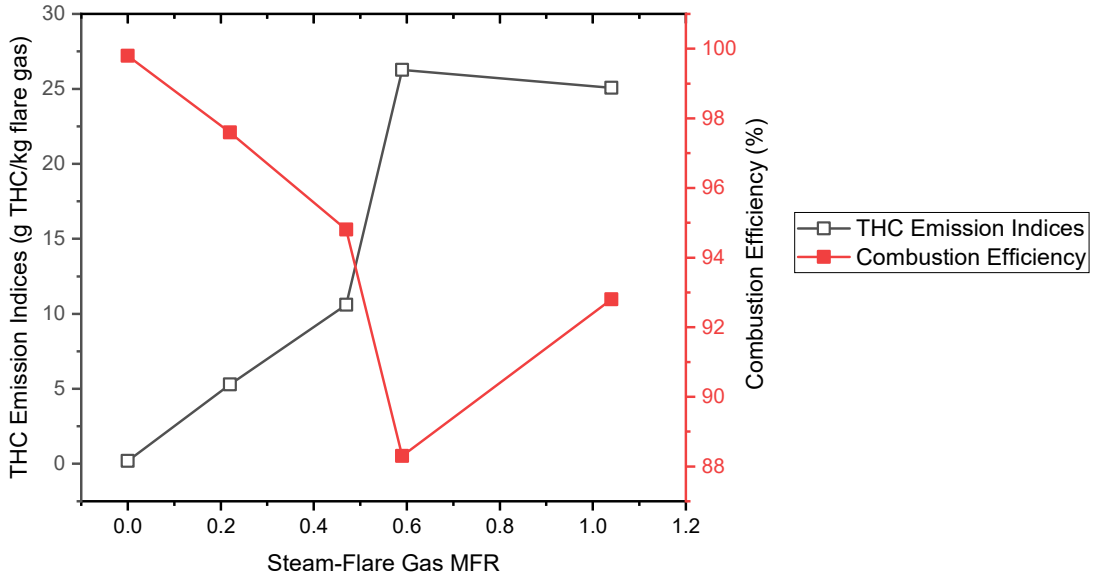

Figure 1.8: THC emission indices and corresponding combustion efficiencies for steam-assisted flare tests performed by Allen and Torres [47].

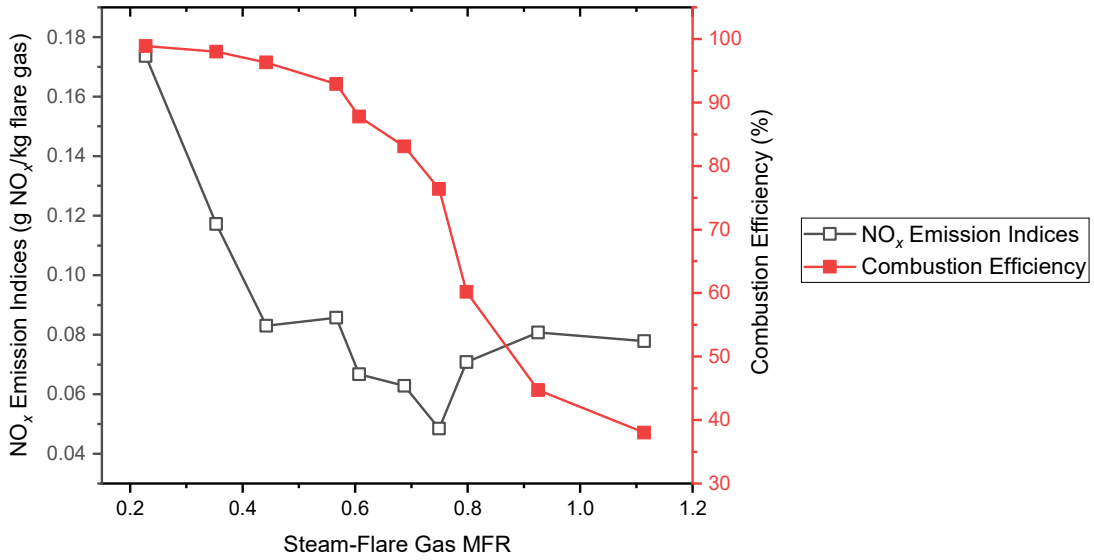

Figure 1.9: NO_x emission indices and corresponding combustion efficiencies for steam-assisted flare tests performed by Allen and Torres [47].

Table 1.2: Maximum pollutant emission indices for steam-assisted flares based on a combustion efficiency of ≥ 96.5% from studies by McDaniel [40], Pohl and Soelberg [45], and Allen and Torres [47].

Study Authors	Average Flare Gas LHV (MJ/m^3)	Species Emission Indices (g/kg flare gas)				
		THC	CO_2	CO	NO_x	BC
McDaniel	81.3	1.76	3 103	23.44	1.88	-
	12.0	0.96	869	4.03	0.23	-
Pohl and Soelberg	15.8	-	-	-	0.03	-
Allen and Torres	13.1	5.29	-	-	-	-
	13.9	-	-	-	0.17	-
	22.1	-	-	-	-	0.016

1.4 Objectives

Due to the lack of reliable quantitative guidelines for achieving steam-assisted flaring operation at an acceptable combustion efficiency and reduced soot emissions, as well as the uncertainty regarding the potential pollutant emissions that can result from an improperly operated steam-assisted flare, a comprehensive and in-depth analysis of the relation between steam and combustion is required. The main goal of the current study was to evaluate the extent to which the injection of steam into a flame improved the combustion efficiency and reduced harmful emissions, as suggested by flare manufacturers and industry bodies. Considering the numerous variables involved in the performance of a real-world industrial-scale steam-assisted flare, this endeavour was undertaken within a controlled lab-scale experimental framework. The current study was performed as part of the Natural Sciences and Engineering Research Council of Canada (NSERC) FlareNet Strategic Network at the University of Alberta. The main research objectives were as follows:

1. Design and build a lab-scale flare facility for performing controlled combustion experiments with the capabilities of capturing and analyzing the exhaust products for measuring the combustion efficiency and pollutant emissions.
2. Devise and implement a method of delivering a known and controllable quantity of steam to the lab-scale flare and implement an injection methodology that conforms to standard industry practices.

3. Generate combustion efficiency and emissions data for a range of steam-assist operating conditions by varying the fuel type, flare gas flow rate, and steam injection method.
4. Explore trends in the combustion efficiency and emission data as operating parameters are varied and compare the experimental results to data that has been established by government and industry.

In Chapter 2, a detailed description of the experimental setup will be provided, including the burner design, facility layout, and equipment and diagnostic instruments required to perform the experiments. Chapter 3 will consist of the experimental results and a discussion of the implications of using steam to improve flare performance. Finally, conclusions from the current study and suggestions for improvements to the approach and methodologies taken in the study will be presented in Chapter 4.

Chapter 2

2. Experimental Setup

2.1 Lab-Scale Flare Design

With the wide variation in steam-assisted flare designs present in industry—most of which are inaccessible due to being proprietary in nature—the goal in constructing a lab-scale flare was to maintain a simple design that would allow for the underlying physics of an assisted flaring process to be analyzed. To accomplish this, a coflow burner design was opted for as an attempt to incorporate the main elements of the different steam-injection methodologies while at the same time enabling highly repeatable experiments that were easy to perform and compare. The coflow design was established as two coaxial tubes with coincident exit planes that allowed for either the steam to flow through the inner tube and fuel gas through the annular space between the tubes or vice versa. This approach allowed the comparison of the effect of steam injection location, either within or outside the flame combustion zone, on combustion efficiency and pollutant emissions. As can be seen in Figure 2.1, the coflow strategy was implemented by the use of two concentric stainless-steel tubes with flush exit planes. The outer tube had a 25.4 mm OD, a 22.9 mm ID, and a length of 305 mm. The bottom of the outer tube was connected to a three-way tee threaded pipe fitting. As will be discussed later in further detail, part of the experimental parameter variation was to test the burner performance using two inner tube diameters. All sets of experiments except for one were performed with an inner tube having a 12.7 mm OD, 11.3 mm ID, and length of 457 mm. The alternate inner tube had a 6.35 mm OD, 5.54 mm ID, and a length of 457 mm. The inner tube was inserted inside

the tee and outer tube and fitted to the bottom of the tee. Three set screws positioned 120° apart were inserted through threaded holes halfway down the length of the outer tube to align the position of the inner tube such that its centerline coincided with that of the outer tube. The bottom of the inner tube could then be connected to the fuel or steam line to accommodate for inner coflow. For the outer coflow, the fuel or steam line was connected to the side inlet of the tee, which provided access to the annular space between the outside wall of the inner tube and inside wall of the outer tube for the medium to flow.

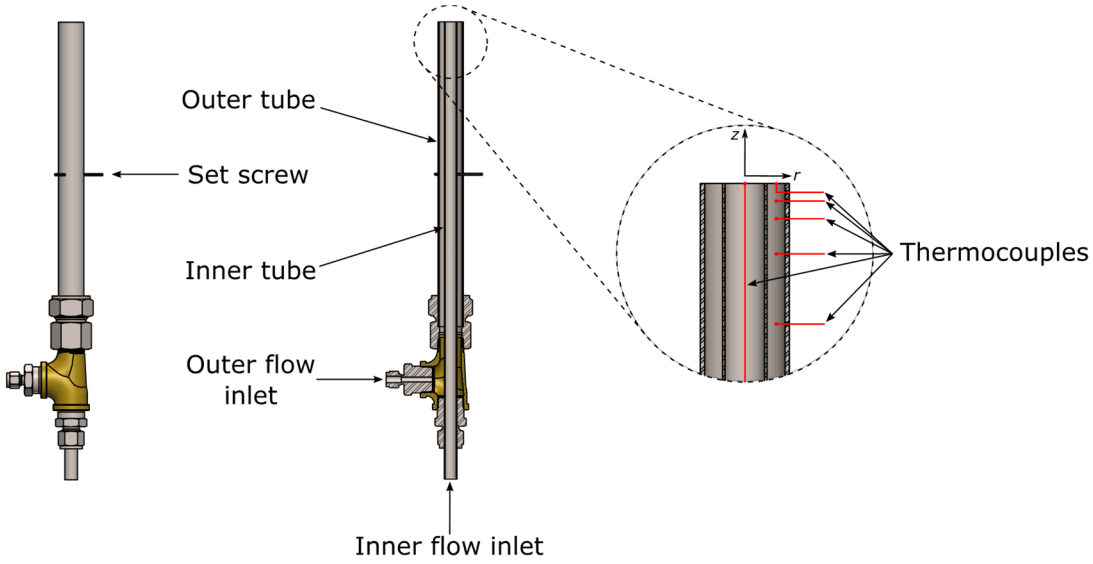

Figure 2.1: Front view of the burner along with a section view showing the inner and outer flow inlets and pathways. A close-up of the tip of the burner is presented to show the locations of the thermocouples placed inside the inner tube and in the annular space between the inner and outer tubes. A coordinate axis is shown above the tip of the burner, with z pointing in the upward axial direction and r pointing in the radial direction.

Also shown in Figure 2.1 is the thermocouple arrangement near the tip of the burner. For measuring the temperature of the inner coflow at the tip of the burner, an exposed junction T-type thermocouple (Omega Engineering, TSS Series) was used, having a wire diameter of 0.81 mm and sheath OD of 1.59 mm. The thermocouple was inserted into the inner tube through the inlet such that it was parallel to the flow and with the junction positioned at axial and radial coordinates of (r, z) = (0, 0), respectively. To gain access to the annular space close to the burner tip between the

inner and outer tubes for temperature measurement. five holes with 0.91 mm diameter were drilled through the outer tube wall at z = −2.5, −5, −10, −20, and −40 mm. Exposed junction T-type thermocouples (Omega Engineering, 5SRTC Series) with a wire diameter of 0.13 mm were inserted into each hole. The topmost thermocouple was bent upwards at a 90° angle such that the junction coordinate position was r = 8.9 mm and z = 0 mm. The remaining thermocouples were placed perpendicular to the flow with the same radial position. The radial position of r = 8.9 mm was the midway point in the annular gap between the inner and outer tube walls. All thermocouple junctions were covered in aluminum foil to minimize the extent to which radiation from the flame affected temperature measurements. To capture the temperature measurements, the thermocouples were wired to a data acquisition module (National Instruments, NI-9213), which sampled the temperature with an overall bias uncertainty of ±1 °C. Refer to Appendix A for a description of the uncertainty analysis methodology including bias and precision uncertainties.

2.2 Lab-Scale Flare Test Facility

Steam-assisted flaring experiments were performed in the flare test facility shown in Figure 2.2. The main functions of the facility were to provide the means to perform combustion experiments while being able to vary the input parameters, collect and mix the combustion exhaust products, and analyze these products with specialized diagnostic instruments. The burner was mounted and bolted on two horizontal aluminum rails which were in turn bolted to an aluminum support frame. The height of the burner was adjusted by raising or lowering the position of the rails on the frame. For all experiments completed in this study, the height of the tip of the burner from the floor was set at 84.9 cm.

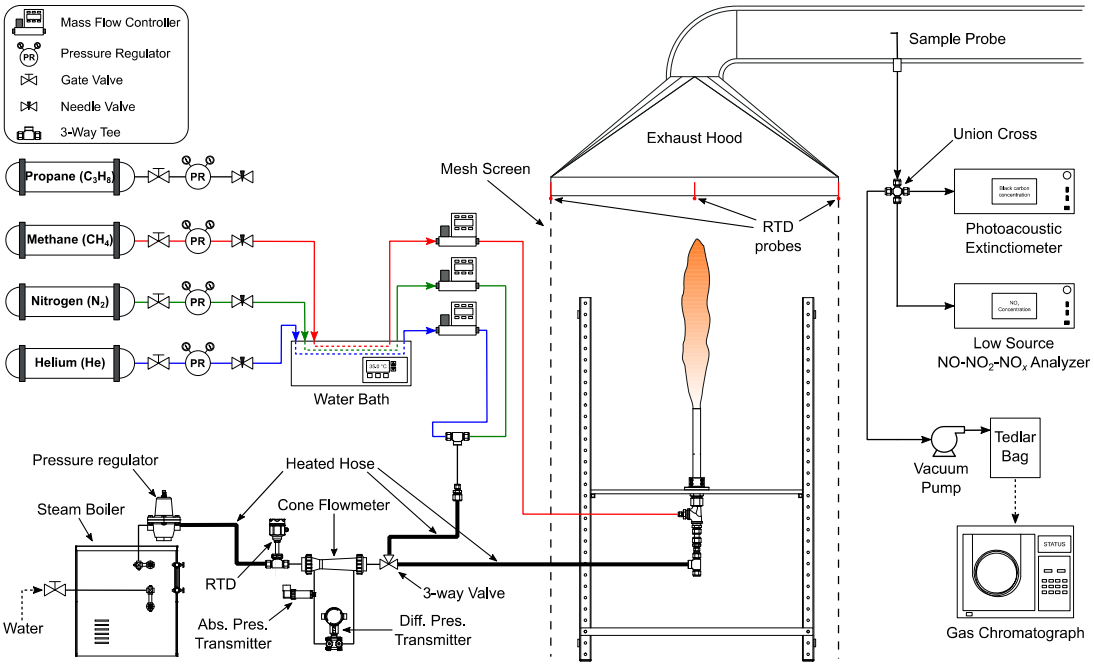

Figure 2.2: Flare test facility for conducting experiments with the lab-scale steam-assisted flare.

The fuel gases used in simulating a flare were 99.97% pure methane (Praxair, ME 3.7UH-T) with an LHV of 32.8 MJ/m^3 and 99.5% pure propane (Praxiar, PR 2.5IS-FX) with an LHV of 84.9 MJ/m^3. The fuel gas cylinder in use was connected with 12.7 mm OD, 9.53 mm ID plastic tubing to a 12.7 mm OD, 11.1 mm ID, 3.81 m length of coiled copper tubing resting in a water bath (Thermo Fisher Scientific, TSCIR35) set to 35 °C, as shown in Figure 2.2. The purpose of the heated water bath was to maintain the gas at close to the room temperature of 23 °C. Once exiting the water bath, the gas was connected using the same plastic tubing to a 50 SLPM (standard liters per minute corrected to 25 °C and 101.3 kPa) mass flow controller (Alicat, MCR 50 SLPM) for metering out the fuel gas, with an uncertainty of ± (0.1 SLPM + 0.8% of reading). The plastic tubing was again used to connect the mass flow controller outlet to the outer or inner burner tube inlets. Since the mass flow controller was only factory-calibrated with air, the calibration was rechecked for CH_4 and C_3H_8 using a drum-type gas meter (Ritter, TG50) as described in Appendix B. The uncertainties were found to fall within the range stated by the manufacturer.

To enable steam coflow in the burner, an 18 kW electric steam boiler (Sussman, MBA18) with a maximum steam generation capacity of 408 g/min was

used. The internal pressure limit of the boiler was set to 207 kPa, while the external pressure-regulating valve (McMaster-Carr, 4674K63) with a range of 14 – 207 kPa was used to adjust the steam flow rate. In order to elevate the steam from a saturated to superheated state and maintain it at this condition, a 6 m long heated hose (Dekoron Unitherm, Series 200) was connected to the outlet port of the pressure-regulating valve and set to a temperature of 155 °C. By maintaining the steam at a superheated state, the problem of having to measure the mass flow rate of a multiphase flow (*i.e.*, wet saturated steam with a quality, x, of $0 < x < 1$) was alleviated. The end of the heated hose was connected to the inlet port of a three-way tee, in which an RTD probe (Spirax Sarco, EL2270) with a full scale measurement range of −50 – 500 °C and uncertainty of ± (0.15 °C + 0.2% of reading) was connected to one of the tee outlet ports for measuring steam temperature. The remaining port was connected to an obstruction-type flow meter (Cameron, NuFlo Cone Meter), which was a central component of the steam flow pathway that allowed for steam flow rates to be measured. This was accomplished by a cone-shaped element contained within the pipe construction of the cone flow meter that generated a pressure differential across the element during steam flow. High- and low-pressure ports located upstream and downstream of the cone element, respectively, were hydraulically connected to a differential pressure transmitter (ABB, 2600T) having a full measurement scale of 16 kPa and uncertainty of ± 0.012 kPa. In order to confirm the superheated nature of the steam at the flow meter, an absolute pressure transducer (Omega, PX409-100AI) with a full scale of 689 kPa and uncertainty of ± 0.551 kPa was installed in-line with the high-pressure impulse tubing connecting the flow meter and differential pressure transmitter. The flow meter outlet was then connected to a three-way valve with the default valve position allowing the steam to flow through a secondary 6 m long heated hose with the same 155 °C setpoint. The hose exit was then fitted to either the inner or outer burner flow inlets whether inner or outer steam coflow, respectively, was required.

The steam temperature, absolute pressure, and differential pressure measurements were taken by temperature and electrical current input data acquisition modules, respectively (National Instruments, NI-9216 and NI-9203). Data from the

steam instrumentation and the physical parameters of the cone flow meter were used to generate steam mass flow rates using LabVIEW based on the methodology outlined in ISO 5167-5 [49]:

$$\dot{m}_{\text{steam}} = \frac{C}{\sqrt{1-\beta^4}}\varepsilon\frac{\pi}{4}(D\beta)^2\sqrt{2\Delta p\rho_1} \tag{2.1}$$

where C is the discharge coefficient, β is the cone element size factor, ε is the expansion factor for steam based on differential pressure, D (m) is the cone flow meter ID, Δp (Pa) is the differential pressure across the cone element, and ρ_1 (kg/m^3) is the density of steam based on temperature and absolute pressure. To verify the steam mass flow rates generated by Eq. (2.1), a separate set of experiments involving a plate heat exchanger for condensing and measuring the steam condensate were performed to calibrate the cone flow meter, which yielded a calibration range of 14 – 100 g/min. The lower bound of this range was limited by the onset of steam flow instabilities at < 14 g/min, whereas the upper bound was experimentally determined to be sufficient for meeting the objectives of the study. Refer to Appendix C for more details regarding the steam mass flow rate calibration procedure.

One of the aspects of the present study was to investigate the claim made by the API [34] with regards to the unique effect that steam has in promoting complete combustion through the water-gas shift reaction. A strategy was devised to pull apart the potential chemical effect of steam on the combustion reaction from the hydrodynamic effect of an internal or external jet flow (*i.e.*, inner vs. outer steam coflow) on the flame. The idea was to perform a set of experiments where steam was partially or fully substituted by an inert gas mixture having the same molecular weight as water. The assumption was first made that the superheated steam could be approximated as an ideal gas, which was confirmed by calculating the compressibility factor of the steam at the burner tip, using the equation below, and discovering a negligible deviation from unity (*i.e.*, < 1.5%):

$$Z = \frac{pM}{\rho RT} \tag{2.2}$$

where p is the atmospheric pressure in the lab, M (g/mol) is the molecular weight of water, ρ is the density of steam at the burner exit, R (J/mol·K) is the universal gas constant, and T (K) is the temperature of steam at the burner exit. Using the ideal gas law, a gas mixture of 58% nitrogen (N_2) and 42% helium (He) was found to have the same molecular weight as water. As shown in Figure 2.2, N_2 at 99.998% purity (Praxair, NI 4.8-T) and He at 99.999% purity (Praxair, HE 5.0UH-T) were used to generate the "equivalent steam-assist" gas mixture. The N_2 and He gases were also piped through the heated water bath, in the same manner as described for the fuel gases, and were connected to their respective mass flow controllers. The mass flow controllers used for metering out N_2 and He had full scales of 100 SLPM (Alicat, MCR 100 slpm) with uncertainty of ± (0.2 SLPM + 0.8% of reading) and 50 SLPM (Alicat, MCR 50 slpm) with uncertainty of ± (0.1 SLPM + 0.8% of reading), respectively. To ensure the N_2 and He gas mixture was uniformly mixed when running the equivalent steam-assist experiments, a smaller, 6.35 mm OD, 4.32 mm ID plastic tubing was used to connect the N_2 and He mass flow controllers to a three-way tee and then to a 41.28 mm OD, 9.53 mm ID, and 3.66 m long heated hose (McMaster-Carr, 5565K63). The heated hose was required to ensure the gas mixture matched the temperature of steam when injected into the flame. A static mixer for the gas mixture was found to be unnecessary due to the narrow diameter of this plastic tubing allowing for turbulent flows. An average Reynold Number of 9 126 was calculated for the gas mixture flow rates tested in the plastic tubing upstream of the heated hose. As shown in Figure 2.2, the heated hose leads to the same three-way valve connected to the outlet of the cone flow meter. As a result, either steam or the N_2/He gas mixture can be selected as the coflow medium for the burner. Since the mass flow controllers were only factory-calibrated with air, each flow controller used in the experiment was calibrated for its respective gas using a drum-type gas meter (Ritter, TG50). The uncertainties were found to fall within the range stated by the manufacturer.

To ensure the products of combustion were fully captured, the burner and frame assembly was placed centrally beneath a square-profile exhaust hood with sides measuring 91 cm and a height of 213 cm above the floor. On each side of the exhaust hood, mesh screens were hung that reached the floor. The mesh screens, made of vinyl-coated polyester, had 1.59 mm square openings with a blockage ratio of 0.55. The presence of the mesh screens allowed for a uniform entrainment of combustion air while dampening the currents in the lab that would otherwise cause flame instability. Connected to the top of the exhaust hood was a circular duct with a 30 cm OD. A Venturi air control valve (Phoenix Controls) was installed inline with the duct and set to a duct flow rate of 17 m^3/min. The valve contains a cone assembly with a spring that expands or compresses to compensate for fluctuations in the duct pressure so that a constant flow rate is maintained. An air pressure proving switch was also installed on the side of the duct to trigger an alarm in the case that the exhaust fan failed. Based on the lab temperature and pressure conditions of 23 °C and 93.1 kPa, respectively, the duct flow rate was at a turbulent Reynolds number of approximately 78 000. As an extra measure of ensuring the entire plume of combustion products was captured, a Resistance Temperature Detector (RTD) probe (McMaster-Carr, 1237N12) was attached to each side of the exhaust hood with the tip extending 1 cm below the hood to detect the potential spillage of hot plume gases outside of the hood.

The extraction of the diluted combustion products was performed using a 6.35 mm OD L-shaped stainless-steel probe (opening pointed upstream) that was inserted into a port on the side of the duct located 6 m downstream of the exhaust hood. At this section in the duct, the combustion products were found to be independent of the radial position of the probe tip and therefore thoroughly mixed. A 2 m long, 1.59 cm OD copper tube with a union cross fitted to one end was welded at its free end to the outlet of the sample probe. The three remaining ports on the union cross were connected to a photoacoustic extinctiometer (Droplet Measurement Technologies, PAX) for BC mass concentration measurements, a NO_x analyzer (Thermo Scientific, 42iQLS) for NO_x concentration measurements, and a diaphragm vacuum pump (GAST Manufacturing, DOA Series) for filling a 10 L Tedlar bag

(Cole-Parmer, ESS Series) with combustion product to be analyzed using a gas chromatograph (Agilent, 7890B).

To minimize the electrostatic losses of BC during transportation from the sampling line to the PAX, a 9.53 mm OD, 6.35 mm ID, 4.5 m long static-dissipative silicone rubber tube (McMaster-Carr, 1909T7) was used to carry the combustion product. The PAX is equipped with an 870 nm modulated diode laser for directly measuring light absorption and scattering of aerosol particles, with this wavelength being most effective for BC particles. A pair of critical orifices restricts the flow rate of sample flow that is drawn into the instrument using an internal pump to 1 L/min. The flow enters a cell and is divided into two subflows that travel through a photoacoustic resonator and nephelometer for the measurement of light absorption and scattering, respectively. Within the photoacoustic chamber, the BC particles absorb energy from the laser and release it as heat, thereby generating pressure waves that are detected by a microphone and converted to an absorption coefficient. The nephelometer employs a light detector that picks up light scattered by the BC particles which is then converted to a scattering coefficient. Based on the following formula provided by Droplet Measurement Technologies [50], the developer of the PAX, the BC mass concentration with units of $\mu g/m^3$ can be calculated:

$$f_m = \frac{B_{\text{abs}}}{\text{MAC}} \tag{2.3}$$

where B_{abs} is the BC absorption coefficient (1/Mm) and MAC is the BC mass absorption cross-section (m^2/g). Based on a laser wavelength of 870 nm, the PAX manufacturer recommended a constant MAC value of 4.74 m^2/g with an uncertainty of ± 0.76 m^2/g. The uncertainty in f_m was also associated with the noise in the absorption coefficient which was found to be approximately 1% of the measured value. For background measurements, the PAX yielded zero or near-zero negative values for BC mass concentration. During the data collection process, therefore, only positive values for BC mass concentration were accepted as valid points.

The NO_x analyzer (Thermo Scientific, 42iQLS) was used to measure NO_x up to a concentration of 100 ppm with an uncertainty of ±1 ppm. The underlying operating principle of the NO_x analyzer is the chemiluminescent reaction between NO and O_3 which produces NO_2 at an excited state and O_2. In reverting to a lower energy state, the NO_2 molecules release infrared light. Once the sample is drawn into the instrument at approximately 0.1 L/min, a solenoid valve sends the flow either directly to a reaction chamber or through an NO_2-to-NO converter before being transferred to the reaction chamber. For the stream that directly enters the reaction chamber, the NO in the sample reacts with O_3 that is produced by an ozonator, which leads to the generation of the infrared light that is detected by a photomultiplier. The intensity of the light is proportional to the concentration of NO, which is then calculated as a concentration in ppb or ppm. The stream that is sent to the NO_2-to-NO converter first enters a stainless steel chamber that is heated up to 625 °C, allowing for the thermal degradation of NO_2 in the sample to NO. The product of this thermal reaction then passes onto the reaction chamber—now accounting for a NO concentration that is proportional to the total sample NO and NO_2 concentration—and generates infrared light proportional to the NO_x concentration in the sample. The difference between the NO_x and NO concentration yields the NO_2 concentration.

Unlike the PAX and NO_x analyzer, the gas chromatograph (GC) was operated offline. The combustion product samples stored in the Tedlar bags were drawn into the GC using a vacuum pump located downstream of the GC. The GC measured the mole concentration of C_1 – C_3 hydrocarbons, and non-hydrocarbons such as O_2, N_2, CO_2, CO, with a flame ionization detector (FID) and thermal conductivity detector (TCD), respectively. Gas cylinders containing these gases at concentrations varying by orders of magnitude were used to generate multi-point calibration curves. Refer to Appendix D for more details regarding the choice of calibration standards as well as the uncertainties in the gas concentration measurements. The FID uses a hydrogen-air flame that combusts the hydrocarbons contained in the sample, thereby generating ions. A metal collector detects the ions, which produces a current proportional to the amount of ions formed that is in turn dependent on the concentration of hydrocarbons in the sample. The current is then represented as a peak on a chromatogram for the

respective hydrocarbon. The TCD works by comparing the thermal conductivities of two different gas flows: a carrier gas such as H_2, He, or N_2 at high purity and the same carrier gas mixed with the sample gas. A filament within the detector is heated and maintained at a constant temperature while these two gas streams flow alternately over the filament. Due to the presence of a gas species other than the carrier gas and the difference in its thermal conductivity compared to the carrier gas, the power needed to maintain a constant filament temperature changes. This difference in power is correlated to the concentration of the respective species in the sample gas and shows up as a peak on the chromatogram.

2.3 Methodology for Calculating Carbon Conversion Efficiency and Emission Indices

To determine the carbon conversion efficiency (CCE) of combustion reactions at various burner operating conditions, a closed carbon mass balance was defined around the reaction as shown in Figure 2.3. The method of enclosing the combustion process with a control volume, accounting for all the inward and outward flows of carbon-containing species, was based on a derivation by Corbin and Johnson [51].

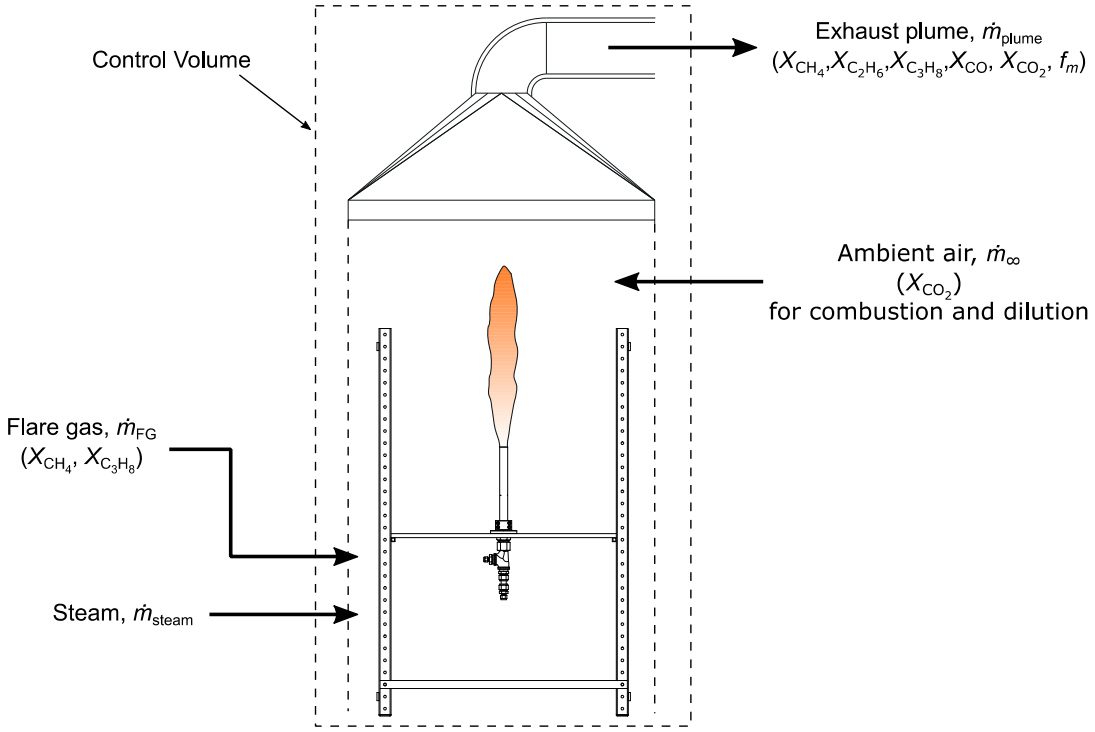

Figure 2.3: Establishing a closed carbon mass balance around the combustion reaction with the mole fractions of carbon-based gas species and the soot mass concentration characterized by X_k and f_m, respectively.

All potential carbon-containing species produced by the incomplete combustion of an arbitrary hydrocarbon, C_xH_y, can be represented by the following generic reaction:

$$C_xH_y + O_2 \longrightarrow bCO_2 + dH_2O + eCO + fCH_4 + \sum_{m,n} g_{m,n}C_mH_n + hC_{(s)} \qquad (2.4)$$

in which N_2 was omitted from the reactants side due to not participating in the oxidation of carbon, CO and $C_{(s)}$ (*i.e.*, soot or BC) are the incompletely oxidized carbon-based products, and CH_4 and C_mH_n are the unburned or reformed hydrocarbons. The CCE (η) described the extent to which this combustion reaction reached completion, and was defined as the ratio of the mass of carbon produced by the reaction in the form of CO_2, $\dot{m}_{C,CO_2,produced}$, to the mass of carbon in the form of hydrocarbons in the fuel gas stream, $\dot{m}_{C,HC,FG}$,

$$\eta[\%] = \frac{\dot{m}_{\mathrm{C,CO_2,produced}}}{\dot{m}_{\mathrm{C,HC,FG}}} \times 100. \tag{2.5}$$

Since Eq. (2.5) is defined as a ratio of mass flow rates of atomic carbon, an equivalent ratio can be written in which the mass flow rates of CO_2 produced by combustion and carbon in the form of hydrocarbons in the fuel gas can be represented by their respective molar flow rates, $\dot{n}_{\mathrm{CO_2,produced}}$ and $x(X_{\mathrm{C}_x\mathrm{H}_y,\mathrm{FG}})\dot{n}_{\mathrm{FG}}$:

$$\eta[\%] = \frac{\dot{n}_{\mathrm{CO_2,produced}}}{x(X_{\mathrm{C}_x\mathrm{H}_y,\mathrm{FG}})\dot{n}_{\mathrm{FG}}} \times 100 \tag{2.6}$$

where x describes the overall carbon coefficient representative of the hydrocarbons in the fuel gas on a mole fraction basis (*i.e.*, x = 1 for a pure CH_4 fuel gas, x = 3 for a pure C_3H_8 fuel gas, and x = 2 for a 50% CH_4/50% C_3H_8 fuel gas mixture by volume) and $X_{\mathrm{C}_x\mathrm{H}_y,\mathrm{FG}}$ represents the mole fraction of the hydrocarbons in the fuel gas as a whole, considering there may be non-hydrocarbon species present such as in the case of natural gas. The numerator and denominator of Eq. (2.6) expanded in Eqs. (2.7) and (2.8), respectively, as:

$$\dot{n}_{\mathrm{CO_2,produced}} = X_{\mathrm{CO_2,plume}}\dot{n}_{\mathrm{plume}} - X_{\mathrm{CO_2},\infty}\dot{n}_{\infty} - X_{\mathrm{CO_2,FG}}\dot{n}_{\mathrm{FG}} \tag{2.7}$$

where the right-hand side of Eq. (2.7) represents the total molar flow rate of CO_2 in the burner exhaust plume minus the molar flow rate of CO_2 contributed by the ambient air (*i.e.*, based on 463 ppm of CO_2 in the lab) and the fuel gas (*i.e.*, natural gas supplied to the Engine Lab in the University of Alberta Mechanical Engineering department contains ~1% CO_2), and

$$\begin{aligned} x\left(X_{\mathrm{C}_x\mathrm{H}_y,\mathrm{FG}}\right)\dot{n}_{\mathrm{FG}} = {} & \textstyle\sum_k \#_{C,k}\left(X_{k,\mathrm{plume}} - X_{k,\infty}\frac{M_{\mathrm{plume}}}{M_{\infty}}\right)\dot{n}_{\mathrm{plume}} + \\ & \textstyle\sum_k \#_{C,k}\left(X_{k,\infty}\frac{M_{\mathrm{FG}}}{M_{\infty}}\dot{n}_{\mathrm{FG}}\right) - X_{\mathrm{CO_2,FG}}\dot{n}_{\mathrm{FG}} \end{aligned} \tag{2.8}$$

where $\#_{C,k}$ is the carbon coefficient for the carbon-based gas species, k, in the plume (*i.e.*, $\#_{C,\mathrm{CO_2}} = 1$ for CO_2, $\#_{C,\mathrm{CH_4}} = 1$ for CH_4, $\#_{C,\mathrm{C_3H_8}} = 3$ for C_3H_8, and $\#_{C,\mathrm{C}_m\mathrm{H}_n} = m$ for C_mH_n), M_{plume}, M_∞, and M_{FG} are the molecular weights of the plume, ambient air, and fuel gas, respectively. The terms on the right-hand side of Eq. (2.8) reflect those of Eq. (2.7) in that they represent the molar flow rates of the plume, ambient air, and fuel gas, except that they describe the fuel stream. The molar flow rate of the plume, $\dot{n}_{\mathrm{plume}}$, is defined as follows:

$$\dot{n}_{\mathrm{plume}} = \frac{\left[x\left(X_{\mathrm{C}_x\mathrm{H}_y,\mathrm{FG}}\right)\dot{n}_{\mathrm{FG}} + X_{\mathrm{CO_2},\mathrm{FG}}\dot{n}_{\mathrm{FG}} - \left(X_{\mathrm{CO_2},\infty} + X_{\mathrm{CO},\infty} + X_{\mathrm{CH_4},\infty} + \sum_k \#_{C,\mathrm{C}_m\mathrm{H}_n} X_{\mathrm{C}_m\mathrm{H}_n,\infty}\right)\frac{M_{\mathrm{FG}}}{M_\infty}\dot{n}_{\mathrm{FG}}\right]}{\left[X_{\mathrm{CO_2},\mathrm{plume}} - X_{\mathrm{CO_2},\infty} + \frac{f_{m,\mathrm{plume}} R_u T_{\mathrm{plume}}}{M_{\mathrm{C(s)}} P_{\mathrm{plume}}} + X_{\mathrm{CO},\mathrm{plume}} - X_{\mathrm{CO},\infty} + X_{\mathrm{CH_4},\mathrm{plume}} - X_{\mathrm{CH_4},\infty} + \sum_{m,n} \#_{C,\mathrm{C}_m\mathrm{H}_n}\left(X_{\mathrm{C}_m\mathrm{H}_n,\mathrm{plume}} - X_{\mathrm{C}_m\mathrm{H}_n,\infty}\right)\right]} \tag{2.9}$$

where $f_{m,\mathrm{plume}}$ is the mass concentration of soot in the plume, R_u is the universal gas constant (8.314 J/mol·K), T_{plume} is the plume temperature measured by an RTD probe (Omega, PR-31 Series), and P_{plume} is the static pressure in the duct measured by a pressure transducer (Omega, PX409-100AI). Due to the difference in the PAX cell and plume temperatures, the $f_{m,\mathrm{plume}}$ value was corrected based on the cell temperature, T_{cell}, and yielded the actual measured soot mass concentration, $f_{m,\mathrm{measured}}$, as follows:

$$f_{m,\mathrm{plume}} = f_{m,\mathrm{measured}} \frac{T_{\mathrm{cell}}}{T_{\mathrm{plume}}}. \tag{2.10}$$

As demonstrated in the derivation performed by Corbin and Johnson [51], Eq. (2.9) was used to calculate a value for $\dot{n}_{\mathrm{plume}}$ for each burner operating condition, which was then used to evaluate Eqs. (2.7) and (2.8) before finally using Eq. (2.6) to resolve the CCE. In addition, to determining the combustion efficiency of the burner at varying levels of steam-assist, the emission indices for various pollutant species was also of interest. The emission index (EI) of a species was calculated as the ratio

of the species' mass emission rate generated by combustion to the mass flow rate of fuel gas to the burner, as given by:

$$EI_j = \frac{\dot{m}_{j,\text{produced}}}{\dot{m}_{\text{FG}}} \tag{2.11}$$

where j represents the species or class of species in question: CO, CO_2, THC, NO_x, and BC. For the gas-phase pollutant species, the mass emission rate was expressed as follows:

$$\dot{m}_{j,\text{produced}} = M_j \left(\left(X_{j,\text{plume}} - X_{j,\infty}\right)\dot{n}_{\text{plume}} - \left\{ X_{j,\text{FG}} \frac{\dot{m}_{\text{FG}}}{M_{\text{FG}}} \right\}_{\text{inert}} + X_{j,\infty} \frac{\dot{m}_{\text{FG}}}{M_\infty} \right). \tag{2.12}$$

The mass emission rate for BC was defined as:

$$\dot{m}_{\text{C(s)},\text{produced}} = f_{m,\text{measured}} \frac{R_u T_{\text{cell}}}{P_{\text{plume}}} \dot{n}_{\text{plume}}. \tag{2.13}$$

The uncertainty in the carbon conversion efficiencies and emission indices were evaluated by performing propagation of uncertainties for all the measurable parameters, assuming that these quantities were independent of each other. The uncertainty in each parameter was derived based on the inherent bias error associated with the measuring instrument and the precision error due to the statistical variability in the experimental data. Refer to Appendix E for the derivations of uncertainties.

Chapter 3

3. Results and Discussion

3.1 Experimental Test Matrix

A range of parametric variations were performed in the experimental phase of the study, as shown in Table 3.1, for a total of seven unique experimental sets. The reference set of experiments was established as a 12.7 mm OD inner tube configured burner flaring 20 SLPM of CH_4 with an inner coflow of steam. Branching off from the reference set, each of the remaining six sets featured a single experimental design difference with the rest of the parameters being kept the same (*i.e.*, except for experimental set 7 where two parameters were altered from the reference set). This was done to investigate the extent to which each of the operating parameters—inner tube OD, fuel type, fuel flow rate, assist configuration, and assist fluid composition—affected CCE, EI_{THC}, EI_{CO_2}, EI_{CO}, EI_{NO_x}, and EI_{BC}. For each of the experimental sets outlined, the fuel gas flow rate remained constant while an increasing amount of assist fluid was introduced to the flame starting from a null quantity (*i.e.*, zero steam mass flow rate) until the necessary flow rate required to either extinguish the flame or reduce the flame CCE to <10%. For experimental sets 1 – 5 and 7, EI_{THC} was represented as EI_{CH_4} since CH_4 was the only detected unburned hydrocarbon during the collapse of CCE.

Table 3.1: Lab-scale steam-assisted flaring experimental test matrix.

Experimental Set	Inner Tube OD (mm)	Fuel	Fuel Flow Rate (SLPM)	Assist Configuration	Assist Composition
1	12.7	CH_4	20	Inner	100% Steam
2	12.7	CH_4	**40**	Inner	100% Steam
3	**6.35**	CH_4	20	Inner	100% Steam
4	12.7	CH_4	20	Inner	**58% N_2/42% He**
5	12.7	CH_4	20	Inner	**50% Steam/29% N_2/21% He**
6	12.7	**C_3H_8**	20	Inner	100% Steam
7	12.7	CH_4	**40**	**Outer**	100% Steam

3.2 Steady State Burner Temperatures and Exit Plane Conditions

One of the fundamental measurements required for developing an understanding of the fuel and assist fluid hydrodynamic exit conditions, and by extension their effect on the combustion process, were the temperatures at the burner exit. Based on the thermocouple arrangement shown in Figure 2.1, temperature measurements were taken up to 40 mm below the burner exit plane in the annular space and at the center of the inner tube exit plane. The range of temperatures measured corresponding to the range of assist flow rates tested is presented in Table 3.2.

Table 3.2: Range of temperature measurements taken at various z values in the annular and center space of the burner.

Experiment	Temperature Ranges (°C)					
	Annular					Center
	z = 0 mm	z = -5 mm	z = -10 mm	z = -20 mm	z = -40 mm	z = 0 mm
1	132.5 − 148.1	117.3 − 132.5	93.0 − 109.2	70.2 − 85.6	47.6 − 62.0	97.4 − 126.2
2	99.8 − 127.0	86.9 − 114.1	65.7 − 95.4	47.7 − 78.1	31.0 − 61.7	97.5 − 128.3
3	100.2 − 144.0	84.3 − 124.6	66.0 − 99.1	51.3 − 77.4	32.4 − 48.5	98.4 − 100.5
4	126.9 − 136.6	114.2 − 123.7	89.9 − 102.5	66.4 − 80.7	43.6 − 59.4	40.9 − 113.7
5	132.5 − 139.6	119.0 − 125.6	95.9 − 105.1	73.2 − 83.8	51.5 − 62.6	112.4 − 126.0
6	120.6 − 131.6	104.8 − 115.7	85.0 − 96.0	65.6 − 77.9	48.4 − 59.7	97.7 − 128.3
7	97.6 − 98.1	97.3 − 97.9	97.3 − 97.7	97.4 − 97.6	97.7 − 99.7	29.1 − 67.6

For the inner steam coflow cases (*i.e.*, experimental sets 1 – 6), the trend in the fuel and steam temperatures generally followed a similar pattern. This pattern is presented in Figure 3.1a by example of experimental set 1. As can be seen by the fuel temperature plots in Figure 3.1a, the closer to the tip of the burner the fuel reached as

it flowed through the annular space, the higher its temperature increased. This was due to the proximity of the burner tip to the flame and the heat transfer it received by convection and radiation. It was also observed that for the fuel temperature plots in which steam-assist was active (*i.e.*, 1.3 < MFR < 4.3) the temperatures of the fuel at each of the thermocouple positions were similar and only deviated from each other by up to 5 °C. Of particular interest was the lower temperature of the fuel at a zero steam-to-fuel gas MFR compared to the non-zero steam-to-fuel gas MFRs, which averaged approximately 13 °C lower. This was a result of the convective heat transfer of steam flowing through the inner tube to the fuel in the annular space when steam-assist was active. As a result of the heat loss experienced by steam to the fuel gas and despite the use of heated hosing to maintain the steam at a superheated state upstream of the burner, steam at lower flow rates would typically be at or slightly above the saturated steam temperature upon reaching the burner exit. This is evident from Figure 3.1a inset in which the temperature of steam at 1.3 < MFR < 3.3 hovered around 97.5 °C before abruptly increasing to 117 °C at an MFR of 3.6. For the highest steam mass flow rates, a degree of superheat (*i.e.*, the difference in the steam superheated and saturation temperatures at a given pressure) of ~30 °C was achieved at the burner exit.

Figure 3.1b represents the fuel and steam temperatures for experimental set 7 in which the assist configuration was reversed and steam was the outer coflow. In contrast to Figure 3.1a, the steam temperature remained relatively unchanged as it progressed towards the exit of the burner. Despite the increase in steam-to-fuel gas MFR, the steam did not experience a sudden rise in temperature as it had in experimental set 1 as a result of steam undergoing convective heat losses to both the ambient air outside the outer tube wall and to the fuel flowing through the inner tube. This is confirmed by the fuel temperature profile in Figure 3.1b inset which shows a sudden increase in the fuel temperature as soon as steam-assist becomes active at an MFR of 0.52.

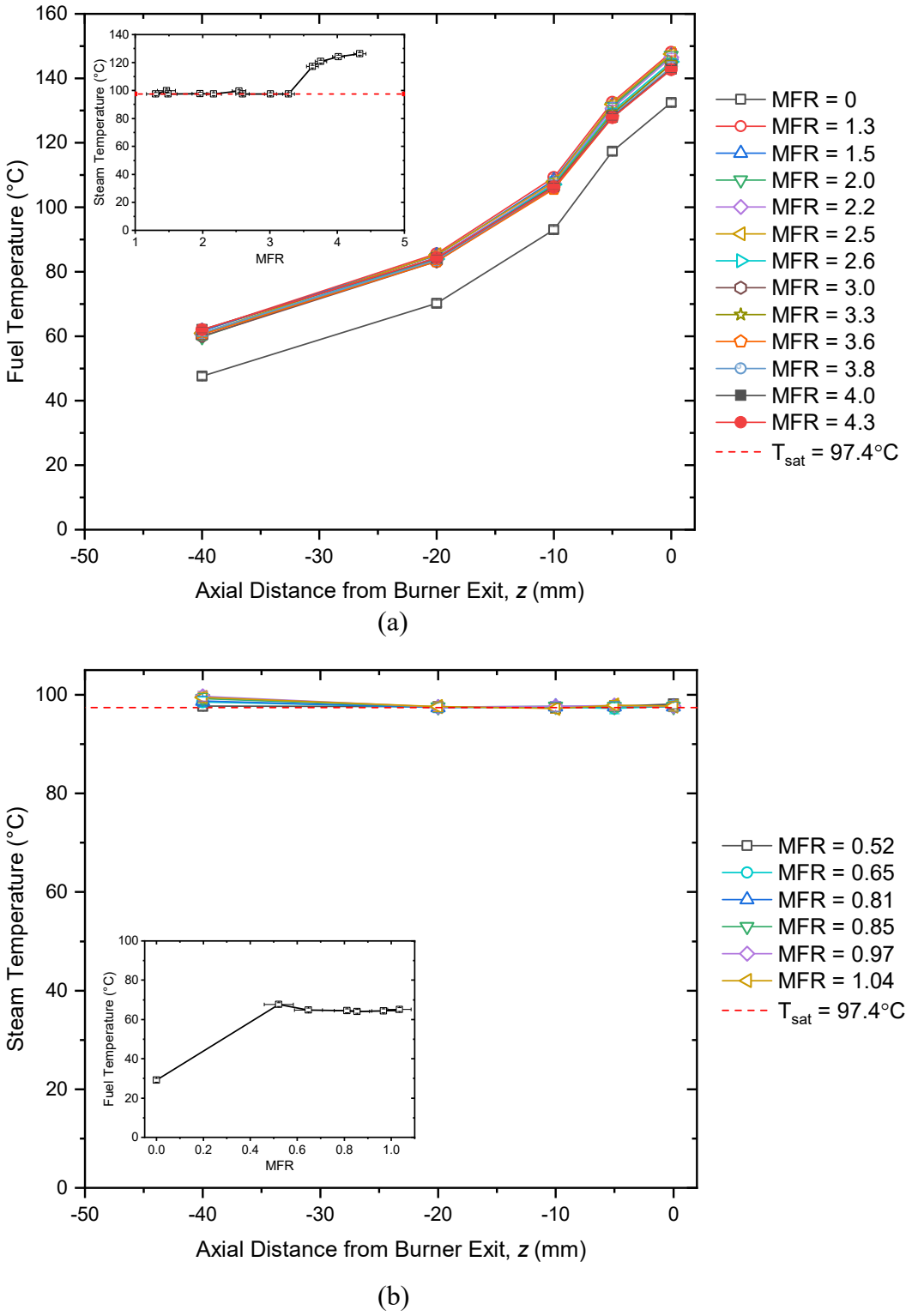

Figure 3.1: Temperature measurements of fuel and steam taken at thermocouple positions located up to 40 mm below the exit plane in the annular space and in the center of the inner tube exit plane for experimental sets (a) 1 and (b) 7. Steam saturation temperatures at local pressure are shown in red dashed lines.

Based on the temperature measurements taken at the burner exit plane (*i.e.*, $z = 0$ mm for annular and center streams), the velocities of fuel and steam at this location were determined. When the exit plane thermocouple yielded the saturation temperature for steam, the steam was always assumed to be at a saturated vapor state with 100% quality even though the steam lost heat as it travelled through the uninsulated burner. This assumption was found to be reasonable after evaluating the total convective and radiative heat losses experienced by the steam. For inner steam coflow, the steam underwent heat loss at a rate of 35 W and had a minimum quality of 94%. Conversely, the outer steam coflow sustained a heat loss rate of 65 W and had a minimum quality of 87%. The density of the steam at the saturated vapour state was therefore obtained by referring to the steam tables [52] at the burner exit temperature and ambient pressure condition. The steam bulk flow velocity at the exit plane was then calculated by dividing the mass flow rate by the density to yield volumetric flow rate, which was in turn divided by the cross-sectional flow area of the steam. The same procedure was followed for evaluating the fuel and N_2/He gas mixture exit velocities except that the density was determined at the exit conditions using the ideal gas law.

To combine the effects of mass and exit velocity of the fuel and assist fluids, the vertical momentum (kg·m/s^2) of these streams aligned to the z-direction at the burner exit plane was considered based on the following definition:

$$P_{zz} = \dot{m}_z v_z \tag{3.1}$$

where $\dot{m}_z$ (kg/s) is the mass flow rate of the fuel or assist fluid stream and v_z (m/s) is the bulk flow exit velocity of the respective stream in the z-direction. Note that the actual rate of vertical momentum leaving a circular tube is defined by

$$P_{zz} = \int_{r_i}^{r_o} 2\pi r \rho v_z^2 \, dr \tag{3.2}$$

where r is the radius and the subscripts i and o represent the inner and outer limits for the integration. Since the integral cannot be evaluated due to the radial dependency of density and velocity being unknown, Equation (3.1) is used instead.

The exit velocities of the fuel and assist streams were also used to evaluate the Reynolds number at the exit plane of the burner, which is defined as follows:

$$Re = \frac{\rho v_z d_h}{\mu} \tag{3.3}$$

where ρ is the density, d_h (m) is the hydraulic diameter, and μ (Pa·s) is the dynamic viscosity all evaluated at the exit plane temperatures of the various fluids and lab room pressure. The range of steam-to-fuel gas MFRs tested for experimental sets 1 − 7 is presented in Table 3.3 with the corresponding range in the steam exit velocities, momentum, and Reynolds number. The average velocity, momentum, and Reynolds number of the fuel at the exit plane are also shown for each experimental set.

Table 3.3: Steam-to-fuel gas MFRs with corresponding exit velocities, momentums, and Reynolds number for fuel and steam. Calculated range in parameters for steam assist correspond to the range in the minimum to maximum steam flow rates, excluding the unassisted case.

Experimental Set	Steam-to-Fuel Gas MFR	Exit Velocity (m/s)		Exit Momentum × 10^{-4} (N)		Exit Reynolds	
		Fuel	Steam	Fuel	Steam	Fuel	Steam
1	1.3 − 4.3	1.8	5.4 − 19.1	3.9	15.3 − 181.2	533	2 709 − 8 251
2	0.6 − 3.7	3.3	4.8 − 31.9	14.7	12.2 − 514.8	1 113	2 425 − 1 3924
3	1.1 − 2.5	1.3	19.2 − 44.9	2.7	45.0 − 246.5	679	4 799 − 11 232
4	0.2 − 5.3	1.7	0.5 − 22.8	3.8	0.2 − 266.2	545	195 − 5 815
5	2.3 − 4.3	1.8	9.7 − 19.0	3.9	48.0 − 178.2	539	3 392 − 6 201
6	0.4 − 2.7	1.7	4.8 − 33.1	10.4	12.4 − 546.6	2 000	2 446 − 14 292
7	0.5 − 1.0	8.3	1.5 − 2.9	36.5	3.3 − 13.1	4 144	671 − 1 333

The burner exit temperature conditions for the fuel and assist fluids were also used to deduce the adiabatic flame temperatures for each experimental set. At each of the experimental operating points, the equilibrium temperature, T_{eq} (K) of the reactants and assist fluid mixture was first calculated as follows:

$$T_{eq} = \frac{\sum_k \dot{m}_k c_{p,k} T_k}{\sum_k \dot{m}_k c_{p,k}} \tag{3.4}$$

where $\dot{m}_k$ represents the mass flow rate of each component, k, of the pre-combustion non-reacting mixture including the fuel gas, assist fluids, and combustion air proportional to the CCE, $c_{p,k}$ (J/kg·K) is the isobaric specific heat capacity of component k, and T_k (K) is the initial temperature of component k. Using STANJAN [53], a chemical equilibrium solver, the molar flow rate of each species in the reactant stream, an initial temperature of T_{eq}, and the ambient pressure were implemented as starting parameters. The list of species at equilibrium for experimental set 1 were: CH_4, O_2, N_2, H_2O, CO_2, CO, NO_2, NO, H_2, OH, H, N, and O. Experimental sets 4 and 5 also included He while experimental set 6 listed C_2H_6 and C_3H_8 as well. The adiabatic flame temperature was then calculated under constant temperature and pressure as shown in Figure 3.2. More details on the calculation of adiabatic flame temperature are provided in Appendix F.

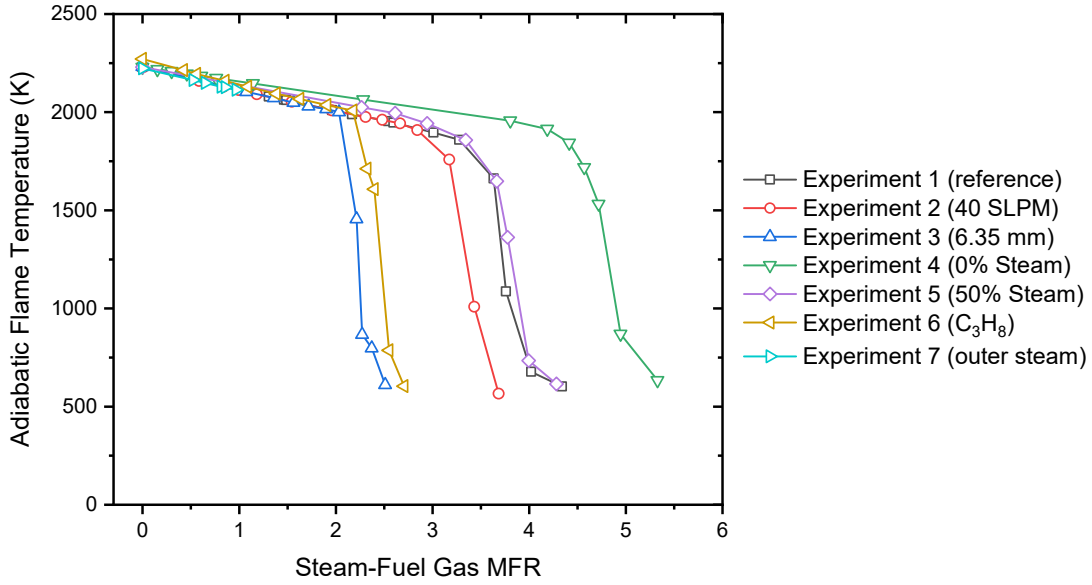

Figure 3.2: Adiabatic flame temperatures for experimental sets 1 – 7.

3.3 Experimental Set 1: Reference Set with 20 SLPM CH_4 Flame and Inner Steam Coflow through 12.7 mm OD Inner Tube

Beginning with zero inner steam coflow, increasing mass flow rates of steam were injected into the base of a 20 SLPM CH_4 coannular jet diffusion flame. The corresponding CCE and EIs are shown in Figure 3.3. In addition to the EIs for CH_4, CO_2, CO, NO_x, and BC, a comprehensive CO_2 equivalent EI (*i.e.*, $EI_{CO_2,eq}$) was calculated based on a 100-year time horizon. This was done by taking the total sum of the products of the individual EIs and their respective 100-year GWP values, which are shown in Table 3.4.

Table 3.4: 100-year GWP values for various pollutant species and their respective uncertainties obtained from the IPCC [6,54].

Species	100-year GWP	Uncertainty (+/−)
CH_4	28	8.4
C_2H_6	5.5	5.5
C_3H_8	3.3	3.3
CO	1.8	0.6
NO_x	−8.2	10.3
BC	900	800

At zero inner steam coflow, the CCE was found to be essentially 100%. This operating point coincided with the maximum NO_x and BC production for this experimental set of 1.21 g NO_x/kg fuel and 0.076 g BC/kg fuel, respectively. With the initial input of steam into the flame at a steam-to-fuel gas MFR of 1.3, there was a sudden decrease in EI_{NO_x} and EI_{BC} by nearly a factor of 3 and an order of magnitude, respectively. Since NO_x emissions for these experimental sets were assumed to be entirely a result of thermal NO_x formation, which is a highly temperature-dependent mechanism involving the dissociation and reaction of N_2 and O_2, the drop in EI_{NO_x} was attributed to the cooling effect of steam on the flame. This effect was established by various studies [55,56] which demonstrated reduced flame temperature with added steam. The decrease in flame temperature was further substantiated by the adiabatic flame temperature plots shown in Figure 3.2, which demonstrated a reduction in the

product gas temperature with increasing steam injection mass flow rates for all experimental sets.

The decrease in EI_{BC} was attributed to the improved mixing of the fuel stream with combustion air as a result of the internal jet of steam. In order to elaborate on this claim, a schematic of the flow structure outside the exit plane of the burner is presented in Figure 3.4, which is based on findings in the literature for non-reacting co-axial jets by Dahm *et al*. [57] and Rehab *et al*. [58]. According to Rehab *et al*., coaxial jets issuing from the central and annular ports of a nozzle were characterized by a "potential core," which was a region where the fluid velocity and concentration remained relatively unchanged due to minimal viscous shear and diffusion effects. The heights of the inner and outer potential cores, $h_{pc,i}$ and $h_{pc,o}$, respectively, were found to be related to the ratio of the inner to outer jet exit velocities, v_i and v_o, respectively. The region between the inner and outer potential cores was defined as the inner shear layer in which the inner and outer coflow jets mixed. Likewise, the region between the outer potential cores and the jet edge was defined as the outer shear layer in which mixing occurred between the outer jet and ambient fluid. The jet edge defined the boundary at which the velocity approached zero. Based on the experiments performed by Dahm *et al*. [57], the nature of the mixing within the shear layers was found to be highly dependent on the inner to outer jet exit velocity ratio. Generally, when the inner jet exit velocity exceeded the outer jet exit velocity, the instabilities generated in the inner shear layer were insubstantial and did not yield any significant vortical structures, possibly due to the robustness of the inner potential core. In fact, the deformation of the inner shear layer was dominated by the "roll-up" vortices generated in the outer shear layer which entrained large amounts of the ambient fluid that penetrated deep into the inner potential core. This scenario yielded optimal mixing in the outer shear layer. When the outer jet exit velocity exceeded the inner jet exit velocity, however, the instabilities in the inner mixing layer became more pronounced leading to the formation of vortices within this layer. As a result, the inner mixing layer experienced a significant growth which greatly shortened the height of the inner potential core and ensured a high degree of mixing between the inner and outer jets. In relation to the present experimental set, the high velocity gradient

between the steam and fuel exit velocities of 5.4 m/s and 1.8 m/s, respectively, as listed in Table 3.3 suggests efficient mixing within the outer shear layer, and thus reduced BC emissions.

In addition to the physical interaction of steam with the fuel, steam is believed to promote complete combustion through various chemical mechanisms [59]. Based on a study performed by Müller-Dethlefs and Schlader [60], steam was found to inhibit BC and CO formation when added to premixed propane and ethylene flames. They suggested that the presence of steam led to an increase in the concentration of OH radicals in the flame, thereby promoting the oxidation of BC through the reaction of C + OH ⟶ CO + H and CO through the reaction CO + OH ⟶ CO_2 + H. From an operational standpoint, the decrease in EI_{BC} was made apparent by the dimming of the originally bright and luminous unassisted flame as shown by the photographs taken at increasing steam-to-fuel gas MFRs in Figure 3.5. As the steam-to-fuel gas MFR was increased to 3.0 with a resulting CCE of 97%, the EI_{NO_x} and EI_{BC} dropped further by an order of magnitude. In addition, the EI_{CO_2} experienced a reduction from the nominal value of 2.7 kg CO_2/kg fuel while the first measured quantity of EI_{CH_4} equal to 29.76 g CH_4/kg fuel was detected, indicating the onset of fuel being stripped away from the combustion zone. This was reminiscent of the industrial problem of over-assisting in which excessive amounts of steam led to the occurrence of fugitive hydrocarbon emissions. The flame at this point also became nearly imperceptible, as can be observed in Figure 3.5. By again increasing the steam-to-fuel gas MFR, the incomplete combustion of CH_4 became evident from the detection of CO, with a maximum EI_{CO} of 85.57 g CO/kg fuel produced at a steam-to-fuel gas MFR of 3.8 and CCE of 44%. A photograph corresponding to this operating point is shown in Figure 3.5. The steam-to-fuel gas MFR was raised to its final value of 4.3 at which point the CCE was diminished to 8% and the EI_{CH_4} peaked at 923.4 g CH_4/kg fuel. This operating condition resulted in a short coannular jet flame as shown in Figure 3.5. The $EI_{CO_2,eq}$ value remained relatively constant until the drop in CCE below 96.5% at which point it rose quickly to a maximum of 26.1 kg CO_2/kg fuel due to the CH_4 being mostly vented at this point and thus showing a positive correlation between over-assisted flaring and the rise in the greenhouse gas effect. The magnitude of the

error bars was mostly due to the large uncertainty in the CH_4 100-yr GWP (*i.e.*, 28 ± 8.4).

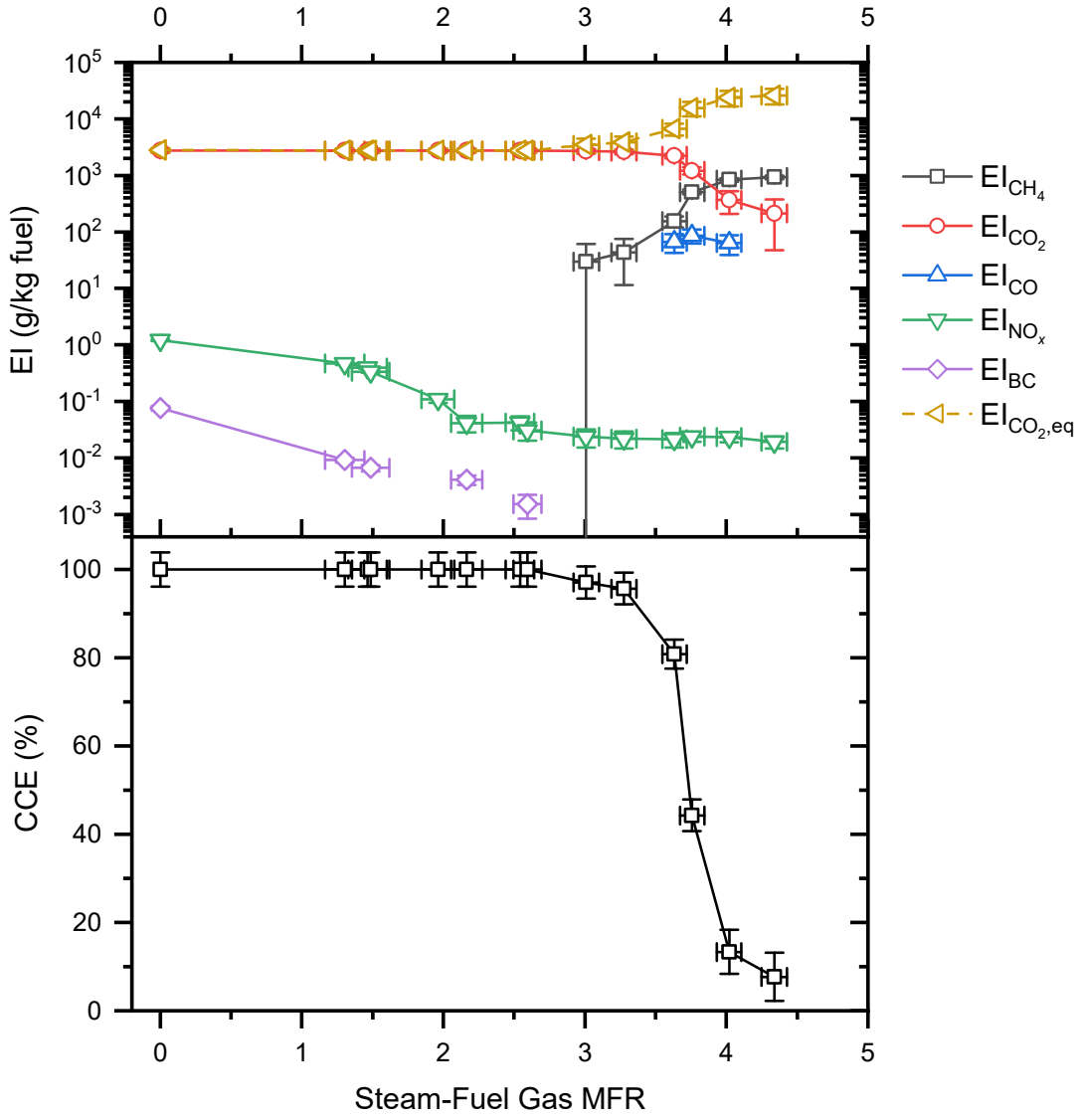

Figure 3.3: Experimental set 1 CCE plot (bottom) and EI plot (top).

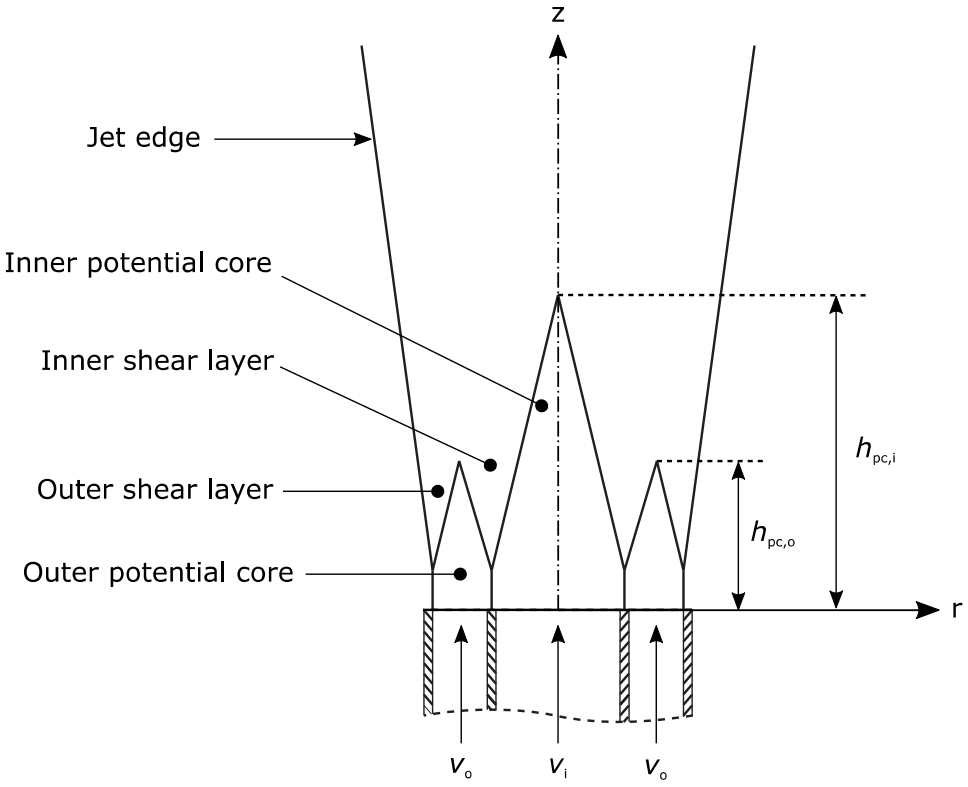

Figure 3.4: Near-field flow structure of inner and annular jets issuing from a nozzle with exit velocities of v_i and v_o, respectively. The heights of the inner and outer potential cores are labeled as $h_{pc,i}$ and $h_{pc,o}$, respectively.

Figure 3.5: Photos of experimental set 1 flame taken at increasing steam-to-fuel gas MFRs.

3.4 Experimental Set 2: Doubling the Fuel Flow Rate

Using the same burner geometry and flow configuration as described for experimental set 1, the flow of CH_4 was doubled from 20 to 40 SLPM. One of the reasons for attempting a higher fuel flow rate was to better scale the test results by lessening the gap between the unassisted experimental test point and the first assisted point in terms of the steam-to-fuel gas MFR that was caused by the limited lower bound of the calibrated steam range (*i.e.*, 14 g/min). As a result, the trends in EI_{NO_x} and EI_{BC} would be better resolved in this region. As can be seen in Figure 3.6, the EI_{NO_x} trend was found to behave similarly to that of the 20 SLPM CH_4 experimental set in that it dropped gradually by two orders of magnitude as an increasing amount of steam was injected into the flame, starting from a maximum value of 0.88 g NO_x/kg fuel. In regards to EI_{BC}, a maximum value of 0.017 g BC/kg fuel was generated for the unassisted point, which was less than the previous scenario as a result of the near doubling of the fuel exit velocity from the 1.8 m/s of the reference case to 3.3 m/s, as shown in Table 3.3. This could have potentially increased the instabilities in and consequent growth of the outer shear layer leading to improved fuel-air mixing. Beyond this test point, the EI_{BC} dropped with added steam and fluctuated between a zero value and trace measurements of $\leq$ 0.005 g BC/kg fuel. As with experimental set 1, the initial decline in CCE coincided with the stripping of CH_4 away from the combustion zone and occurred at a steam-to-fuel gas MFR of 2.5. Compared to the reference experimental set, however, doubling the fuel flow rate led to a slightly earlier onset of the CCE collapse at 96.5% with a steam-to-fuel gas MFR of 2.8. Furthermore, incomplete combustion of CH_4 seemed less pronounced in experimental set 2 than experimental set 1, which could potentially be due to the higher exit Reynolds for the fuel and steam as shown in Table 3.3, despite the similarity in the steam-to-fuel gas MFR and exit velocity ratio at a CCE of 96.5%. According to Rehab *et al*., [58] to compare two coaxial jets having the same inner to outer jet exit velocity ratios, the inner and outer jet exit Reynolds needs to be assessed. For the coaxial jet having a greater inner and outer jet exit Reynolds, the outer mixing layer develops earlier, which leads to better mixing between the coannular jet and the ambient fluid. At a steam-to-fuel gas MFR of 3.4, a maximum EI_{CO} of only 62.1 g CO/kg fuel was

produced. A final steam-to-fuel gas MFR test point of 3.7 yielded a CCE of 5% and a corresponding maximum EI_{CH_4} of 929 g CH_4/kg fuel. The change in physical appearance of the flame at increasing steam-to-fuel gas MFRs was similar for the 40 SLPM of CH_4 as for 20 SLPM of CH_4. As can be seen in Figure 3.6, the maximum $EI_{CO_2,eq}$ of 26.2 kg CO_2/kg fuel was nearly identical to that of the reference experimental set due to the high degree of CH_4 venting.

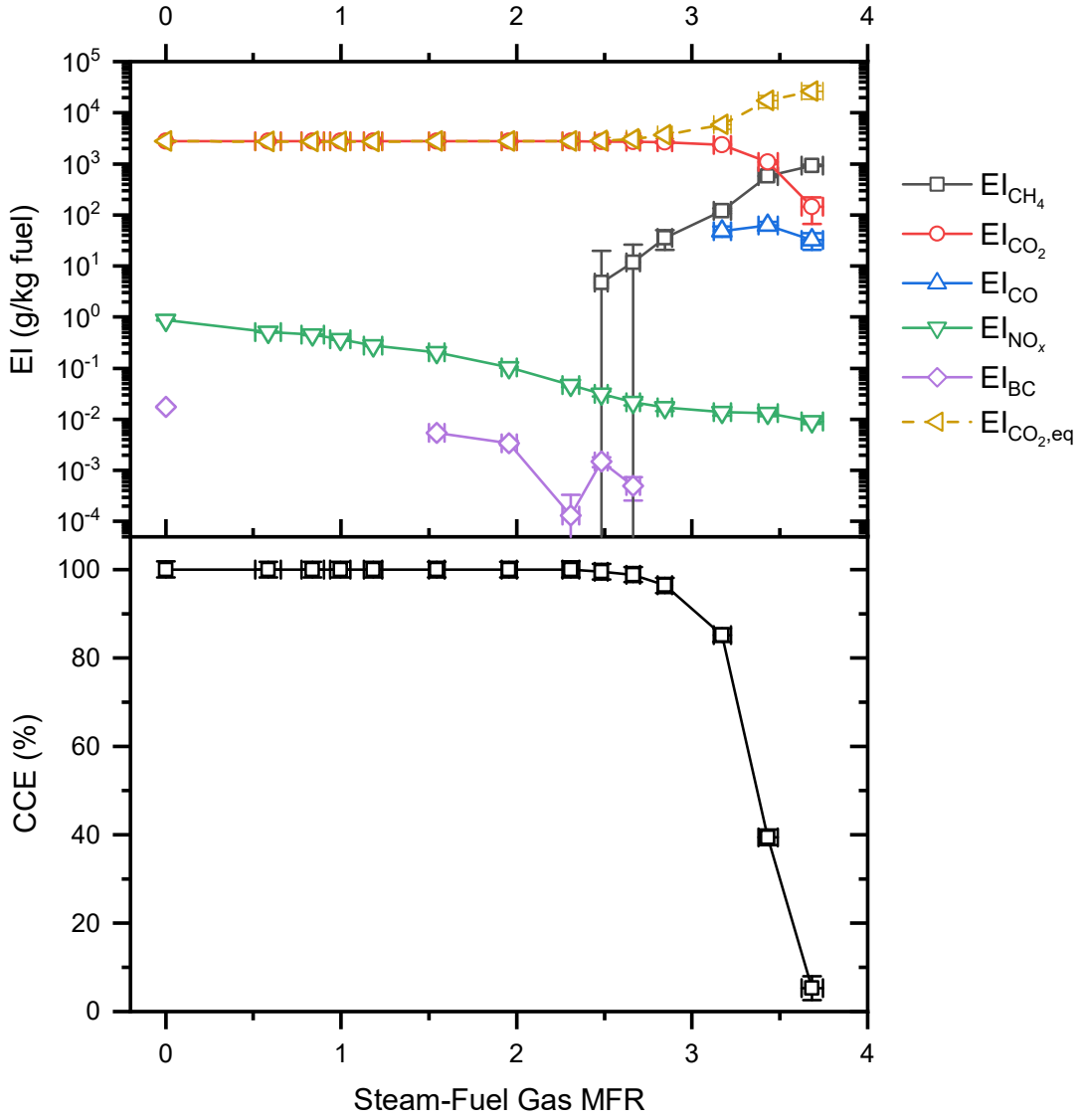

Figure 3.6: Experimental set 2 CCE plot (bottom) and EI plot (top).

3.5 Experimental Set 3: Reducing Burner Inner Tube Diameter by Half

The inner steam coflow configuration and standard CH_4 flow rate of 20 SLPM of the reference experimental set was retained for experimental set 3, with the only difference being that the original 12.7 mm OD inner tube was substituted with one having a 6.35 mm OD. The motivation behind this variation was to investigate the increase in the steam exit velocity relative to that of the fuel gas. As a result of increasing the annular cross-sectional flow area, the fuel had a considerably smaller exit velocity of 1.3 m/s compared to the reference set's 1.8 m/s, as shown in Table 3.3. This reduction in fuel exit velocity led to a decrease in the fuel-air mixing for the unassisted flame as demonstrated by the doubling of the EI_{BC} value to 0.161 g BC/kg fuel as shown in Figure 3.7, which was potentially due to the weaker instabilities and growth of the outer shear layer. The initial injection of steam at a steam-to-fuel gas MFR of 1.1 dropped the EI_{BC} by an order of magnitude and coincided with the maximum EI_{NO_x} value of 1.15 g NO_x/kg fuel. All additional increases to the steam-to-fuel gas MFR yielded null values of EI_{BC}. The EI_{NO_x} trend behaved similarly to those of the previous experimental sets, in that it underwent a reduction by nearly two orders of magnitude over the range of steam-to-fuel gas MFR. Unlike the two previous experimental sets, however, the onset of the CCE collapse phase at 96.5% for the present experimental set occurred considerably earlier at a steam-to-fuel gas MFR of 2.0. Also contrary to the previous experimental sets was the lack of CO production during the CCE collapse phase. This can be explained by referring to Table 3.3 which shows that for the present experimental set, the average fuel gas exit velocity was the lowest of all experimental sets at 1.3 m/s, whereas the range in the steam exit velocities was the highest at 19.2 – 44.9 m/s. In fact, at a CCE of 96.5%, experimental set 3 had the highest steam-to-fuel exit velocity ratio of 30.1 for all experimental sets of which the reference set only had an exit velocity ratio of 7.1. As described in section 3.3, higher inner to outer jet exit velocities are correlated with a more robust inner potential core which yield minimal inner shear layer development in favour of greater development of the outer shear layer. Such a high velocity gradient between the steam and fuel flows may therefore have helped entrain

sufficient oxygen to eliminate incomplete combustion. Furthermore, the rate at which the CCE dropped from 96.5% to <10% occurred more rapidly compared to the previous experimental sets—over a range in steam-to-fuel gas MFR of only 0.5 (*i.e.*, 2.0 – 2.5). The limiting factor to the continued injection of steam for the present experimental set may have been a result of a disruption to the combustion process due to excessive turbulence in the outer shear layer. As with experimental set 2, the progression in the change in the flame's appearance with increasing steam-to-fuel gas MFR was similar to that of experimental set 1. The maximum $EI_{CO_2,eq}$ of 26.5 kg CO_2/kg fuel was also similar to the reference experimental set as expected.

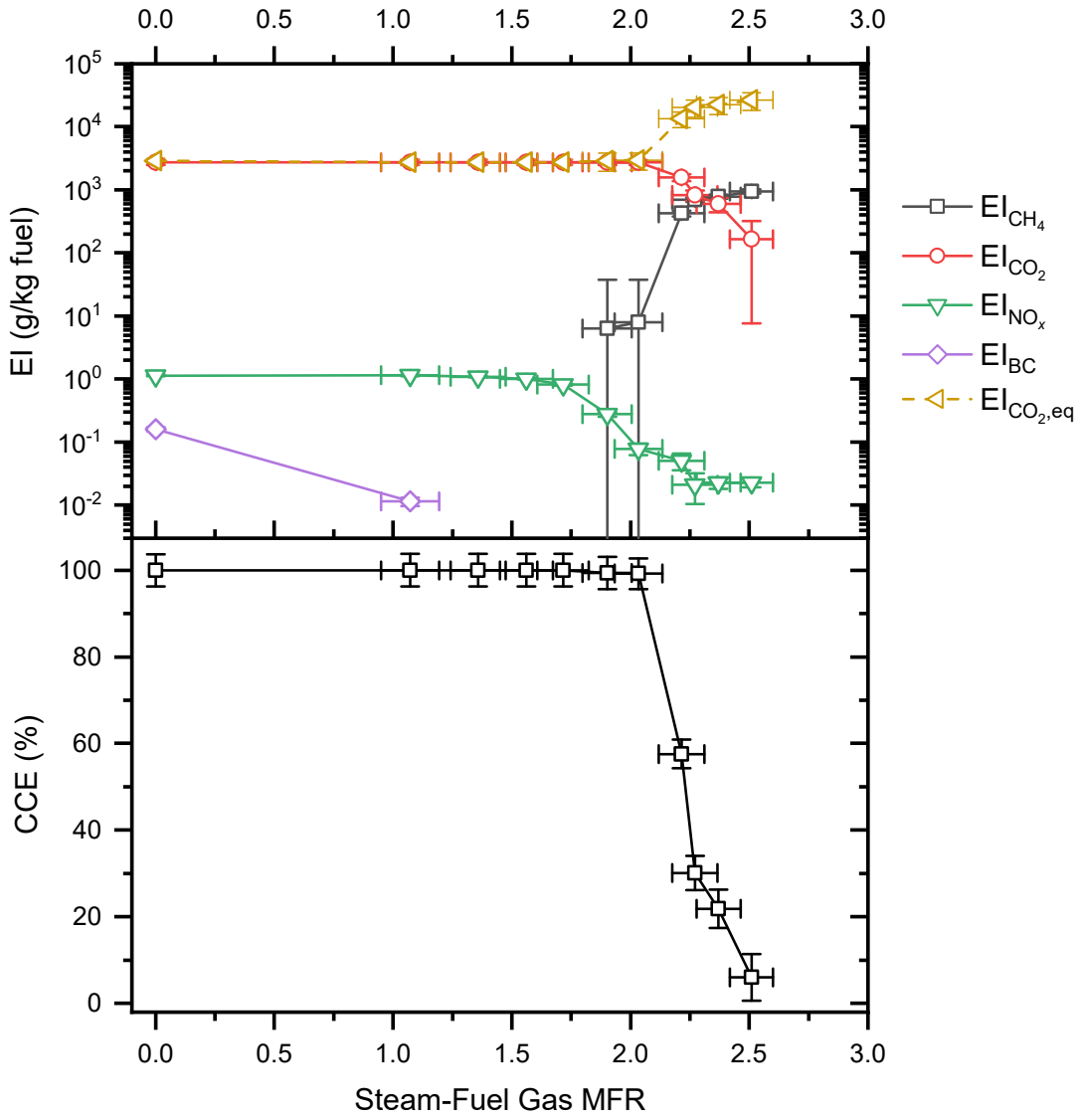

Figure 3.7: Experimental set 3 CCE plot (bottom) and EI plot (top).

3.6 Experimental Set 4: Steam-Equivalent Gas Mixture with 58% N_2 and 42% He

As discussed in the previous chapter, one of the goals of the study was to analyze the extent to which steam has a unique effect on promoting complete combustion through the water-gas shift reaction. The aim of this experiment was to replace the inner steam coflow with an alternative inert gas mixture having the same molecular weight as water and heated to the same temperature range as the steam in experimental set 1. A gas mixture of 58% N_2 and 42% He was chosen for this purpose. One of the major

advantages of working with the gas mixture was being able to dispense finer and more precise quantities to the burner as compared to the steam production and distribution system, which allowed for a higher resolution of the plots in Figure 3.8 at lower assist flow rates. At an equivalent steam-to-fuel gas MFR of 0.5, the EI_{BC} dropped from an initial value of 0.115 g BC/kg fuel by nearly an order of magnitude. BC was only detected once more at an equivalent steam-to-fuel gas MFR of 3.8, at which point it had dropped by another order of magnitude. With regards to the generation of NO_x, it did not initially decrease at the same rate as with experimental set 1 when the equivalent steam-to-fuel gas MFR was increased. The primary difference between the present experimental set and the reference experimental set was that the onset in the collapse of CCE starting at 96.5% did not occur until a considerably greater equivalent steam-to-fuel gas MFR of 4.1. In addition to this, the equivalent steam-to-fuel exit velocity at a CCE of 96.5% for the present experimental set reached 9.9 compared to 7.1 for the reference set. A possible explanation for the flame being able to sustain faster flows of the gas mixture is that the exit Reynolds number of the gas mixture, as presented in Table 3.3, only reached a maximum of 5 815 compared to 8 251 for the inner steam coflow in the reference set. Thus, the reduced turbulence of the inner coflow may have delayed the onset of fuel stripping from the combustion zone. The discrepancy in the Reynolds number was due to the significant variation in exit viscosities for steam and the gas mixture, with each having an average exit viscosity of 1.25×10^{-5} Pa·s and 2.03×10^{-5} Pa·s, respectively. During the collapse phase of the CCE, a maximum EI_{CO} of 78.7 g CO/kg fuel was generated, which was slightly less than that of the reference experimental set.

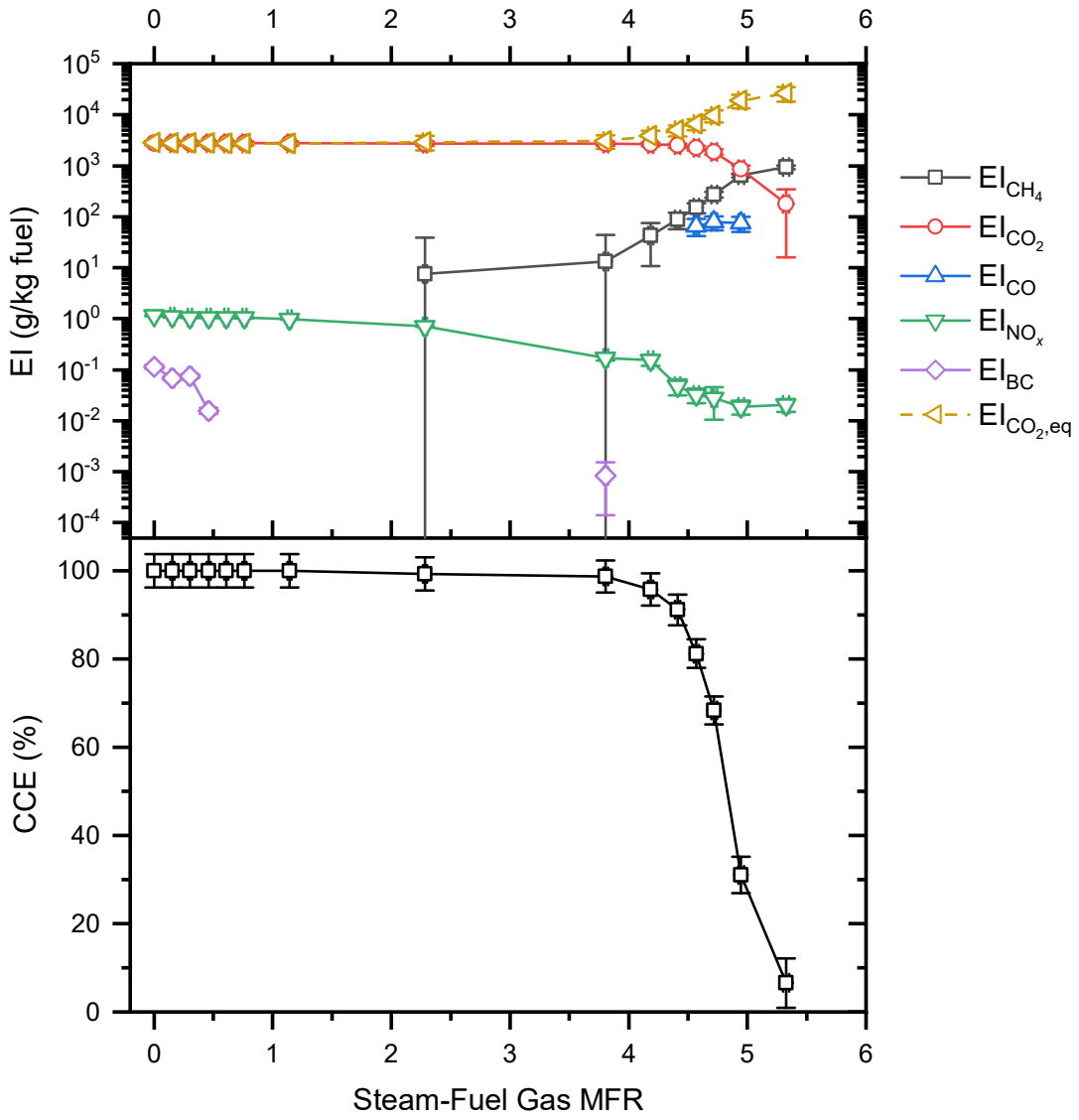

Figure 3.8: Experimental set 4 CCE plot (bottom) and EI plot (top).

3.7 Experimental Set 5: Steam-Equivalent Gas Mixture with 50% Steam, 29% N_2, and 21% He

To further investigate the impact of steam on combustion emissions, another internal coflow containing 50% steam, 29% N_2, and 21% He was tested. The purpose of this experiment was to examine whether a partial substitution of steam with the inert gas mixture would yield results proportional to the quantity of steam. A significant drawback encountered during the performance of this experimental set was the limitation in terms of the minimum possible assist flow rate. Since the calibrated

steam mass flow rate had a lower bound of 14 g/min and steam constituted 50% of the total flow, the overall minimum possible assist flow rate for this set was 28 g/min. As can be seen in Figure 3.9, after the unassisted test point in which an EI_{BC} of 0.09 g BC/kg fuel was generated, the initial steam-gas mixture injection occurred at an equivalent steam-to-fuel gas MFR of 2.3 (*i.e.*, equivalent to a mass flow rate of 30 g/min) at which point BC was no longer detected. This unfortunately obscured the EI_{BC} trend for this experimental set. As for EI_{NO_x} , the maximum value of 1.1 g NO_x/kg fuel experienced a drop by an order of magnitude at an equivalent steam-to-fuel gas MFR of 2.3. The rate at which NO_x production declined over the range of equivalent steam-to-fuel gas MFRs was in between that of the pure steam and N_2/He mixture internal coflow cases. By an equivalent steam-to-fuel gas MFR of 2.8, the CCE had been reduced to 96.5%, which was slightly earlier than for experimental set 1. The stripping of CH_4 away from the combustion zone also occurred at nearly the same time as the reference experimental set at an MFR of 2.9. A maximum EI_{CO} of 81.9 g CO/kg fuel was produced at an equivalent steam-to-fuel gas MFR of 3.8, which was in between the amount of CO generated for experimental sets 1 and 4. Overall, the results of the present experimental set were highly comparable to those of the reference set due to the nearly identical fuel and steam exit velocities as shown in Table 3.3.

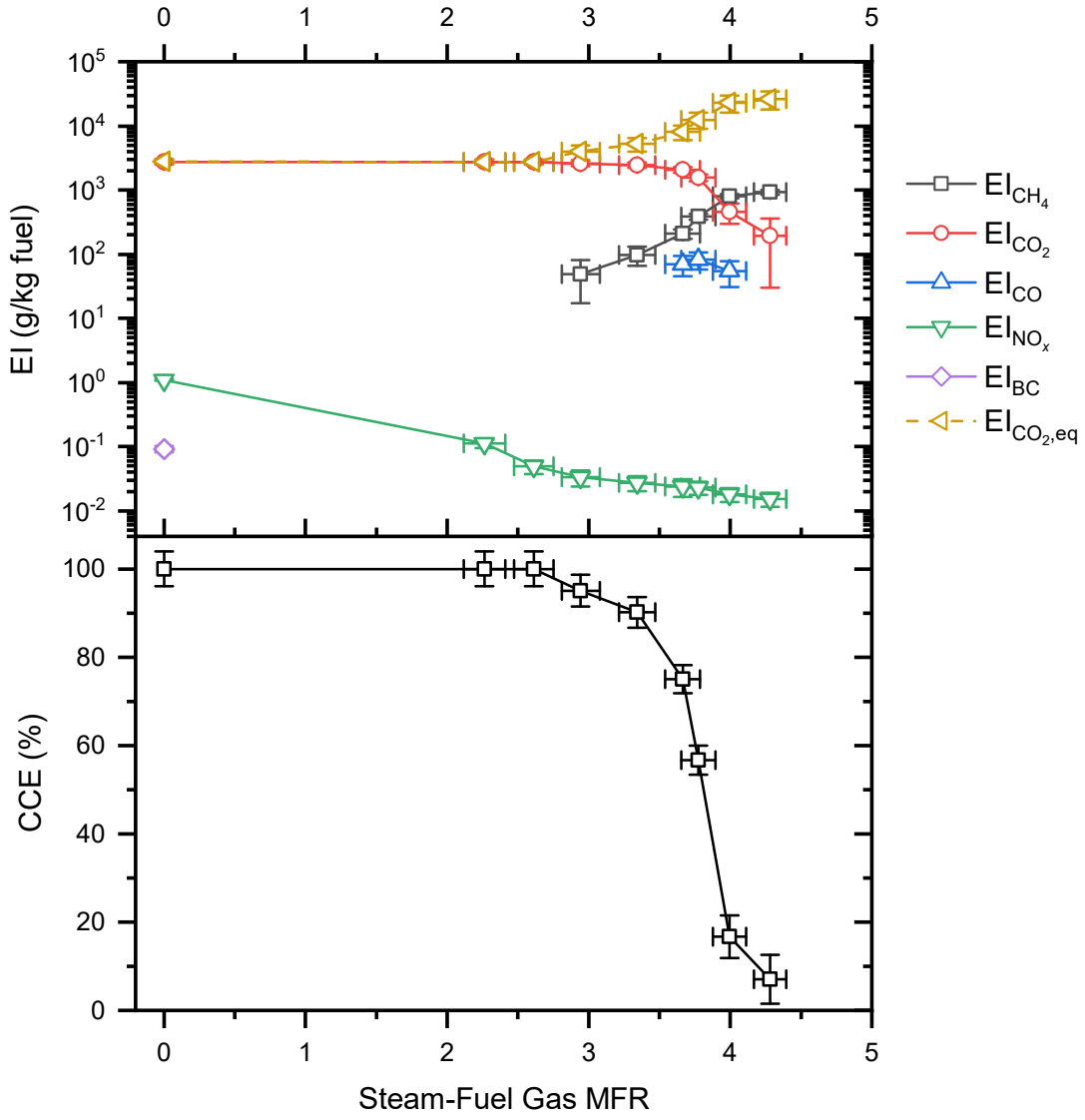

Figure 3.9: Experimental set 5 CCE plot (bottom) and EI plot (top).

3.8 Experimental Set 6: Burning 20 SLPM of C_3H_8

One of the features of the industry- and government-led studies was to examine the effect of the flare gas LHV on combustion performance. With the same intent, the fuel gas for the current experimental set was changed from CH_4 to C_3H_8, thereby increasing the LHV by a factor of 2.5 from 32.8 MJ/m^3 to 84.9 MJ/m^3. As can be seen from the EI plot in Figure 3.10, the most apparent difference from the unassisted C_3H_8 flame was the significantly higher EI_{BC} value of 2.74 g BC/kg fuel, which was 36 times greater than the amount generated from the unassisted CH_4 flame in experimental set 1. This difference was visible from the larger and more luminous

unassisted C_3H_8 flame as shown in Figure 3.11, compared to the CH_4 flame in Figure 3.5. The addition of steam to the flame was effective at eliminating BC fairly rapidly at a steam-to-fuel gas MFR of only 1.1, which reduced EI_{BC} by nearly three orders of magnitude. This was comparable to the amount of steam required to reduce EI_{BC} to the same levels for the CH_4 flame. A photograph representing this operating point is shown in Figure 3.11 and shows the contrast in luminosity of the flame with steam injection. Another notable difference between the present experimental set and all the previous ones was the relatively low production of NO_x for the unassisted flame. An EI_{NO_x} of 0.60 g NO_x/kg fuel was generated, which was only half the amount produced as the reference experimental set. The EI_{NO_x}, however, dropped steadily with increasing steam-to-fuel gas MFR in a similar fashion to experimental set 1. As shown in Figure 3.10 and the corresponding photograph of the C_3H_8 flame in Figure 3.11, the collapse in the CCE began at a steam-to-fuel gas MFR of 2.2, at which point unburned C_3H_8 and the reformed hydrocarbons CH_4 and C_2H_6 were first detected. The average breakdown of EI_{THC} during the collapse in CCE was 0.7% CH_4, 0.2% C_2H_6, and 99.1% C_3H_8, which demonstrates that fuel stripping was the dominant cause of the CCE collapse. The early onset in the CCE collapse as well as the short collapse phase over a steam-to-fuel gas MFR range of only 0.5 (*i.e.*, 2.2 – 2.7), were similar to that of experimental set 3. This may be due to the high inner to outer jet exit velocity ratio at a CCE of 96.5% of 15.8 coupled with the high average fuel exit Reynolds number of 2 000, which may have contributed to excessive turbulence in the outer shear layer and a disruption in the combustion process. During the collapse phase of CCE, a maximum EI_{CO} of 35.9 g CO/kg fuel was produced at a steam-to-fuel gas MFR of 2.3. This was notably smaller than the amount generated by the reference experimental set. The same reasons offered for the improved fuel-air mixing found in experimental sets 2 and 3 can be used to explain this reduced EI_{CO}, which were the robust inner potential core and subsequent growth of the outer shear layer due to the high inner to outer jet exit velocity as well as the earlier onset of vortices in the outer shear layer due to the high fuel Reynolds number. Another significant result was the profile of the $EI_{CO_2,eq}$ plot as shown in Figure 3.10. Unlike the previous experimental sets, the maximum $EI_{CO_2,eq}$ value of 5.4 kg CO_2/kg fuel for the present experimental

set was relatively small in comparison and was associated with the high BC content of the unassisted C_3H_8 flame. While the previous experimental sets had maximum $EI_{CO_2,eq}$ values corresponding to the lowest CCE operating points where CH_4 was being heavily vented, the collapse in CCE for the present experiment only brought about a moderate increase in $EI_{CO_2,eq}$. This was due to C_3H_8 having a 100-year GWP eight times smaller than that of CH_4. As a result of the unique $EI_{CO_2,eq}$ profile for the present experimental set, the optimal steam-to-fuel gas MFR range had a lower bound at an MFR of 0.9 at which point $EI_{CO_2,eq}$ returned to the baseline set by EI_{CO_2} and an upper bound at an MFR of 2.2 at which point CCE dropped to 96.5%.

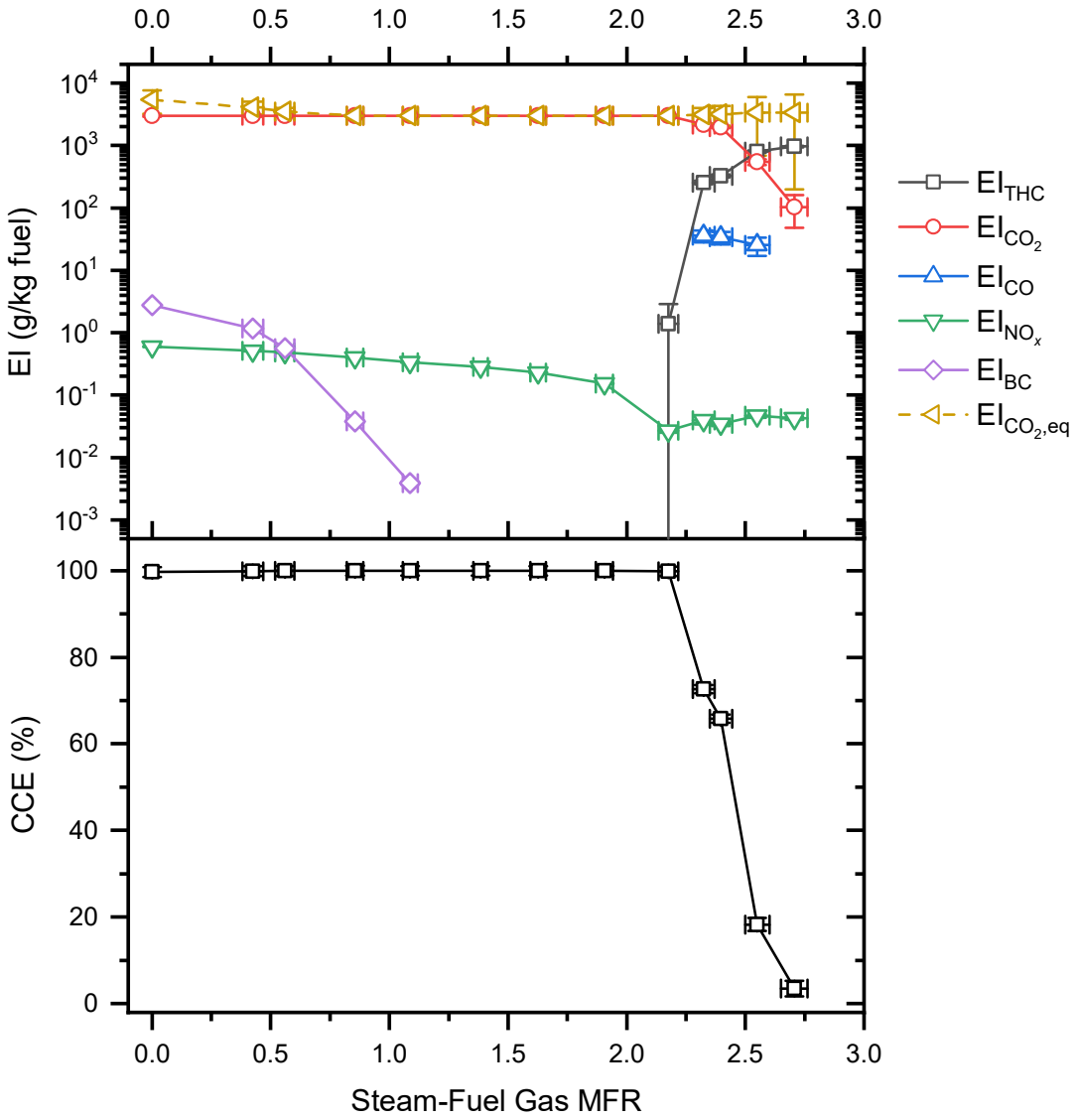

Figure 3.10: Experimental set 6 CCE plot (bottom) and EI plot (top).

Figure 3.11: Photos of experimental set 6 flame taken at increasing steam-to-fuel gas MFRs.

3.9 Experimental Set 7: 40 SLPM CH_4 Flame with Steam Outer Coflow

While experimental sets 2 – 6 differed from the reference set with respect to only one operating parameter, the present experimental set diverged in two ways. Firstly, the burner configuration was reversed such that the fuel gas flowed through the inner tube rather than the annular space and vice versa for the steam. This was attempted in order to investigate the effect of surrounding the internal jet of fuel with an inert annular jet. The second difference between the present experimental set and the reference experimental set, although inadvertent, was the fuel flow rate choice of 40 SLPM rather than 20 SLPM. At a fuel flow rate of 20 SLPM, the lowest possible steam mass flow rate (*i.e.*, 14 g/min), extinguished the flame. By increasing the fuel flow rate to 40 SLPM, the flame stability was improved. Therefore, the present experimental set had an inverse flow configuration compared to experimental set 2. At a fuel flow rate of 40 SLPM compounded with the smaller inner tube flow area (*i.e.*, 100 mm^2 for inner coflow versus 286 mm^2 for outer coflow), a distinguishing feature of the fuel flow in the present experimental set was its turbulent exit Reynolds number of 4 144

as presented in Table 3.3. As a result of the fuel having the highest exit velocity and momentum compared to previous experimental sets and therefore the most highly developed outer shear layer, the EI_{BC} generated by the unassisted flame was the lowest of all experimental sets at 0.007 g BC/kg fuel as shown in Figure 3.12. A photograph of the unassisted flame is also shown in Figure 3.13. The center photograph of the flame in Figure 3.13 coincided with the initial steam injection point at a steam-to-fuel gas MFR of 0.52 and illustrated the defining feature of the present experimental set, which was the lifting of the flame from the tip of the burner. The CCE of the flame remained at 100% at this point and EI_{BC} production was unchanged. In fact, EI_{BC} remained constant until a steam-to-fuel gas MFR of 0.81, after which it was eliminated. The maximum EI_{NO_x} generated was 0.97 g NO_x/kg fuel at zero steam assist and was less than the reference experimental set. The last steam injection point before the collapse in CCE was at a steam-to-fuel gas MFR of 0.97, which yielded a CCE of 98.8% and a higher lifted flame as shown in Figure 3.13. The next steam injection point at a steam-to-fuel gas MFR of 1.04 completely extinguished the flame, unlike any of the previous experimental sets in which a small residual flame remained. The quick collapse in CCE may have been caused by the inert annular jet of steam acting as a barrier between the fuel and combustion air. As a result of the sudden collapse in CCE and complete failure in the combustion process, CO was never detected.

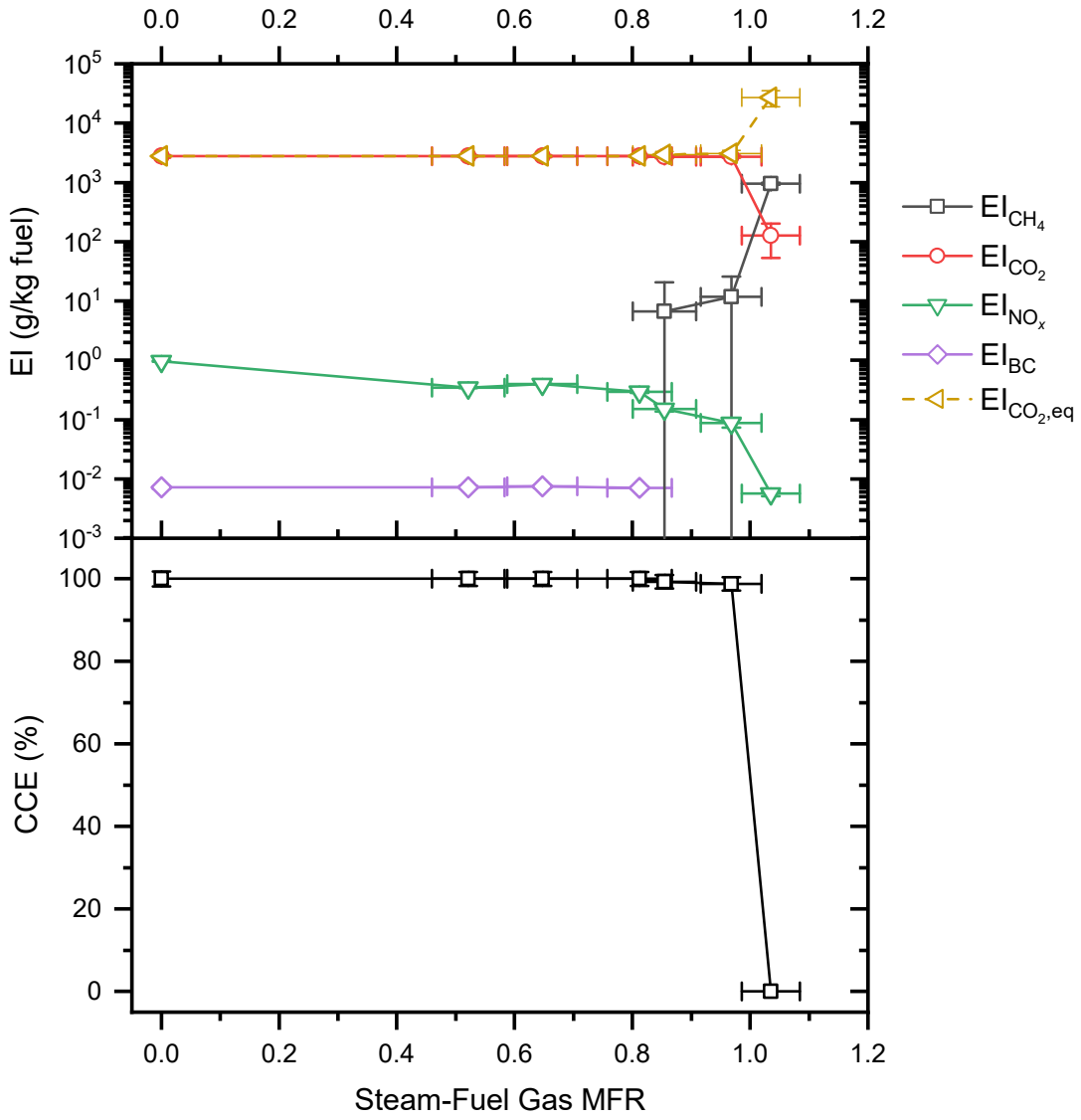

Figure 3.12: Experimental set 7 CCE plot (bottom) and EI plot (top).

Figure 3.13: Photos of experimental set 7 flame taken at increasing steam-to-fuel gas MFRs.

3.10 Analysis of Hydrodynamic Conditions at Burner Exit Plane

The effect of increasing the assist fluid mass flow rate on the flame CCE was captured for each of the experimental sets as shown in Figure 3.14.

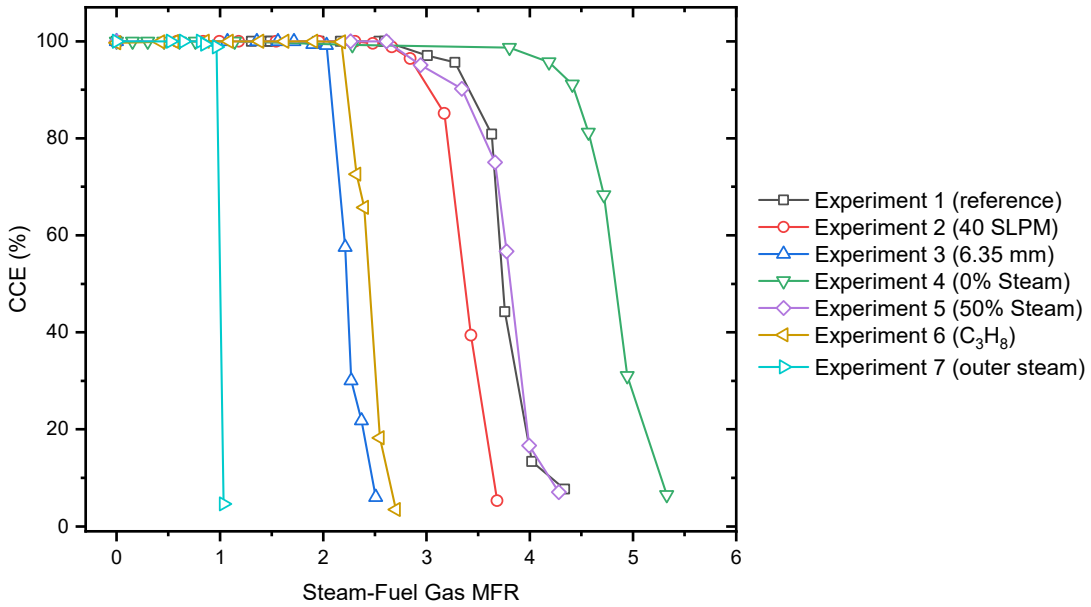

Figure 3.14: The response of CCE to increasing mass flow rates of assist fluid for experimental sets 1 – 7.

In order to resolve any potential trends between the steam and fuel exit velocity gradients and CCE, the steam-to-fuel gas exit velocity ratio (VR_{zz}), with both steam and fuel in the *z*-direction, was calculated for experimental sets 1 – 6 and plotted as shown in Figure 3.15. Experimental set 7 was excluded due to the different flow configuration.

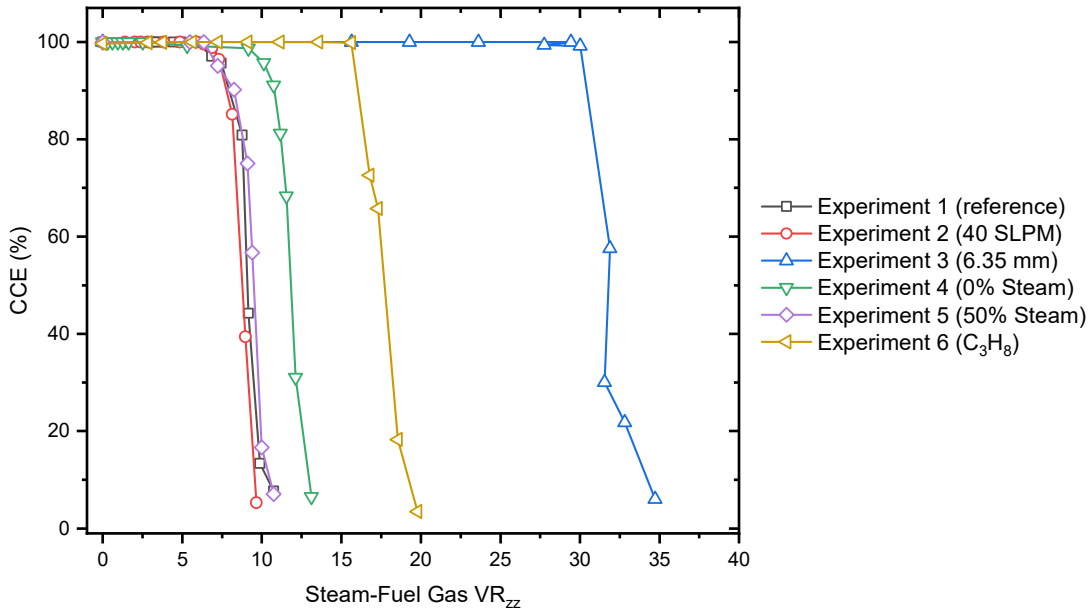

Figure 3.15: Response of CCE to increasing steam-to-fuel gas velocity ratio for experimental sets 1 – 6.

To take into account the density of the assist and fuel streams, the steam-to-fuel gas momentum ratio (MR_{zz}), also with both steam and fuel in the *z*-direction, was calculated for experimental sets 1 – 6 by taking the product of MFR and VR_{zz} as shown in Figure 3.16.

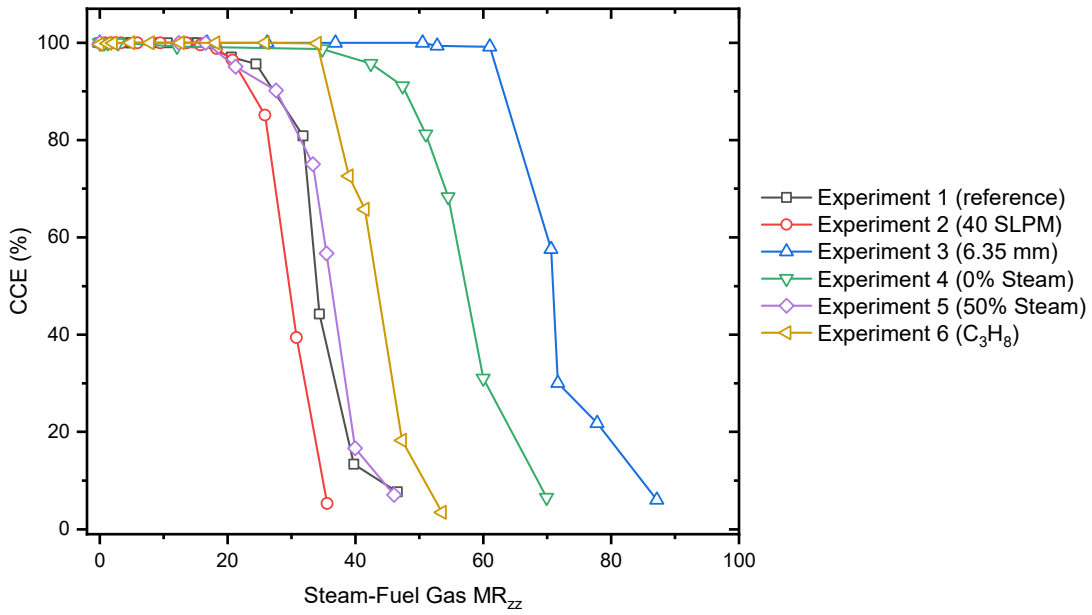

Figure 3.16: Response of CCE to increasing steam-to-fuel gas momentum ratio for experimental sets 1 – 6.

Although the redefining of the relationship between steam and fuel and CCE in terms of velocity and momentum ratio did not collapse the experimental sets into one common trend, it did allow for more insight into the combustion process at varying hydrodynamic exit conditions. When characterizing the behaviour of the flame at increasing steam-to-fuel gas MFR values, it was necessary to analyze the hydrodynamic properties of the steam and fuel gas at the burner exit in order to discern the velocity and momentum gradients that may have contributed to improved fuel-air mixing or increased the flame's susceptibility to sudden instabilities. Experimental set 3, for instance, had a VR_{zz} and MR_{zz} approximately four and three times greater than those of experimental set 1, as shown in Figure 3.15 and 3.16, respectively. This underlined the potential value in implementing high velocity jets of steam in steam-assisted flare heads for ensuring optimal fuel-air mixing and, as shown by experimental sets 3 and 6, eliminating incomplete combustion. When the flame was capable of sustaining higher steam-to-fuel velocity ratios as for experimental sets 3 and 6, however, there was an increased risk of a rapid decline in CCE due to excessive turbulence in the outer shear layer, which presented concerns from an operational standpoint and a requirement for the cautious administration of steam assist. This

therefore pointed towards the limiting factor for increasing the flow rate of steam for the velocity dominated experimental sets 3 and 6, which may have been the excessive turbulence generated in the outer shear layer. For the mass dominated experimental sets 1, 2, 4, and 5, the limiting factor for increased steam flow rate may have been the relatively less pronounced inner potential core and therefore increased dilution of reactants with inert assist fluid.

3.11 Comparing Experimental Results to Industry- and Government-Led Studies

A summary of the steam-to-fuel gas MFRs corresponding to a CCE of 96.5% along with the maximum EIs in the CCE range of ≥ 96.5% for each of the experimental sets is shown in Table 3.5. The maximum EIs were presented in order to establish the acceptable emissions limits for the various operating conditions as is done in industry. The 96.5% CCE threshold was adopted as a cut-off point by which the results from the present study can be compared to those found by industry. The recommended steam-to-fuel gas MFR operating range for each of the experimental sets are also shown in Figure 3.17. The range for each experimental set was bounded on the left by the steam-to-fuel gas MFR at which point the EI_{BC} dropped by an order of magnitude starting from the unassisted flame case, while the right bound was the steam-to-fuel gas MFR corresponding to a CCE of 96.5%. For the seventh experimental set, the left bound of the recommended steam-to-fuel gas MFR operating range was coincident with the unassisted flame point due to the EI_{BC} remaining consistent with increasing steam flow rate.

Table 3.5: Steam-fuel gas MFR at CCE of 96.5% and maximum EIs for CCE ≥ 96.5%.

Experimental Set	Steam-Fuel Gas MFR at CCE = 96.5%	Emission Indices (g/kg fuel)			
		THC	CO_2	NO_x	BC
1	3.1	29.76	2743	1.21	0.076
2	2.8	11.78	2743	0.88	0.017
3	2.0	7.93	2743	1.15	0.161
4	4.1	13.15	2743	1.15	0.115
5	2.8	–	2743	1.10	0.092
6	2.2	1.39	2994	0.60	2.742
7	1.0	11.81	2743	0.97	0.007

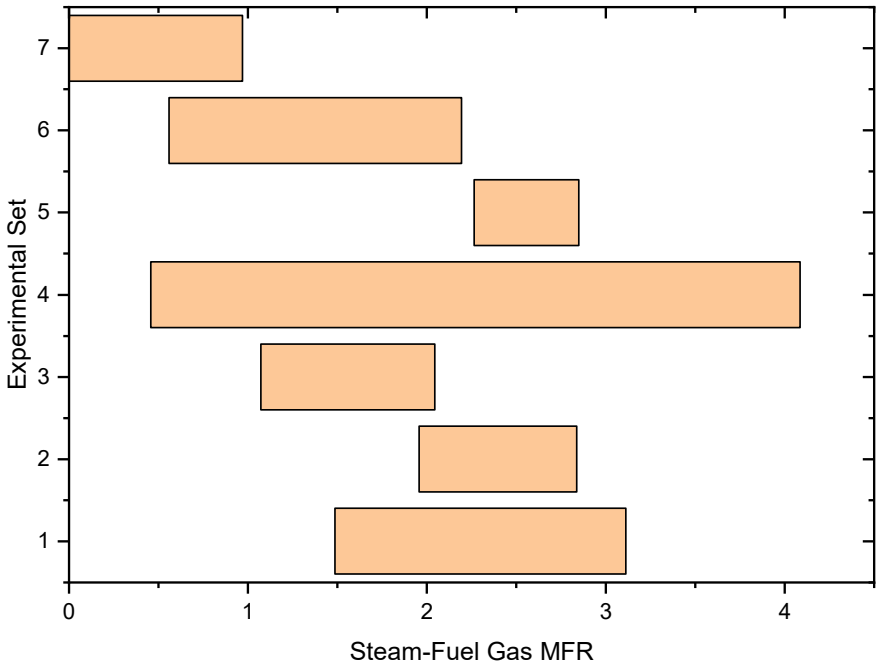

Figure 3.17: Recommended steam-to-fuel gas MFR operating ranges for experimental sets 1 – 7.

Beginning with McDaniel's [40] steam-assisted flare study in which a 0.22 m ID flare stack was utilized, two flare gases were tested having LHVs of 12.0 MJ/m^3 and 81.3 MJ/m^3, respectively. For the 12.0 MJ/m^3 LHV flare gas, which was less energy dense than CH_4 and C_3H_8 (*i.e.*, LHVs for CH_4 and C_3H_8 are 32.8 MJ/m^3 and 84.9 MJ/m^3, respectively), McDaniel recommended a maximum steam-to-flare gas MFR of 0.17 for a CCE ≥ 96.5%. This MFR value was considerably smaller than the recommended steam-to-fuel gas MFRs for any of the experimental sets in the present study, as can be seen in Table 3.5. Furthermore, McDaniel presented maximum EI values for a CCE ≥ 96.5% for EI_{THC}, EI_{CO_2}, and EI_{NO_x} values of 0.96 g THC/kg fuel, 869 g CO_2/kg fuel, and 0.23 g NO_x/kg fuel, respectively, which were also considerably lower than any of those listed in Table 3.5 for the present study. Surprisingly, McDaniel presented a maximum EI_{CO} value of 4.03 g CO/kg fuel for a CCE ≥ 96.5% which was a species that was never detected for any of the experimental sets performed in the present study at this CCE range. For McDaniel's 81.3 MJ/m^3 flare gas case, the maximum recommended steam-to-flare gas MFR was stated as 3.6

for a CCE ≥ 96.5%. Based on the flare gas used, experimental set 6 of the present study would be the most comparable due to C_3H_8's LHV of 84.9 MJ/m^3. Despite the similarity in LHV of the fuel gas, however, the recommended steam-to-fuel gas MFR from the present study was only 2.2 for a CCE ≥ 96.5%. However, most of McDaniel's EIs for the 81.3 MJ/m^3 flare gas were highly comparable to those from experimental set 6. McDaniel presented maximum EIs for a CCE ≥ 96.5% for EI_{THC}, EI_{CO_2}, and EI_{NO_x} values of 1.76 g THC/kg fuel, 3 103 g CO_2/kg fuel, and 1.88 g NO_x/kg fuel, respectively, which were similar to those listed for experimental set 6 in Table 3.5. As with the 12.0 MJ/m^3 flare gas, the maximum EI_{CO} value of 23.44 g CO/kg fuel generated for the 81.3 MJ/m^3 flare gas at a CCE ≥ 96.5% was unexpected.

Pohl *et al*. [43] studied an 8.9 cm OD steam-assisted flare burning a flare gas with an LHV of 49.3 MJ/m^3. According to his experiments, the maximum steam-to-flare gas MFR was 1 for a CCE ≥ 96.5%. This result replicated that of experimental set 7 which had the same maximum steam-to-fuel gas MFR for a CCE ≥ 96.5%. A possible explanation for this similarity is Pohl *et al.*'s use of the upper steam-assist method which could potentially have caused a lifted flame in the same manner as in experimental set 7. Pohl and Soelberg [45] extended the work of Pohl *et al*. with a 30.5 cm OD flare head burning a flare gas with an LHV of 13.6 MJ/m^3. Based on their experimental results, a CCE of ≥ 96.5% was sustained up to a steam-to-flare gas MFR of 3.3. This was very similar to the steam-to-flare gas MFR of 3.1 for a CCE ≥ 96.5% achieved in experimental set 1 despite burning CH_4 which has a considerably lower LHV value of 32.8 MJ/m^3. In terms of EI data, Pohl and Soelberg only presented a maximum EI_{NO_x} value of 0.03 g NO_x/kg fuel at a CCE ≥ 96.5% for an experiment burning a flare gas with LHV of 15.8 MJ/m^3. This value was significantly lower than any of the EI_{NO_x} values measured in the same CCE range for all experimental sets in the present study.

The most recent comprehensive steam-assisted flare gas study was performed by Allen and Torres [47], who operated a flare stack with a 91.4 cm tip diameter. A variety of flare gas LHVs and flow rates were tested, although most tests burned a 13.0 MJ/m^3 LHV flare gas. For this LHV value, steam-to-flare gas MFRs of 0.25 and 0.32 were recommended for the low and high flare gas flow rates (*i.e*., 425 kg/hr and

1 062 kg/hr), respectively, in order to remain at a CCE ≥ 96.5%. For their 22.8 MJ/m^3 LHV flare gas flowing at 1 083 kg/hr, Allen and Torres stated a steam-to-flare gas MFR of 0.84 for a CCE ≥ 96.5%. The maximum steam-to-flare gas MFRs for both flare gas LHVs for a CCE ≥ 96.5% were considerably less than those established by the experimental sets in the present study which had an average maximum steam-to-fuel gas MFR for the same CCE range of 2.6. For flares burning gases with an average LHV of 13.1 MJ/m^3, an EI_{THC} of 5.29 g THC/kg fuel was provided, which was within the range of those identified in the present study. A slightly increased flare gas LHV of 13.9 MJ/m^3 yielded an EI_{NO_x} of 0.17 g NO_x/kg fuel which, like McDaniel's study with the 12.0 MJ/m^3 flare, was much lower than the amount of NO_x produced in experimental sets 1 – 7. Finally, based on Allen and Torres' data for a flare gas with an LHV of 22.1 MJ/m^3, Fortner *et al*. [48] estimated an EI_{BC} of 0.016 g BC/kg fuel. This was similar to the maximum EI_{BC} values at a CCE ≥ 96.5% of 0.017 g BC/kg fuel and 0.007 g BC/kg fuel generated in experimental sets 2 and 7, respectively, which were defined by their high exit momentum fuel gases.

A number of reasons can be provided to explain the discrepancies between the results from the industry-scale flare studies and the present lab-scale study, with the most apparent being the difference in flare head diameters and flare gas and steam assist flow rates. As a result of the significantly higher stack diameters and flaring flow rates, industrial flares operate at a considerably higher Reynolds number regime in the range of 10^3 – 10^7, as was pointed out in Table 1.1. In comparison, the experiments performed in the present study only operated in a Reynolds number regime of 10^2 – 10^4 for the fuel and steam flows. One of the observations from the seven experimental sets completed was that those with the highest fuel or steam exit Reynolds number typically experienced the most rapid onset of collapse in CCE. The same reasoning may be applied to explain why Allen and Torres' industrial steam-assisted flare experienced an even earlier collapse in CCE. Furthermore, industrial-scale flares are usually equipped with multiple narrow-diameter steam injection nozzles for delivering the steam at a greater velocity. As shown by experimental set 3, steam delivered at a higher steam-to-fuel gas MR had a profound effect on minimizing the required MFR required to achieve a CCE of 96.5%, which could also

explain the smaller steam-to-fuel gas MFRs stated by Allen and Torres. Another major difference between industrial steam-assisted flaring and the present study is industry's use of saturated steam as indicated by the EPA [61], which is the state that water occupies where the liquid and vapour phases coexist in equilibrium. With saturated steam having a higher specific heat capacity than superheated steam, which was the predominant state of steam in the present study, there is a possibility that industrial steam-assisted flares may experience a higher degree of cooling especially with the use of lower quality steam. This potentially explains the more rapid drop in CCE found in the industrial studies as well as the typically lower EI_{NO_x} values presented.

Chapter 4

4. Conclusions and Recommendations for Future Work

4.1 Conclusions

A lab-scale flaring facility was established in order to investigate the industrial practice of steam-assisted flaring in a controlled environment. For simplicity and repeatability, steam-assisted flaring was simulated using a coflow burner design that consisted of two concentric tubes with coincident exit planes in which steam flowed through the inner tube and fuel gas through the annular space or vice versa. Thermocouples were used to capture the temperatures at the exit plane of the inner tube and annular space as well as at four additional locations below the exit plane in the annular space.

The fuel gases selected for experimentation were CH_4 and C_3H_8, whose temperatures were regulated to 23 °C in a heated water bath before being metered out by a mass flow controller to the burner. An electric steam boiler was used to generate the steam required to perform steam coflow tests. To measure the mass flow rate of steam, an obstruction-type flow meter in conjunction with a differential pressure transmitter, an absolute pressure transmitter, and an RTD probe were used to provide the steam flow properties necessary to calculate mass flow rate. The steam was metered to the burner by means of a heated hose to elevate the steam from a saturated to superheated state and thereby prevent condensation from occurring.

An exhaust hood positioned above the burner ensured that the entire plume of the flame was captured, which then flowed through a duct at a turbulent Reynolds Number to ensure well-mixedness of the combustion products. A probe installed in

the duct was used to extract samples of the diluted combustion products to be analyzed by an array of diagnostic instruments. One of these instruments was a PAX which evaluated the BC mass concentration of the duct sample based on measured optical properties of the BC. An NO_x analyzer was used to measure the concentration of NO_x in the sample on the basis of a chemiluminescent reaction. A sample of the combustion products was also stored in a Tedlar bag for injection into a GC for the measurement of the mole concentration of $C_1 – C_3$ hydrocarbons, and non-hydrocarbons such as O_2, N_2, CO_2, and CO.

A closed carbon mass balance was established around the combustion process in order to keep track of the carbon-based species, including hydrocarbons in the fuel and products of incomplete combustion such as CO_2, CO, $C_{(s)}$, and unburned or reformed hydrocarbons. This was a prerequisite for determining the carbon conversion efficiency of the flame, which was defined as the ratio of the mass of carbon produced by the reaction in the form of CO_2 to the mass of carbon in the form of hydrocarbons in the fuel gas stream. The emission indices for CO, CO_2, THC, NO_x, and BC were also calculated for each of the operating points performed in the present study and was defined as the ratio of the species' mass emission rate generated by combustion to the mass flow rate of the fuel gas to the burner.

A total of seven experimental sets were performed in the present study to investigate the effect of varying the burner operating conditions on the CCE and EIs for THC, CO_2, CO, NO_x, and BC. The reference case—experimental set 1—was established as the benchmark for which all other experimental sets were compared to. The burner was configured with a 12.7 mm OD inner tube with inner steam coflow injected into a 20 SLPM CH_4 flame. The unassisted flame yielded an EI_{NO_x} and EI_{BC} of 1.21 g NO_x/kg fuel and 0.076 g BC/kg fuel, respectively, at a CCE of 100%. With the increasing in steam-to-fuel gas MFR, the EI_{NO_x} and EI_{BC} values dropped by over an order of magnitude each. The drop in EI_{NO_x} was attributed to the cooling effect of steam on the flame product gas temperature whereas the decrease in EI_{BC} was attributed to the improved mixing of the fuel with combustion air as a result of the development of the outer shear layer that was promoted by the robust inner potential core. Chemical effects due to the suggested increased presence of OH radicals may

also have had an impact in promoting complete combustion. The onset of collapse in CCE at 96.5% occurred at a steam-to-fuel gas MFR of 3.1. At this point, the nominal EI_{CO_2} value of 2.7 kg CO_2/kg fuel began to drop while EI_{CH_4} at 29.76 g CH_4/kg fuel began to increase due to fuel being stripped away from the combustion zone. During the CCE collapse phase, a maximum EI_{CO} of 85.57 g CO/kg fuel was generated. The CCE continued its descent until 8% at which point the EI_{CH_4} and $EI_{CO_2,eq}$ peaked at 923.4 g CH_4/kg fuel and 26.1 kg CO_2/kg fuel, respectively.

Experimental set 2 involved a doubling of the fuel flow rate to 40 SLPM of CH_4. A difference that was immediately noticed was the maximum EI_{BC} value being only a quarter of the reference set at 0.017 g BC/kg fuel. This was attributed to the near doubling of the fuel exit velocity which promoted the growth of the outer shear layer. Compared to the reference set, the onset in CCE collapse occurred earlier at a steam-to-fuel gas MFR of 2.8. During the CCE collapse phase, the maximum EI_{CO} was 27% less than that of the previous experimental set. This was attributed to the earlier onset of vortex formation in the outer shear layer due to increased fuel Reynolds and therefore better fuel-air mixing.

For experimental set 3, the inner tube diameter was replaced with one having a 6.35 mm OD. As a result of the reduced velocity of the fuel stream as it exited the burner, the maximum EI_{BC} value of 0.161 g BC/kg fuel was twice that of the reference experimental set. Due to the greatly increased velocity and momentum of the steam jet, especially with respect to the fuel, the onset in collapse of CCE occurred considerably earlier than the reference experimental set at a steam-to-fuel gas MFR of 2.0. As the CCE was dropping, however, CO was undetected unlike the two previous experimental sets. The high velocity gradient between the steam and fuel flows may have contributed to excessive turbulence in the outer shear layer which disrupted the combustion process.

The aim of experimental set 4 was to replace the inner steam coflow with a 58% N_2 and 42% He heated gas mixture in order to match steam in terms of molecular weight and density. Despite the hydrodynamic similarity between the gas mixture and steam, the onset of collapse for CCE occurred at a significantly greater equivalent steam-to-fuel gas MFR of 4.1. This was attributed to the lower exit Reynolds Number

of the gas mixture compared to steam due to its higher viscosity, thus delaying the onset of fuel stripping from the combustion zone. Experimental set 5 was a continuation of the investigation of the unique effect of steam on combustion, in which the inner coflow comprised of 50% steam with the remainder being N_2 and He in the same proportions as experimental set 4. Overall, the results of this experimental set were highly comparable to those of the reference experimental set, with the onset of the CCE collapse happening at an equivalent steam-to-fuel gas MFR of 2.8.

The purpose of experimental set 6 was to investigate the response of a higher LHV fuel in C_3H_8 to steam coflow. Initially, the most apparent difference was the significantly higher EI_{BC} generated by the unassisted flame at 2.742 g BC/kg fuel. As with experimental set 3, the onset in the CCE collapse and the duration of the collapse was sudden in comparison to the reference experimental set. The exceedingly high Reynolds numbers of the steam and fuel jets could have prompted instabilities in the flame leading to the rapid CCE collapse. Furthermore, the CCE collapse phase yielded a maximum EI_{CO} of only 35.86 g CO/kg fuel. This could have been due to the high velocity gradient between steam and fuel, which in a similar manner to experimental set 3, promoted a higher degree of outer shear layer growth and by extension fuel-air mixing as compared to the reference experimental set. Another important result was the $EI_{CO_2,eq}$ trend which began at a maximum of 5.4 kg CO_2/kg fuel due to the high BC emissions and did not experience the sharp incline during the CCE collapse phase. This was due to C_3H_8's diminished role in global warming compared to CH_4.

Experimental set 7 inverted the steam and fuel flow configuration. The fuel flow rate of CH4 was selected as 40 SLPM CH_4 due to the lower limit on the steam mass flow rate. This led to the fuel having the highest exit Reynolds number, velocity, and momentum compared to the previous experimental sets. The resulting unassisted flame had the lowest EI_{BC} value of 0.007 g BC/kg fuel. Of all the experimental sets, this experimental set experienced the earliest onset of CCE collapse at a steam-to-fuel gas MFR of 0.97, after which the flame was completely extinguished. The quick collapse in CCE may have been caused by the lifted nature of the flame and the inert annular jet of steam acting as a barrier between the fuel and combustion air.

Industrial-scale steam-assisted flare studies performed by McDaniel, Pohl *et a*l., Pohl and Soelberg, and Allen and Torres were compared to the results from experimental sets 1 – 7. In general, the steam-to-fuel gas MFRs recommended by the industrial studies outlined were less than those established by the experimental sets in the present study. The maximum EIs at a CCE of ≥ 96.5% for THC, NO_x, and BC were also less than those generated by the experimental sets. One of the primary reasons for the discrepancy between the industrial-scale flare studies and the present lab-scale study was the difference in flare head diameters and flare gas and steam assist flow rates. The resulting orders of magnitude in variation between the Reynolds number regimes of these two scales meant that direct comparisons would inherently be flawed. A difference that possibly explained the relatively lower requirement of steam mass flow rate by industry was their use of saturated steam with a potentially high degree of moisture. In comparison to the superheated steam typically used in the present study, wet steam has a considerably higher specific heat capacity and therefore a greater potential for cooling the flame product gas temperature.

4.2 Recommendations for Future Work

In order to expand on the present study and make the results more applicable to industry, one of the main recommendations would be to scale up the burner diameter. An initial scaling factor of three could be implemented to increase the current burner OD from 25.4 mm to 76.2 mm, thereby extending the experimental framework from a strictly lab-scale flare to a small industrial flare representative of some found in industry. By doing so, the trends in the CCE and various EIs could be tracked with increasing steam-to-fuel gas MFRs and compared to the ones established by the present study as well as by industry. Another aspect of the burner geometry that could be modified to better understand the center steam-assist method is recessing the tip of the inner tube below the outer tube to study the effect of premixing the steam and fuel before the combustion zone during inner steam coflow. The inner tube could be tested at different heights below the burner tip to find an optimal location for introducing a high momentum jet to augment that of the fuel. More variations in the fuel gas LHV

could also be experimented with, especially closer to the 11.2 MJ/m^3 limit imposed by federal statute, to better align the results with those obtained by industry.

To gain a deeper insight into the results presented in the current study, further analysis could be performed in the following three areas: thermal, hydrodynamic, and chemical. One possible method for better understanding the effect of steam-assist on combustion is by inserting a thermocouple into the flame to monitor flame temperature. Data could be collected to study the effect of assist fluids with varying specific heat capacities—whether saturated steam, superheated steam, or an inert gas mixture—on the flame temperature. This information could then be used to generate a correlation between the changes in flame temperature under different assist conditions and NO_x formation. To better characterize the hydrodynamic interaction between the center jet, annular jet, and ambient air, a way of visualizing the flows beyond the tip of the burner would be highly valuable. This could be achieved through the use of Particle Image Velocimetry (PIV), in which the velocity field could be discerned by seeding the steam and fuel flows with tracer particles and illuminating the coflow jet streams by a laser sheet to observe flow structures. Lastly, the potential chemical effect of steam on combustion through the water-gas shift reaction in which the concentration of OH radicals increases to promote complete combustion can be further investigated by the use of spectroscopy. In this way, the chemiluminescence from OH radicals can be detected during the CCE collapse phase to evaluate the OH radical concentration and provide insight into its effect on CO concentrations.

Bibliography

[1] Understanding flares, ExxonMobil. (n.d.). http://www.exxonmobil.com.sghttps://www.exxonmobil.com.sg/en-sg/company/business-and-operations/operations/understanding-flares (accessed December 23, 2018).

[2] T.A. Brzustowski, Flaring in the energy industry, Progress in Energy and Combustion Science. 2 (1976) 129–141. doi:10.1016/0360-1285(76)90009-5.

[3] Global Gas Flaring Reduction Partnership (GGFR), World Bank. (n.d.). http://www.worldbank.org/en/programs/gasflaringreduction (accessed November 24, 2018).

[4] C.D. Elvidge, M.D. Bazilian, M. Zhizhin, T. Ghosh, K. Baugh, F.-C. Hsu, The potential role of natural gas flaring in meeting greenhouse gas mitigation targets, Energy Strategy Reviews. 20 (2018) 156–162. doi:10.1016/j.esr.2017.12.012.

[5] National Research Council (U.S.), The Instrumental Record, in: Surface Temperature Reconstructions for the Last 2,000 Years, National Academies Press, Washington, D.C, 2006: p. 145.

[6] Thomas F. Stocker, Dahe Qin, Gian-Kasper Plattner, Melinda M.B. Tignor, Simon K. Allen, Judith Boschung, Alexander Nauels, Yu Xia, Vincent Bex, Pauline M. Midgley, IPCC, 2013: Climate Change 2013: The Physical Science Basis. Contribution of Working Group I to the Fifth Assessment Report of the Intergovernmental Panel on Climate Change, Cambridge University Press, Cambridge, United Kingdom and New York, NY, USA, 2013. https://www.ipcc.ch/site/assets/uploads/2018/02/WG1AR5_all_final.pdf.

[7] Pieter Tans, Trends in Atmospheric Carbon Dioxide, Earth System Research Laboratory Global Monitoring Division. (2018). https://www.esrl.noaa.gov/gmd/ccgg/trends/ (accessed November 30, 2018).

[8] Ralph Keeling, Carbon Dioxide Measurements, Scripps Institution of Oceanography CO2 Program. (n.d.). http://scrippsco2.ucsd.edu/ (accessed November 30, 2018).

[9] James H. Butler, Stephen A. Montzka, NOAA/ESRL Global Monitoring Division - THE NOAA ANNUAL GREENHOUSE GAS INDEX (AGGI), Earth System Research Laboratory Global Monitoring Division. (2018). https://www.esrl.noaa.gov/gmd/aggi/aggi.html (accessed December 4, 2018).

[10] J.M. Cloy, K.A. Smith, Greenhouse Gas Sources and Sinks, in: Encyclopedia of the Anthropocene, Elsevier, 2018: pp. 391–400. doi:10.1016/B978-0-12-809665-9.09961-4.

[11] D.M. Leahey, K. Preston, M. Strosher, Theoretical and Observational Assessments of Flare Efficiencies, Journal of the Air & Waste Management Association. 51 (2001) 1610–1616. doi:10.1080/10473289.2001.10464390.

[12] Y. Shi, Y. Ji, H. Sun, F. Hui, J. Hu, Y. Wu, J. Fang, H. Lin, J. Wang, H. Duan, M. Lanza, Nanoscale characterization of PM2.5 airborne pollutants reveals high adhesiveness and aggregation capability of soot particles, Scientific Reports. 5 (2015). doi:10.1038/srep11232.

[13] J. Marshall, PM 2.5, Proceedings of the National Academy of Sciences. 110 (2013) 8756–8756. doi:10.1073/pnas.1307735110.

[14] B.M. Conrad, M.R. Johnson, Field Measurements of Black Carbon Yields from Gas Flaring, Environmental Science & Technology. 51 (2017) 1893–1900. doi:10.1021/acs.est.6b03690.
[15] T.J. Grahame, R. Klemm, R.B. Schlesinger, Public health and components of particulate matter: The changing assessment of black carbon, Journal of the Air & Waste Management Association. 64 (2014) 620–660. doi:10.1080/10962247.2014.912692.
[16] S.-Y. Kim, S.J. Dutton, L. Sheppard, M.P. Hannigan, S.L. Miller, J.B. Milford, J.L. Peel, S. Vedal, The short-term association of selected components of fine particulate matter and mortality in the Denver Aerosol Sources and Health (DASH) study, Environmental Health. 14 (2015). doi:10.1186/s12940-015-0037-4.
[17] T.C. Bond, S.J. Doherty, D.W. Fahey, P.M. Forster, T. Berntsen, B.J. DeAngelo, M.G. Flanner, S. Ghan, B. Kärcher, D. Koch, S. Kinne, Y. Kondo, P.K. Quinn, M.C. Sarofim, M.G. Schultz, M. Schulz, C. Venkataraman, H. Zhang, S. Zhang, N. Bellouin, S.K. Guttikunda, P.K. Hopke, M.Z. Jacobson, J.W. Kaiser, Z. Klimont, U. Lohmann, J.P. Schwarz, D. Shindell, T. Storelvmo, S.G. Warren, C.S. Zender, Bounding the role of black carbon in the climate system: A scientific assessment: BLACK CARBON IN THE CLIMATE SYSTEM, Journal of Geophysical Research: Atmospheres. 118 (2013) 5380–5552. doi:10.1002/jgrd.50171.
[18] K. Huang, J.S. Fu, A global gas flaring black carbon emission rate dataset from 1994 to 2012, Scientific Data. 3 (2016) 160104. doi:10.1038/sdata.2016.104.
[19] A. Stohl, Z. Klimont, S. Eckhardt, K. Kupiainen, V.P. Shevchenko, V.M. Kopeikin, A.N. Novigatsky, Black carbon in the Arctic: the underestimated role of gas flaring and residential combustion emissions, Atmospheric Chemistry and Physics. 13 (2013) 8833–8855. doi:10.5194/acp-13-8833-2013.
[20] O.G. Fawole, X.-M. Cai, A.R. MacKenzie, Gas flaring and resultant air pollution: A review focusing on black carbon, Environmental Pollution. 216 (2016) 182–197. doi:10.1016/j.envpol.2016.05.075.
[21] D.T. Allen, Emissions from oil and gas operations in the United States and their air quality implications, Journal of the Air & Waste Management Association. 66 (2016) 549–575. doi:10.1080/10962247.2016.1171263.
[22] M. Sanchez, Source Characterization of Volatile Organic Compounds Affecting the Air Quality in a Coastal Urban Area of South Texas, International Journal of Environmental Research and Public Health. 5 (2008) 130–138. doi:10.3390/ijerph2008050018.
[23] V.M. Torres, S. Herndon, Z. Kodesh, D.T. Allen, Industrial Flare Performance at Low Flow Conditions. 1. Study Overview, Industrial & Engineering Chemistry Research. 51 (2012) 12559–12568. doi:10.1021/ie202674t.
[24] E. Lavigne, S. Weichenthal, J. Wong, M. Smith-Doiron, R. Dugandzic, T. Kosatsky, Mortality and hospital admission rates for unintentional nonfire-related carbon monoxide poisoning across Canada: a trend analysis, CMAJ Open. 3 (2015) E223–E230. doi:10.9778/cmajo.20140122.

[25] J.S. Daniel, S. Solomon, On the climate forcing of carbon monoxide, Journal of Geophysical Research: Atmospheres. 103 (1998) 13249–13260. doi:10.1029/98JD00822.
[26] V.E. Fioletov, C.A. McLinden, N. Krotkov, C. Li, J. Joiner, N. Theys, S. Carn, M.D. Moran, A global catalogue of large SO2 sources and emissions derived from the Ozone Monitoring Instrument, Atmospheric Chemistry and Physics. 16 (2016) 11497–11519. doi:10.5194/acp-16-11497-2016.
[27] Eric V. Schaeffer, Frequent, Routine Flaring May Cause Excessive, Uncontrolled Sulfur Dioxide Releases, United States Environmental Protection Agency, 2000.
[28] Ambient Levels of Sulphur Dioxide, Environment and Climate Change Canada. (2017). https://www.ec.gc.ca/indicateurs-indicators/default.asp?lang=En&n=307CCE5B-1&pedisable=true (accessed November 26, 2018).
[29] J.J. Slaski, D.J. Archambault, X. Li, Evaluation of polycyclic aromatic hydrocarbon (PAH) accumulation in plants: the potential use of PAH accumulation as a marker of exposure to air emissions from oil and gas flares, Alberta Environment, Edmonton, Alberta, 2000.
[30] Government of Canada, Environment Canada, Health Canada, Polycyclic Aromatic Hydrocarbons, NATIONAL PRINTERS (OTTAWA) INC., Ottawa, 1994.
[31] William S. Schellentrager, Edward S. Bale, Howard G. Briggs, Flare stack tip, US2506972, 1950. https://patents.google.com/patent/US2506972A.
[32] Robert A. Verner, John P. Longwell, Flare stack apparatus for burning waste gases, US2761496, 1956. https://patents.google.com/patent/US2761496A.
[33] John S. Zink, Robert D. Reed, Flare stack gas burner, US2779399, 1957. https://patents.google.com/patent/US2779399A.
[34] API Standard 521: Pressure-relieving and Depressuring Systems, 6th ed., American Petroleum Institute (API), Washington, DC, 2014.
[35] Team up for Energy Savings – Compressed Air, Natural Resources Canada. (2016). https://www.nrcan.gc.ca/energy/publications/efficiency/industrial/cipec/5637 (accessed December 9, 2018).
[36] General control device and work practice requirements., 2018. https://www.ecfr.gov/cgi-bin/text-idx?SID=a2dc7bcb194fa81d82a6ff79a755e3b1&mc=true&node=se40.7.60_118&rgn=div8 (accessed December 10, 2018).
[37] Method 22 - Visual Determination of Fugitive Emissions, US EPA. (2016). https://www.epa.gov/emc/method-22-visual-determination-fugitive-emissions (accessed December 20, 2018).
[38] EPA Enforcement Targets Flaring Efficiency Violations, United States Environmental Protection Agency, 2012. https://www.epa.gov/sites/production/files/documents/flaringviolations.pdf.
[39] Requirements for flare control devices., 2018. https://www.ecfr.gov/cgi-bin/retrieveECFR?gp=&SID=ffd0ee8912d64077bd89a7a09e672b95&mc=true&

n=pt40.12.63&r=PART&ty=HTML#se40.12.63_1670 (accessed January 19, 2019).
[40] M. McDaniel, Flare Efficiency Study, U.S. Environmental Protection Agency, Washington, D.C., 1983. https://www3.epa.gov/ttnchie1/old/ap42/ch13/s05/reference/ref_01c13s05_jan1995.pdf.
[41] U.S. Environmental Protection Agency, AP-42: Compilation of Air Emissions Factors, 2018. https://www3.epa.gov/ttn/chief/ap42/ch13/final/C13S05_02-05-18.pdf (accessed December 25, 2018).
[42] J.D.N. McEwen, M.R. Johnson, Black carbon particulate matter emission factors for buoyancy-driven associated gas flares, Journal of the Air & Waste Management Association. 62 (2012) 307–321. doi:10.1080/10473289.2011.650040.
[43] J.H. Pohl, R. Payne, J. Lee, Evaluation of the Efficiency of Industrial Flares: Test Results, U.S. Environmental Protection Agency, Irvine, California, 1984.
[44] C. Shaddix, A. Molina, Ignition, flame stability, and char combustion in oxy-fuel combustion, in: Oxy-Fuel Combustion for Power Generation and Carbon Dioxide (CO2) Capture, Elsevier, 2011: pp. 101–124. doi:10.1533/9780857090980.2.101.
[45] J.H. Pohl, N.R. Soelberg, Evaluation of the Efficiency of Industrial Flares: Flare Head Design and Gas Composition, U.S. Environmental Protection Agency, Irvine, California, 1985.
[46] Coanda Flares, Trinvalco. (2014). http://www.trinvalco.com/John-Zink/coanda-flares (accessed January 8, 2019).
[47] D.T. Allen, V.M. Torres, TCEQ 2010 Flare Study Final Report, The University of Texas at Austin, 2011. https://www.tceq.texas.gov/assets/public/implementation/air/rules/Flare/2010flarestudy/2010-flare-study-final-report.pdf (accessed December 22, 2018).
[48] E.C. Fortner, W.A. Brooks, T.B. Onasch, M.R. Canagaratna, P. Massoli, J.T. Jayne, J.P. Franklin, W.B. Knighton, J. Wormhoudt, D.R. Worsnop, C.E. Kolb, S.C. Herndon, Particulate Emissions Measured During the TCEQ Comprehensive Flare Emission Study, Industrial & Engineering Chemistry Research. 51 (2012) 12586–12592. doi:10.1021/ie202692y.
[49] International Organization for Standardization, Measurement of fluid flow by means of pressure differential devices inserted in circular cross-section conduits running full — Part 5: Cone meters (ISO 5167-5), Geneva, Switzerland, 2016. https://www.iso.org/standard/62568.html.
[50] Droplet Measurement Technologies, Inc., Photoacoustic Extinctiometer (PAX) Operator Manual, Boulder, Colorado, 2012. http://www.dropletmeasurement.com/sites/default/files/ManualsGuides/Hardware%20Manuals/PAX%20Manual.pdf.
[51] D.J. Corbin, M.R. Johnson, Detailed Expressions and Methodologies for Measuring Flare Combustion Efficiency, Species Emission Rates, and Associated Uncertainties, Industrial & Engineering Chemistry Research. 53 (2014) 19359–19369. doi:10.1021/ie502914k.

[52] W. Wagner, H.-J. Kretzschmar, International Steam Tables, Springer Berlin Heidelberg, Berlin, Heidelberg, 2008. doi:10.1007/978-3-540-74234-0.
[53] David Dandy, Chemical Equilibrium Calculator, (2019). http://navier.engr.colostate.edu/code/code-4/index.html (accessed March 3, 2019).
[54] Susan Solomon, Dahe Qin, Martin Manning, Melinda Marquis, Kristen Averyt, Melinda M.B. Tignor, Henry LeRoy Miller, Zhenlin Chen, Climate change 2007: the physical science basis: contribution of Working Group I to the Fourth Assessment Report of the Intergovernmental Panel on Climate Change, Cambridge University Press, Cambridge ; New York, 2007.
[55] C.C. Ndubizu, R. Ananth, P.A. Tatem, V. Motevalli, On water mist fire suppression mechanisms in a gaseous diffusion flame, Fire Safety Journal. 31 (1998) 253–276. doi:10.1016/S0379-7112(98)00007-1.
[56] J. Richard, J.. Garo, J.. Souil, J.. Vantelon, V.. Knorre, Chemical and physical effects of water vapor addition on diffusion flames, Fire Safety Journal. 38 (2003) 569–587. doi:10.1016/S0379-7112(03)00012-2.
[57] W.J.A. Dahm, C.E. Frieler, G. Tryggvason, Vortex structure and dynamics in the near field of a coaxial jet, Journal of Fluid Mechanics. 241 (1992) 371. doi:10.1017/S0022112092002088.
[58] H. Rehab, E. Villermaux, E.J. Hopfinger, Flow regimes of large-velocity-ratio coaxial jets, Journal of Fluid Mechanics. 345 (1997) 357–381. doi:10.1017/S002211209700637X.
[59] D. Castiñeira, T.F. Edgar, CFD for Simulation of Steam-Assisted and Air-Assisted Flare Combustion Systems, Energy & Fuels. 20 (2006) 1044–1056. doi:10.1021/ef050332v.
[60] K. Müller-Dethlefs, A.F. Schlader, The effect of steam on flame temperature, burning velocity and carbon formation in hydrocarbon flames, Combustion and Flame. 27 (1976) 205–215. doi:10.1016/0010-2180(76)90023-7.
[61] D. Joseph, J. Lee, C. McKinnon, R. Payne, J. Pohl, Evaluation of the Efficiency of Industrial Flares: Background-Experimental Design-Facility, U.S. Environmental Protection Agency, Washington, D.C., 1983.

Appendix A Uncertainty Analysis Methodology

When defining the various quantitative parameters used to describe the operation of the experiments and the results they yielded, an uncertainty value is needed to provide an estimation of the proximity between the quantity and the true value. Therefore, an uncertainty analysis was performed for parameters such as the steam and fuel mass flow rates, the measurement of black carbon and gas phase emission species, and the calculation of carbon conversion efficiency and emission indices. The two types of errors considered when evaluating the uncertainty of any given parameter were the bias and precision errors.

The bias error (B_x) is defined as the offset from the true value irrelative of the number of measurements taken. This type of error arises due to the systematic error that is characteristic of a particular instrument which can be minimized through a calibration of the instrument, or human error during the measurement process. The bias error of an instrument is usually taken from the manufacturer specifications or a calibration curve.

Precision error (P_x) is defined as the statistical variation of the measurements outside the mean value. Based on the sample size of the measurements taken, the precision uncertainty can be defined differently. For a sample size of $n > 30$, the precision uncertainty is based on the standard normal distribution and is defined as follows:

$$P_x = z\frac{\sigma}{\sqrt{n}} \tag{A.1}$$

where z is the z-score ranging from -1.96 to 1.96 for a corresponding confidence interval of 95%, σ is the standard deviation, and n is the sample size represented by the number of measurements taken. The standard deviation is defined as:

$$\sigma = \sqrt{\frac{(x_i - \bar{x})^2}{n}} \tag{A.2}$$

where x_i is the measured value and $\bar{x}$ is the mean value of the sample.

The bias and precision errors were combined to generate a total uncertainty (U_x) of the measurement at a 95% confidence interval as shown:

$$U_x = \Delta x = \sqrt{{B_x}^2 + {P_x}^2} \tag{A.3}$$

By defining *y* as a function dependent on *n* independent variables all having the same confidence interval (*i.e.*, $y = f(x_1, x_2, \dots, x_n)$), the uncertainty in *y* can then be determined by applying the following error propagation rule:

$$\Delta y = \sqrt{\left(\frac{\partial f}{\partial x_1}\Delta x_1\right)^2 + \left(\frac{\partial f}{\partial x_2}\Delta x_2\right)^2 + \cdots + \left(\frac{\partial f}{\partial x_n}\Delta x_n\right)^2}. \tag{A.4}$$

Appendix B Gas Mass Flow Controller Calibration

The mass flow controllers described in Chapter 2 were each calibrated for their respective gases using a drum-type gas meter (Ritter, TG-50) as shown in Figure B.1. Just as in the experimental setup, the gases were piped through a heated water bath set to 35 °C in order to regulate the gas temperatures to approximately room temperature (*i.e.*, 23 °C). The heated gas was then metered out with a mass flow controller to the inlet port of the gas meter. The gas meter operates on the basis of positive volume displacement. It consists of a cylindrical drum that rotates on an axle and is partitioned into four chambers. Each of the chambers are sealed with water that fills up the housing above the central axis. The chambers also each contain an inlet and outlet. As the gas is fed into the gas meter, it fills up two of the chambers causing the drum assembly to rotate due to a pressure difference between the inlet and outlet ports. As the drum continues to rotate, the gas is evacuated from the chamber as it fills with water. The gas exits the meter and is exhausted to the capture hood.

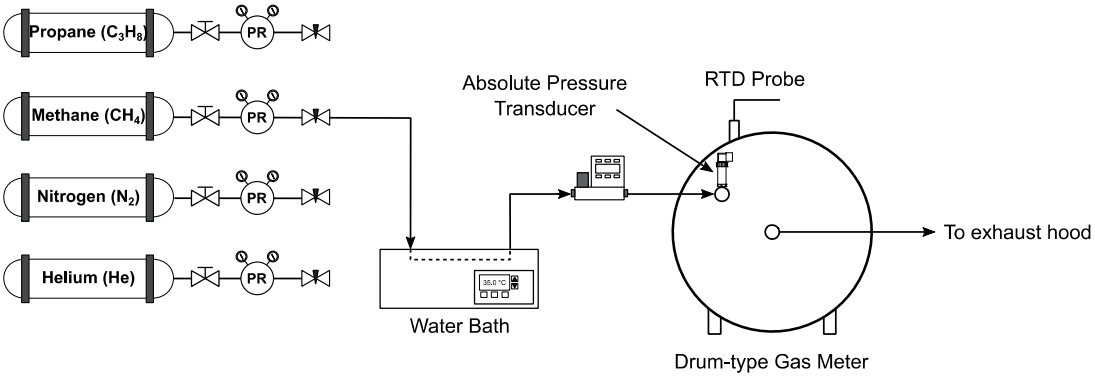

Figure B.1: Mass flow controller calibration setup.

The meter contains a pulse generator that keeps track of the number of revolutions the drum performs. The meter outputs a volumetric flow rate of the gas by multiplying the volume of the chambers by four and then dividing by the time elapsed for a single revolution of the drum. This volumetric flow rate is captured through serial communication on a LabVIEW program. The absolute pressure transducer (Omega Engineering, PX409-USBH Series) and RTD probe (Omega

Engineering, P-L Series) were used to provide the pressure and temperature of the gas within the meter. This was to allow for the volumetric flow rate, $\dot{V}_s$, to be corrected to SLPM conditions based on the ideal gas law as follows:

$$\dot{V}_s = \dot{V}_g \frac{p_g T_s}{p_s T_g} \tag{B.1}$$

where $\dot{V}_g$ (LPM) is the volumetric flow rate at the gas meter pressure, p_g (kPa), and temperature, T_g (K). The standard temperature and pressure, T_s and p_s, are 101.3 kPa and 298 K, respectively.

For each of the mass flow controllers, a 10-point calibration curve was generated, as shown in Figure B.2. Based on linear regression statistics, a 95% confidence interval was calculated for each of the calibration curves. For the methane calibration curve shown in Figure B.2, this yielded a maximum bias uncertainty of ± 0.1 SLPM. This was within the error provided by the manufacturer, which was ± (0.8% of reading + 0.1 SLPM).

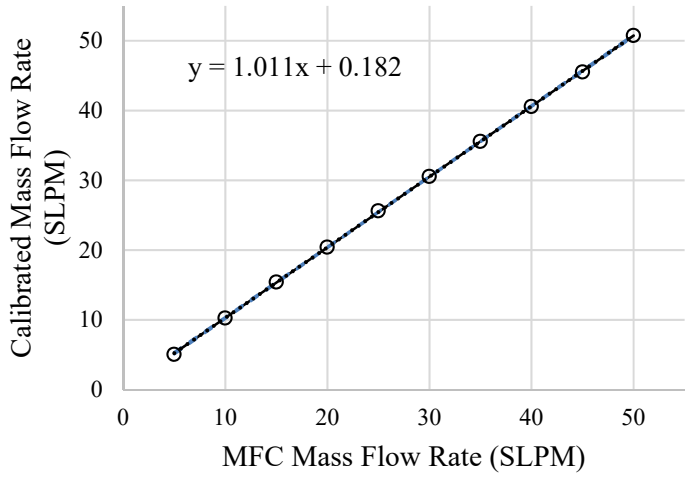

Figure B.2: Calibration curve for 50 SLPM mass flow controller running methane.

Appendix C Steam Production and Distribution System Calibration

The steam production and delivery system was calibrated based on the setup shown in Figure C.1. The same basic setup was used as described in Chapter 2, except that the cone flowmeter was piped using 12.7 mm diameter copper tubing directly to one of the inlets of a plate heat exchanger (McMaster-Carr, 35115K62). By supplying cold water to the secondary inlet of the heat exchanger, the steam was condensed into its liquid phase. The cooling water discharge was piped to a drain, while the steam condensate leaving the heat exchanger was carried through plastic tubing to a beaker resting on a mass balance (A&D, HF-6000G) having a full scale of 6 000 g (uncertainty ± 0.1 g).

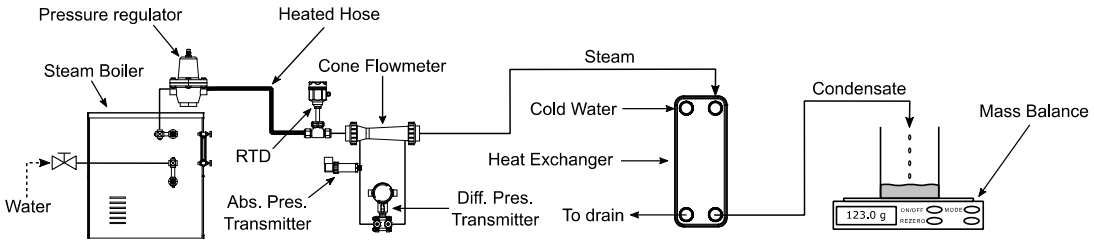

Figure C.1: Steam production and delivery system calibration setup.

For the purposes of the present study, the cone flow meter was calibrated at seven different flow rates ranging between 14 – 100 g/min. At each of the calibration points, the calculated, or theoretical, steam mass flow rate based on Equation (2.1) was recorded as shown in Figure C.2. The overall mass flow rate at this point was determined by taking the average of all the calculated mass flow rates. Simultaneously, the cumulative steam mass flow rate measured by the mass balance was recorded as shown in Figure C.3. For each calibration point, steam condensate was collected in the beaker over a period of up to 30 minutes or until the transients in the average mass flow rate were resolved to less than 0.1%. As shown in Figure C.3, different timeframes were used to resolve the transients due to the significant fluctuations of the steam mass flow rate in the initial calibration period.

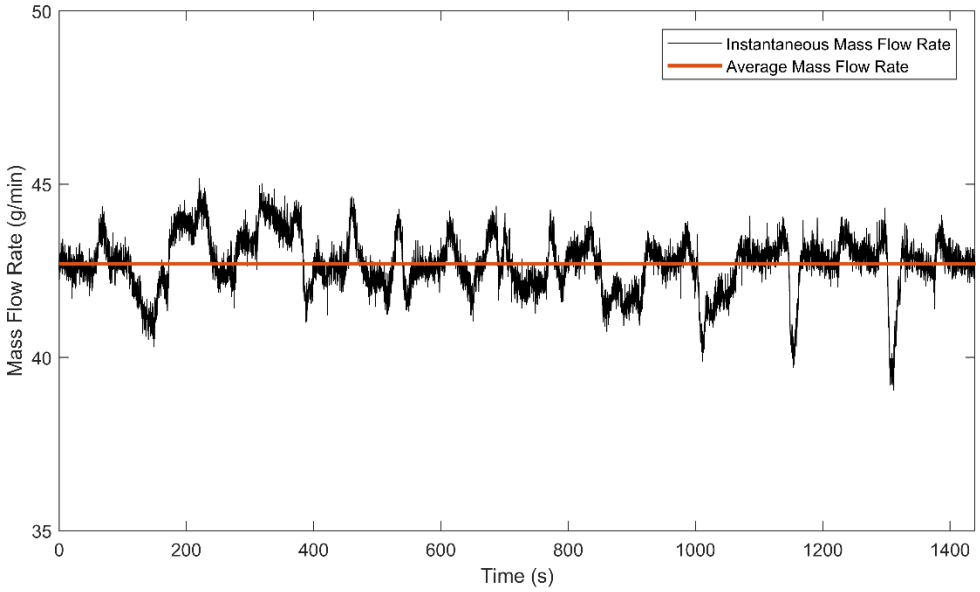

Figure C.2: Theoretical mass flow rate of steam.

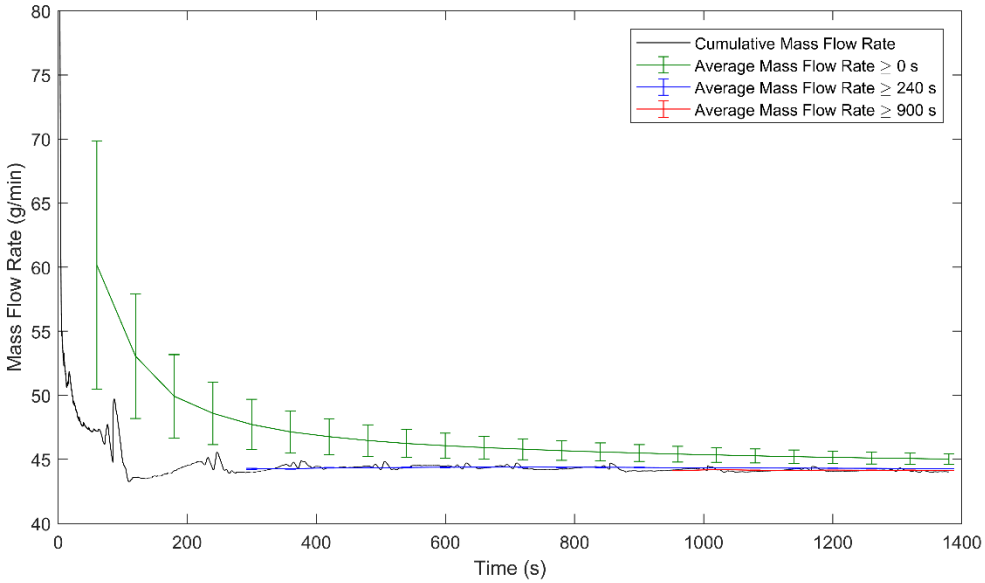

Figure C.3: Experimental mass flow rate of steam.

Once the theoretical and experimental steam mass flow rates for each of the calibration points were satisfactorily resolved, they were plotted on a calibration curve as shown in Figure C.4. Using linear regression statistics, the 95% confidence interval for the calibration curve was calculated and plotted. As can be seen in Figure C.4, the confidence intervals are slightly hyperbolic, with the greatest uncertainty occurring at

the low and high end of the calibration curve. Overall, the maximum bias uncertainty for the calibration curve was determined to be ± 3.9 g/min.

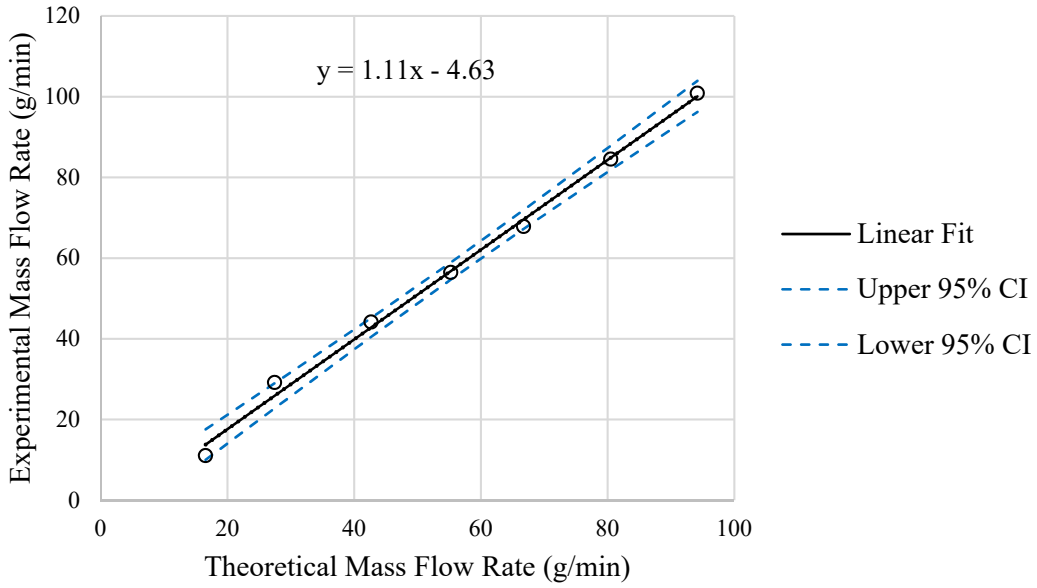

Figure C.4: Steam mass flow rate calibration curve.

Appendix D Gas Chromatograph Calibration Standards and Uncertainties

The gas chromatograph (GC) was calibrated with the standards shown in Table D.1.

Table D.1: GC calibration standards.

Standard	Gas species (mol %)									
	H_2	CO	CO_2	CH_4	C_2H_6	C_3H_8	C_4H_{10}	N_2	He	O_2
1		0.0998	5.01					93.88		1.01
2	0.4018	19.95		0.1002	0.09975	0.09937		79.449		
3		0.01						99.889		0.1005
5	4.005			0.9947	1.013	1.008		92.979		
9		3.005	19.95					57.055		19.99
11	0.04	9.983		0.0105	0.0101	0.0102		89.946		
12			0.8108	94.96	2.4	0.0589	0.0103	1.76		
14			0.09969					99.79971	0.1006	
15			0.0402	0.001	0.001	0.001	0.001	99.905802	0.05	

For the purposes of calculating the CCE and EIs for THC, CO_2, and CO, the only relevant calibration curves were for CH_4, C_2H_6, C_3H_8, CO_2, and CO. An example of the CH_4 calibration curve is shown in Figure D.1.

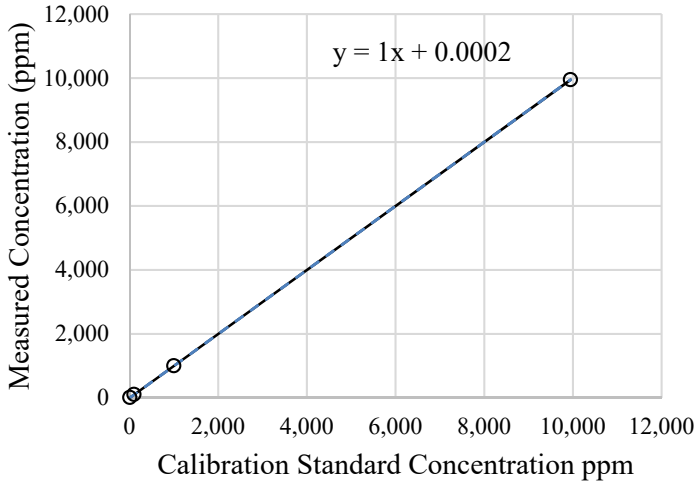

Figure D.1: Calibration curve for CH_4.

Based on linear regression statistics a linear equation was generated for each calibration curve. A 95% confidence interval was also calculated which allowed for the bias error to be defined as shown in Table D.2. In order to determine the precision uncertainty associated with taking repeated measurements with the GC, a series of tests were performed over a span of three days. On each consecutive day, a 100 L Tedlar bag was filled with a diluted combustion sample representative of the species captured during the actual experiments and sampled five times with the GC. The precision uncertainty for each of the species on each of the three days was then calculated based on the five samples using the student t-distribution due to a sample size $n < 30$. The largest of the three precision uncertainties calculated for each species was then selected as the representative precision uncertainty. Refer to Table D.2 for the precision uncertainties as well as the total uncertainties for each of the five species.

Table D.2: Uncertainties for gases measured by GC.

Species	Uncertainty (ppm)		
	Bias (B_x)	Precision (P_x)	Total (U_x)
CH_4	0.020	38.2	38.2
C_2H_6	0.001	22.8	22.8
C_3H_8	0.015	2.1	2.1
CO_2	0.009	67.9	67.9
CO	0.014	11.8	11.8

Appendix E Uncertainty Analysis for CCE and EI

As described in Chapter 2 of this thesis, CCE was calculated using Equation (2.6). The uncertainty for this equation can be expressed by performing the propagation of uncertainty as follows:

$$(\Delta\eta)^2 = \left(\frac{\partial\eta}{\partial\dot{n}_{\mathrm{CO_2,produced}}}\Delta\dot{n}_{\mathrm{CO_2,produced}}\right)^2 + \left(\frac{\partial\eta}{\partial\dot{n}_{\mathrm{FG}}}\Delta\dot{n}_{\mathrm{FG}}\right)^2. \tag{E.1}$$

The error in the molar flow rate of produced CO_2, $\dot{n}_{\mathrm{CO_2,produced}}$, can be determined in a similar manner based on Equation (2.7):

$$\begin{aligned}\left(\Delta\dot{n}_{\mathrm{CO_2,produced}}\right)^2 = &\left(\frac{\partial\dot{n}_{\mathrm{CO_2,produced}}}{\partial X_{\mathrm{CO_2,plume}}}\Delta X_{\mathrm{CO_2,plume}}\right)^2 + \left(\frac{\partial\dot{n}_{\mathrm{CO_2,produced}}}{\partial\dot{n}_{\mathrm{plume}}}\Delta\dot{n}_{\mathrm{plume}}\right)^2 + \\ &\left(\frac{\partial\dot{n}_{\mathrm{CO_2,produced}}}{\partial X_{\mathrm{CO_2},\infty}}\Delta X_{\mathrm{CO_2},\infty}\right)^2 + \left(\frac{\partial\dot{n}_{\mathrm{CO_2,produced}}}{\partial\dot{n}_{\infty}}\Delta\dot{n}_{\infty}\right)^2 + \left(\frac{\partial\dot{n}_{\mathrm{CO_2,produced}}}{\partial X_{\mathrm{CO_2,FG}}}\Delta X_{\mathrm{CO_2,FG}}\right)^2 + \\ &\left(\frac{\partial\dot{n}_{\mathrm{CO_2,produced}}}{\partial\dot{n}_{\mathrm{FG}}}\Delta\dot{n}_{\mathrm{FG}}\right)^2.\end{aligned} \tag{E.2}$$

Since the fuel gases used in the present study were high purity CH_4 and C_3H_8, the volume fraction of CO_2 in the fuel was assumed to be zero. Therefore, the error in $\dot{n}_{\mathrm{CO_2,produced}}$ can be simplified as follows:

$$\begin{aligned}\left(\Delta\dot{n}_{\mathrm{CO_2,produced}}\right)^2 = &\left(\frac{\partial\dot{n}_{\mathrm{CO_2,produced}}}{\partial X_{\mathrm{CO_2,plume}}}\Delta X_{\mathrm{CO_2,plume}}\right)^2 + \left(\frac{\partial\dot{n}_{\mathrm{CO_2,produced}}}{\partial\dot{n}_{\mathrm{plume}}}\Delta\dot{n}_{\mathrm{plume}}\right)^2 + \\ &\left(\frac{\partial\dot{n}_{\mathrm{CO_2,produced}}}{\partial X_{\mathrm{CO_2},\infty}}\Delta X_{\mathrm{CO_2},\infty}\right)^2 + \left(\frac{\partial\dot{n}_{\mathrm{CO_2,produced}}}{\partial\dot{n}_{\infty}}\Delta\dot{n}_{\infty}\right)^2.\end{aligned} \tag{E.3}$$

Equation (E.3) now has two unknown error values which are $\Delta\dot{n}_{\mathrm{plume}}$ and $\Delta\dot{n}_{\infty}$. The error in $\Delta\dot{n}_{\mathrm{plume}}$ can be determined by applying the propagation of uncertainty to Equation (2.9) as follows:

$$\left(\Delta\dot{n}_{\text{plume}}\right)^2 = \sum_k \left(\frac{\partial \dot{n}_{\text{plume}}}{\partial X_{k,\infty}} \Delta X_{k,\infty}\right)^2 + \sum_k \left(\frac{\partial \dot{n}_{\text{plume}}}{\partial X_{k,\text{plume}}} \Delta X_{k,\text{plume}}\right)^2 + \left(\frac{\partial \dot{n}_{\text{plume}}}{\partial \dot{n}_{\text{FG}}} \Delta\dot{n}_{\text{FG}}\right)^2 + \left(\frac{\partial \dot{n}_{\text{plume}}}{\partial X_{\text{CO}_2,\text{FG}}} \Delta X_{\text{CO}_2,\text{FG}}\right)^2. \quad \text{(E.4)}$$

As with Equation (E.2), the above equation can be simplified due to the assumption of CO_2 not being present in the fuel gases:

$$\left(\Delta\dot{n}_{\text{plume}}\right)^2 = \sum_k \left(\frac{\partial \dot{n}_{\text{plume}}}{\partial X_{k,\infty}} \Delta X_{k,\infty}\right)^2 + \sum_k \left(\frac{\partial \dot{n}_{\text{plume}}}{\partial X_{k,\text{plume}}} \Delta X_{k,\text{plume}}\right)^2 + \left(\frac{\partial \dot{n}_{\text{plume}}}{\partial \dot{n}_{\text{FG}}} \Delta\dot{n}_{\text{FG}}\right)^2. \quad \text{(E.5)}$$

The error in the molar flow rate of fuel gas, $\dot{n}_{\text{FG}}$, has now been reintroduced. Its error is based on the mass flow rate error and can be defined as follows:

$$\Delta\dot{n}_{\text{FG}} = \frac{\partial \dot{n}_{\text{FG}}}{\partial \dot{m}_{\text{FG}}} \Delta\dot{m}_{\text{FG}} = \frac{\Delta\dot{m}_{\text{FG}}}{M_{\text{FG}}}. \quad \text{(E.6)}$$

The molar flow rate of ambient air, $\Delta\dot{n}_{\infty}$, is defined based on the flare control volume shown in Figure 2.3 as follows:

$$\Delta\dot{n}_{\infty} = \frac{M_{\text{plume}}}{M_{\infty}} \dot{n}_{\text{plume}} - \frac{M_{\text{FG}}}{M_{\infty}} \dot{n}_{\text{FG}}. \quad \text{(E.7)}$$

The error in $\Delta\dot{n}_{\infty}$ is then defined as:

$$(\Delta\dot{n}_{\infty})^2 = \left(\frac{\partial \dot{n}_{\infty}}{\partial \dot{n}_{\text{plume}}} \Delta\dot{n}_{\text{plume}}\right)^2 + \left(\frac{\partial \dot{n}_{\infty}}{\partial \dot{n}_{\text{FG}}} \Delta\dot{n}_{\text{FG}}\right)^2. \quad \text{(E.8)}$$

The error in CCE can now be defined as follows:

$$(\Delta\eta)^2 = \left(\frac{\partial\eta}{\partial\dot{n}_{\mathrm{CO_2,produced}}}\right)^2 \left\{\left(\frac{\partial\dot{n}_{\mathrm{CO_2,produced}}}{\partial X_{\mathrm{CO_2,plume}}}\Delta X_{\mathrm{CO_2,plume}}\right)^2 + \left(\frac{\partial\dot{n}_{\mathrm{CO_2,produced}}}{\partial\dot{n}_{\mathrm{plume}}}\right)^2 \left[\sum_k \left(\frac{\partial\dot{n}_{\mathrm{plume}}}{\partial X_{k,\infty}}\Delta X_{k,\infty}\right)^2 + \sum_k \left(\frac{\partial\dot{n}_{\mathrm{plume}}}{\partial X_{k,\mathrm{plume}}}\Delta X_{k,\mathrm{plume}}\right)^2 + \left(\frac{\partial\dot{n}_{\mathrm{plume}}}{\partial\dot{n}_{\mathrm{FG}}}\frac{\Delta\dot{m}_{\mathrm{FG}}}{M_{\mathrm{FG}}}\right)^2\right] + \left(\frac{\partial\dot{n}_{\mathrm{CO_2,produced}}}{\partial X_{\mathrm{CO_2},\infty}}\Delta X_{\mathrm{CO_2},\infty}\right)^2 + \left(\frac{\partial\dot{n}_{\mathrm{CO_2,produced}}}{\partial\dot{n}_{\infty}}\right)^2 \left[\left(\frac{\partial\dot{n}_{\infty}}{\partial\dot{n}_{\mathrm{plume}}}\right)^2 \left(\sum_k \left(\frac{\partial\dot{n}_{\mathrm{plume}}}{\partial X_{k,\infty}}\Delta X_{k,\infty}\right)^2 + \sum_k \left(\frac{\partial\dot{n}_{\mathrm{plume}}}{\partial X_{k,\mathrm{plume}}}\Delta X_{k,\mathrm{plume}}\right)^2 + \left(\frac{\partial\dot{n}_{\mathrm{plume}}}{\partial\dot{n}_{\mathrm{FG}}}\frac{\Delta\dot{m}_{\mathrm{FG}}}{M_{\mathrm{FG}}}\right)^2\right) + \left(\frac{\partial\dot{n}_{\infty}}{\partial\dot{n}_{\mathrm{FG}}}\frac{\Delta\dot{m}_{\mathrm{FG}}}{M_{\mathrm{FG}}}\right)^2\right]\right\} + \left(\frac{\partial\eta}{\partial\dot{n}_{\mathrm{FG}}}\frac{\Delta\dot{m}_{\mathrm{FG}}}{M_{\mathrm{FG}}}\right)^2. \quad \text{(E.9)}$$

The remaining errors in the ambient and plume gas species mole fractions $X_{k,\infty}$ and $X_{k,\mathrm{plume}}$ were based on the GC uncertainties outlined in Table D.2 of Appendix D. The error in the fuel gas mass flow rate $\dot{m}_{\mathrm{FG}}$ was based on the mass flow controller uncertainty.

The error in the emission indices Equation (2.11) for gas species was expressed as follows:

$$\left(\Delta EI_j\right)^2 = \left(\frac{\partial EI_j}{\partial X_{j,\mathrm{plume}}}\Delta X_{j,\mathrm{plume}}\right)^2 + \left(\frac{\partial EI_j}{\partial X_{j,\infty}}\Delta X_{j,\infty}\right)^2 + \left(\frac{\partial EI_j}{\partial\dot{m}_{\mathrm{FG}}}\Delta\dot{m}_{\mathrm{FG}}\right)^2 + \left(\frac{\partial EI_j}{\partial\dot{n}_{\mathrm{plume}}}\right)^2 \left[\sum_k \left(\frac{\partial\dot{n}_{\mathrm{plume}}}{\partial X_{k,\infty}}\Delta X_{k,\infty}\right)^2 + \sum_k \left(\frac{\partial\dot{n}_{\mathrm{plume}}}{\partial X_{k,\mathrm{plume}}}\Delta X_{k,\mathrm{plume}}\right)^2 + \left(\frac{\partial\dot{n}_{\mathrm{plume}}}{\partial\dot{n}_{\mathrm{FG}}}\frac{\Delta\dot{m}_{\mathrm{FG}}}{M_{\mathrm{FG}}}\right)^2\right]. \quad \text{(E.10)}$$

The error in BC emission indices can be defined as follows:

$$(\Delta EI_{BC})^2 = \left(\frac{\partial EI_{BC}}{\partial f_{m,\text{measured}}}\Delta f_{m,\text{measured}}\right)^2 + \left(\frac{\partial EI_{BC}}{\partial T_{\text{cell}}}\Delta T_{\text{cell}}\right)^2 + \left(\frac{\partial EI_{BC}}{\partial P_{\text{plume}}}\Delta P_{\text{plume}}\right)^2 + \left(\frac{\partial EI_{BC}}{\partial \dot{n}_{\text{plume}}}\right)^2 \left[\sum_k \left(\frac{\partial \dot{n}_{\text{plume}}}{\partial X_{k,\infty}}\Delta X_{k,\infty}\right)^2 + \sum_k \left(\frac{\partial \dot{n}_{\text{plume}}}{\partial X_{k,\text{plume}}}\Delta X_{k,\text{plume}}\right)^2 + \left(\frac{\partial \dot{n}_{\text{plume}}}{\partial \dot{n}_{\text{FG}}}\frac{\Delta \dot{m}_{\text{FG}}}{M_{\text{FG}}}\right)^2\right]. \quad \text{(E.11)}$$

The error in the measured black carbon mass concentration is based on Equation (2.3) as follows:

$$\Delta f_{m,\text{measured}} = \frac{\partial f_{m,\text{measured}}}{\partial B_{\text{abs}}}\Delta B_{\text{abs}} = \frac{\Delta B_{\text{abs}}}{\text{MAC}}. \quad \text{(E.12)}$$

Furthermore, the repeatability of the experimental sets can be assessed by comparing the results in the emission indices in BC, NO_x, and CO_2 for the common experimental test points. The three experiments performed using the same operating parameters were the unassisted flames for experimental sets 1, 4, and 5. The EI_{BC}, EI_{NO_x}, and EI_{CO_2} values for these experiments are shown in Table E.1. The standard deviations calculated show that all of the emission indices are within a standard deviation of the mean except for EI_{BC} of experimental set 4.

Table E.1: Repeatability in BC, NO_x, and CO_2 emission indices for unassisted flame tests for experimental sets 1, 4, and 5.

Emission Index	Experimental Sets at MFR = 0			Mean	Standard Deviation
	1	4	5		
EI_{BC}	0.076	0.115	0.092	0.094	0.019
EI_{NO_x}	1.21	1.15	1.10	1.15	0.06
EI_{CO_2}	2742.9	2742.8	2742.9	2742.8	0.1

Appendix F Adiabatic Flame Temperature

The adiabatic flame temperature was determined for each of the experimental sets in order to investigate the effect of steam assist on the product gas temperature. The adiabatic flame temperature is the maximum temperature that the product gases can reach in a steady-flow combustion process in which no heat is lost to the surroundings and no work is extracted from the flow. The equation that defines this isoenthalpic process is as follows:

$$\sum n_r\left(\bar{h}_f^\circ + \bar{h}(T) - \bar{h}^\circ\right)_r = \sum n_p\left(\bar{h}_f^\circ + \bar{h}(T_{ad}) - \bar{h}^\circ\right)_p, \tag{F.1}$$

where n is the number of moles of the species, $\bar{h}_f^\circ$ is the enthalpy of formation of the species at 25 °C and 1 atm, and $\bar{h}(T) - \bar{h}^\circ$ represents the sensible enthalpy of the species relative to 25 °C and 1 atm. A schematic of the steady-flow combustion process is shown in Figure F.1.

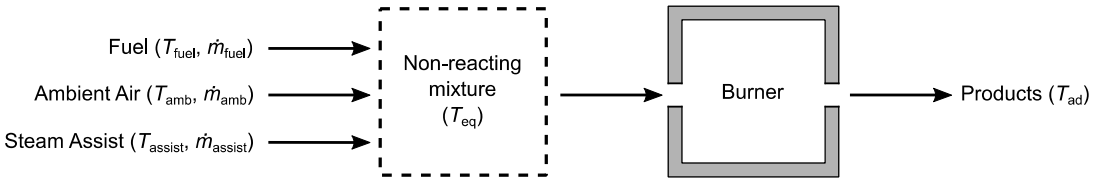

Figure F.1: Steady-flow combustion process for determining the adiabatic flame temperature.

The process of calculating the adiabatic flame temperature for each of the experimental sets was divided into two stages. Firstly, an equilibrium temperature, T_{eq} (K), for the non-reacting mixture of the reactants including the fuel, assist fluid, and the stoichiometric ambient air was calculated based on the following energy balance:

$$\sum_k \dot{m}_k \langle c_{p,k} \rangle T_k = \sum_k \dot{m}_k \langle c_{p,k} \rangle T_{eq}, \tag{F.2}$$

where $\dot{m}_k$ represents the mass flow rate of each component, k, of the pre-combustion non-reacting mixture including the fuel gas, assist fluids, and combustion air proportional to the CCE, $\langle c_{p,k} \rangle$ (J/kg·K) is the representative isobaric specific heat capacity of component k, and T_k (K) is the initial temperature of component k. The equilibrium temperature was then isolated as

$$T_{eq} = \frac{\sum_k \dot{m}_k \langle c_{p,k} \rangle T_k}{\sum_k \dot{m}_k \langle c_{p,k} \rangle}. \tag{F.3}$$

Using STANJAN, a chemical equilibrium solver, the molar flow rate of each species in the reactant stream, an initial temperature of T_{eq}, and the ambient pressure were implemented as starting parameters. The list of species at equilibrium for experimental set 1 were: CH_4, O_2, N_2, H_2O, CO_2, CO, NO_2, NO, H_2, OH, H, N, and O. Experimental sets 4 and 5 also included He while experimental set 6 listed C_2H_6 and C_3H_8 as well. The adiabatic flame temperature was then calculated under constant temperature and pressure as shown in Figure 3.2.